AFIT/GAE/ENY/91D-19

Fatigue Behavior and Failure Mechanisms of Centrally Notched $[0]_8$ and $[(0/90)_2]_{(S)}$ Silicon Carbide Reinforced Aluminosilicate Glass

THESIS

William R. Moschelle
Captain, USAF
AFIT/GAE/ENY/91D-19

AFIT/GAE/ENY/91D-19

Fatigue Behavior and Failure Mechanisms of Centrally Notched $[0]_8$ and $[(0/90)_2]_S$ Silicon Carbide Reinforced Aluminosilicate Glass

THESIS

Presented to the Faculty of the School of Engineering
of the Air Force Institute of Technology
Air University
In Partial Fulfillment of the
Requirements for the Degree of
Master of Science in Aeronautical Engineering

William R. Moschelle
Captain, USAF

December 1991

Approved for public release; distribution unlimited

Acknowledgments

Several individuals provided expert assistance and guidance towards the completion of this project. I would like to recognize their efforts here.

First, I extend my gratitude to Dr. Shankar Mall, my advisor. Dr. Mall was always available to all of his students whenever they needed help and his patience and technical expertise were greatly appreciated.

The AFIT Aeronautical Engineering Laboratory staff was also instrumental in this project. Every technician had a hand in helping me either prepare the test station or assisting in the use of the examination equipment; such as the scanning electron microscope. Without the help of Jay Anderson, Mark Derriso, Andy Pitts and Dan Rioux, this thesis would not have been completed.

Several individuals outside of AFIT also played important roles. Captain John Pernot of the Air Force Materials Laboratory was the project sponsor. He provided all specimens for testing and was always available whenever I had questions. I would also like to thank Tim Hancock of the AFIT model shop. He machined all parts that were new modifications to the test station. Finally, I'd like to thank Bob Lewis of the Material Laboratory's metallography lab. He provided a great deal of assistance in the preparing of specimens for microscopic examination.

Table of Contents

List of Figures

List of Tables

ABSTRACT

The purpose of this study was to determine the fatigue behavior of notched Silicon Carbide fiber-reinforced Aluminosilicate glass, SiC/1723. Two lay-ups were investigated, $[0]_8$ and $[(0/90)_2]_s$. All specimens were centrally notched with a 1.6 millimeter hole.

Fatigue testing was accomplished using the 22.24 kN MTS tension machine in the AFIT Aeronautical Engineering laboratory. The test set-up underwent minor modifications and realignment from last usage to ensure the specimens would be subjected to the absolute minimum of stress due to bending and torsion which occur when the specimen grips are not properly aligned.

Stress versus strain curves and modulus reduction during cycling were obtained for each lay-up. It was found that at a certain stress threshold level for $[0]_8$ and $[(0/90)_2]_s$, failure would not occur over one million cycles, while stresses above that level would produce failure.

Damage was monitored in all specimens by measurement of stiffness modulus degradation. In addition, acetate replications were used to record matrix microcrack growth and ultrasonic C-scan inspection was used to monitor internal damage.

Several analytical models used for other types of composites were applied to these laminates to see if the fatigue behavior of SiC/1723 could be predicted and characterized by these existing models. It was found that extending classical laminated plate theory to fatigue, along with total ply discount method, the fatigue failure of the bidirectional laminates could be approximated quite closely. Three other models, Whitney-Nuismer, Fatigue Modulus Concept and Elastic Degradation Model, were applied to the unidirectional lay-up. The Whitney-Nuismer model provided the closest correlation to actual data. The other two models were inadequate in predicting fatigue life for this composite.

The notch appeared to lower the ultimate stress and fatigue failure stresses of the unidirectional laminate. Cracks initiated at points on the hole near the theoretical maximum stress concentration point for these specimens. Longitudinal, ie. loading direction, cracks grew from these points leading to fiber breakage and specimen failure.

The $[(0/90)_2]_s$ specimens were insensitive to the notch. Notched and unnotched ultimate strengths were nearly identical. The notched fatigue endurance limit was within eight percent of the unnotched value. Fatigue damage modes included transverse matrix cracking in the 90^0 plies. These

cracks were then deflected longitudinally when they approached the $0^0/90^0$ interface. This led to delamination cracks and delamination between the plies. Final failure occurred with fiber breakage and pullout in the 0^0 laminae. Failure in the 90^0 plies was always marked by an increase in transverse crack density at the eventual fracture site.

FATIGUE BEHAVIOR AND FAILURE MECHANISMS OF CENTRALLY NOTCHED $[0]_8$ AND $[(0/90)_2]_S$ SILICON CARBIDE REINFORCED ALUMINOSILICATE GLASS

I. Introduction

A. Background

Ceramic materials have long held a place in engineering applications as a class of materials with high levels of hardness and, on average, higher melting points than either metals or polymers [1]. These properties have made them candidates for high temperature aerospace applications. In addition, ceramics offer advantages such as high resistance to degradation due to oxidation and the ability to be an electrical insulator.

Monolithic ceramics are typically very hard due to their inability to undergo plastic deformation. This lack of deformation is caused by the ordering of atoms in ceramics which provide for fewer slip systems than in metals. Furthermore, ceramics have a high notch sensitivity. This means a discontinuity or existing crack in a ceramic can see a severe stress concentration rise at a crack tip [2]. Therefore, ceramics can fail suddenly and catastrophically due to pre-existing flaws or cracks. This brittleness has hampered the extensive use of ceramics since life prediction is difficult unless the ceramic is perfectly formed.

In spite of this, several adverse environment applications of ceramics have been investigated. Engineers at the Ford Motor Company and NASA among others have built and tested gas turbine engines made of ceramics. Some of the components that were made entirely of ceramics were the combustion chamber and turbine blades, both rotating and stationary. These engines were able to withstand very high temperature for extended amounts of time; benefitting from the high temperature characteristics of ceramics. Failures encountered involved sudden failures due to crack propagation of internal flaws.

The resistance of brittle materials such as ceramics to tensile loads can be increased dramatically with the addition of a high strength fiber reinforcer. Common fibers used to reinforce glasses and glass-ceramics are carbon and silicon carbide (SiC). Fibers serve to increase strength and stiffness, provide high temperature stability and allow the ceramic to increase fracture toughness [3].

The low density of fiber reinforced ceramic matrix composites (CMC) provides an opportunity for their application in aerospace applications. Europeen de Propulsion, a leader in composite manufacturing in Europe, has already developed a CMC, carbon fiber/SiC matrix, that will be used as the material for the Arianne launch vehicle exhaust nozzle. They have also demonstrated a SiC/SiC composite as a ramjet combustion chamber material with great

success. If the fracture toughness can be further improved, CMC's would be ideal candidates to be implemented in the next generation of turbojet engines. The Air Force Propulsion Laboratory's goal to double the thrust to weight ratio of current gas turbine engines could use CMC's high temperature capability and strength to weight ratio to advantage to meet their goal. Research is continuing to provide a more crack resistant CMC, and to characterize and predict the behavior of CMCs. This thesis is part of that research. Two important areas of concern are the fatigue characteristics of CMCs and their response to geometric discontinuities such as holes.

Fatigue testing provides a realistic measure of a material's ability to withstand actual service environments. For example, wing components on an aircraft are subjected to repeated, fluctuating loads which can cause failure well below a component's ultimate strength. Since composites have played an increasing role in aircraft body construction (e.g. see Reference 4), it is necessary to understand the mechanisms involved in composite fatigue and how their properties change as a function of applied cyclic stress.

Isotropic materials, such as metals, tend to fail in fatigue due to the growth of a single dominant crack. Composites have several modes of failure that can all occur in fatigue. These modes include matrix microcracking, debonding, delamination and fiber breakage and pullout [5].

Even though there are more modes of fatigue failure in composites than in metals, composites generally react more favorably to repeated loading than metals. The growth of damage in composites is not as abrupt and hence, less dangerous than metals, where damage can be slight until a certain threshold number of cycles is reached at which point exponentially increasing damage occurs until failure [6].

This study will characterize the damage that occurs in unidirectional and bidirectional lay-ups of a Silicon Carbide reinforced ceramic matrix composite. The modes of fatigue failure will be investigated to see what are the primary causes of fatigue failure in this CMC. In addition, the specimens to be fatigue tested will be centrally notched with a single hole. Holes in materials serve several purposes. They can be used as a fastening point for a bolt or they can be used to provide access from one side of a plate to another. Geometric discontinuities generate stress fields near the discontinuity that are much higher than the far field stress. The effect of a hole on the behavior of a CMC versus unnotched specimens under fatigue will also be studied.

B. Approach

The composite being studied, SiC/1723, is a silicon carbide reinforced aluminosilicate glass. It has been the subject of several studies done by the Air Force Materials

Laboratory, Ceramics Division. Their work had focused on the unnotched fatigue behavior while this thesis will expand to include centrally notched specimens. Tension-tension fatigue testing will be done using a minimum to maximum stress ratio of .1. Stress versus strain curves over specimen lifetime and elastic modulus reduction over life will be generated to see how stress level affects composite life. A failure stress versus number of test cycles (S-N) curve will also be generated to see if there is some relationship that can be used to predict the behavior of notched ceramic composites.

Two different orientations will be utilized. Unidirectional and bidirectional laminates will be tested. This thesis will only be concerned with one hole diameter to specimen width ratio (D/W) of .26. Acceptable tolerance is .02 either side of .26. Future work should include varying the D/W ratio to learn if this has any effect on fatigue life for this composite.

Several non-destructive evaluation techniques will be used to evaluate, microscopically and macroscopically, what classical failure modes are present in each laminate. These techniques inclued acetate film replicas, ultrasonic C-scans, X-Ray radiography, scanning electron microscope and modulus degradation.

Several analytical models that have previously been utilized for fatigue life prediction in metal matrix composites and graphite/epoxy will be applied to determine if

they can characterize the fatigue life of SiC/1723. The models include total ply discount method utilizing elements of classical laminated plate theory, the Whitney-Nuismer model, the Fatigue Modulus Concept and the Elastic Modulus Degradation Model.

II. Analytical Background

In order for new materials such as ceramic matrix composites to be readily applied in engineering applications, their behavior must be able to be predicted. To do this, research expands in two directions; experimentally, where a material's response to external stimuli is determined in the laboratory, and analytically where models of the material's response are formulated in the hopes that the model can apply to a large spectrum of environmental inputs. A model is considered satisfactory only when actual data can be used in the proposed model and the output from the model closely resembles that of the material's actual response.

Experimental research that has been accomplished will be covered in detail in Chapter IV. The focus of this chapter will be to expand on research that has been accomplished on fatigue models for composites. This research can be broken down into three components. First are fatigue models based on damage accumulation or stiffness reduction. Second, are models that apply a statistical approach to composite fatigue life. Lastly are models based on the strength or residual strength of the composite. Examples of each will be presented and the models used in this project will be presented in detail. As will be seen, there is no model developed specifically for CMCs. Most research has centered on either metal matrix or polymeric composites.

Composites differ from metals in terms of fatigue failure significantly. Metals tend to fail due to the catastrophic growth of a single crack. Using linear elastic fracture mechanics methods, the crack growth in a metal can be predicted with a good degree of accuracy. However, composites have several modes of failure that can occur in any combination [7].

The composites' modes of failure include matrix microcracking, delamination, debonding, which is the separation of fiber from matrix, fiber pullout and defects due to manufacturing such as voids and fiber/matrix density variation. The randomness that these modes can appear during fatigue of composites make model predictions extremely difficult to make.

Kulkarni et al [8] presented data on boron/epoxy laminates that were fatigue tested in tension-tension. They applied their data to the "Mechanistic Wearout" model developed by McLaughlin et al to see if centrally-notched boron/epoxy fatigue life could be predicted. This model was originally used for static tests but was extended to fatigue. The philosophy underlying this model is the wearout concept [9]. The authors state that, "...repeated application of load results in material degradation and changes in residual properties. When the residual strength is reduced to the level of applied loads, failure occurs." In their experiments, the authors had to characterize lamina behavior

and properties in the region of the notch. With these changed properties, they were able to predict the residual strength and failure of the laminate.

Kulkarni et. al. were able to predict certain fatigue phenomena such as residual strength increase after loading. The damage zone predicted by the model, axial and transverse, was observed experimentally. However, their correlation between theory and experiment was hampered by delamination of 0^0 surface layers in the region of the notch diameter (not predicted) and the lack of a statistically significant data base for lamina fatigue properties in general.

Hahn proposed a statistical approach to determining fatigue life [10]. This approach eliminates the need for specific information about the failure modes of composites [11]. Hahn proposed two models based on statistics. The first model was based on failure rate and failure potential. He determined the material "age", T, as the key parameter, replacing real time (test time). Material age represents the aging of the material in the same fashion as the strain-hardening parameter is a measure of the plastically deformed state in metals [12]. The failure potential, Ψ, is then introduced such that the failure rate is its derivative with respect to the material age. Hahn states that the load history, $\sigma(t)$, can be related to the material age by:

$$T=\int_0^t K[\sigma(\zeta)]\,d\zeta \qquad (1)$$

where K is called the breakdown rule.

In addition, Hahn asserts;

$$\Psi = T^{\alpha} \tag{2}$$

$$K = C\sigma^{\gamma} \tag{3}$$

α, C and γ are constants.

The probability of surviving the failure stress, X, in static tension, based on the characteristic strength, X_0, has been given previously by Tsai and Hahn, Coleman and Phoenix as;

$$R_s(X) = \exp\left[-\left(\frac{X}{X_0}\right)^{\alpha_s}\right] \tag{4}$$

where X_0 depends on the constants and α_s is given by;

$$\alpha_s = \alpha(\gamma + 1) \tag{5}$$

This yields Hahn's model for fatigue which is a three parameter Weibull distribution:

$$R_f(T) = \exp\left[-\left[\left(\frac{S_{max}}{X_0}\right)^{\gamma+1} + T\right]^{\alpha}\right] \tag{6}$$

where S_{max} is the maximum tensile stress in fatigue.

The author also proposed the residual strength of the composite as the critical factor of the damage. Using a

derivation similar to the above model [13], he obtained a probability life distribution, $R_f(T)$ equivalent to equation 6. Hahn states that these models have only been used to analyze data and that their success at predicting life has yet to be seen. These models were not applied to this project due to the lack of a statistically significant number of specimens available for testing.

There are two ways to apply damage accumulation into a fatigue model. One may attempt to identify the exact damage modes in a composite. The growth progression of these modes must then be followed taking into account interactions between loading, specimen geometry and lay-up and also the interactions between the damages themselves [14]. This is the optimum approach but due to the number of damage modes and their randomness it would be exceedingly complex.

Another approach is to consider some measurable external quantity which is directly affected by all of the internal damage modes. For tensile-tensile fatigue tests, the elastic modulus in the longitudinal (loading) direction, E_x, is a parameter considered by many as that key measurable quantity. Since all tests in this project measured E_x, the following models were applied to SiC/1723 to predict fatigue life.

A model based on stiffness reduction has been recently developed by Jen, Hsu and Hwang [15]. They attempted to model the reduction in elastic modulus and predict fatigue life of $[0/90/+45]_{2S}$ graphite/epoxy centrally-notched

specimens under tension-tension loading. The authors assumed for constant cyclic stress levels, the elastic modulus will degrade as a power function of applied cycles, N. They postulated this relationship as follows;

$$\frac{\Delta E}{E_0} = A(N)^c \tag{7}$$

where ΔE= change in stiffness

E_0= initial stiffness

A,c= test and material dependent constants

Taking the logarithm of eq (7) yields;

$$\log\left(\frac{\Delta E}{E_0}\right) = \log(A) + c\log(N) \tag{8}$$

A and c can be determined from different cycles in a single test.

The shape of the curve in the $\log(\Delta E/E_0)$ versus $\log(N)$ graph was considered extremely important by the authors. Two graphs from their data are presented in figures 1 and 2.

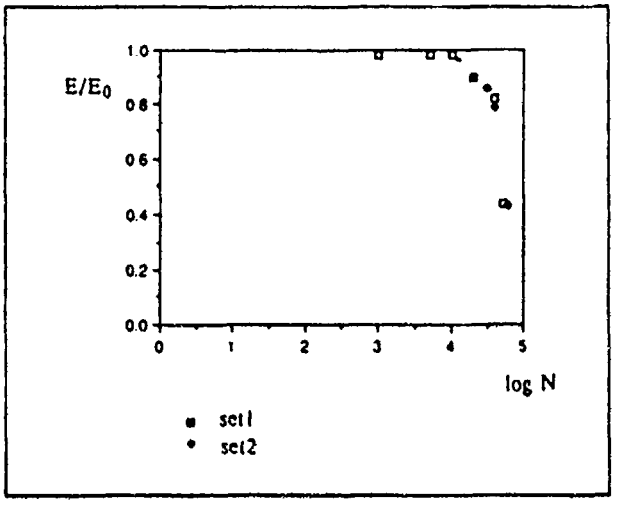

Figure 1 Modulus Reduction Data

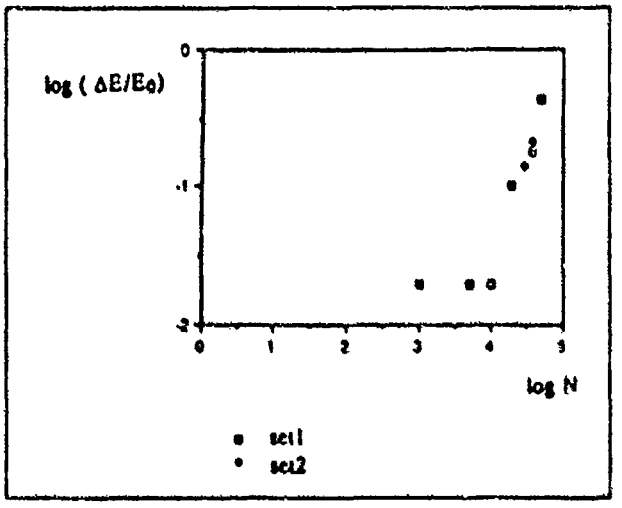

Figure 2 Logarithmic Modulus Reduction Data

Hwang et al. broke up these graphs into three distinct regions. In region one, the reduction in elastic modulus is quite small, due to matrix microcracking. In the second region there is stable and larger stiffness decrease than in the first region. In the third region, the damage goes unstable and specimen failure occurs.

The next step is to shift the curve so the beginning cycle is the threshold cycle between regions I and II. This cycle will be denoted N_i. Equation (8) now becomes;

$$\log\left(\frac{\Delta E}{E_0}\right) = \log(A') + c(\log(N) - \log(N_i)) \tag{9}$$

where;

$$\log(A') = \log\left(\frac{\Delta E_i}{\Delta E}\right) \tag{10}$$

from boundary conditions, $N=N_i$ and $\Delta E_i=\Delta E(N_i)$
Therefore, the final model is;

$$\log\left(\frac{\Delta E}{E_0}\right) = \log\left(\frac{\Delta E_i}{E_0}\right) + c(\log(N) - \log(N_i)) \tag{11}$$

In order to predict the fatigue life, we must introduce the failure degradation of elastic modulus, ΔE_f, as a failure criteria. ΔE_f is the modulus degradation at the failure cycle. The authors determined it was independent of applied load. Therefore if ΔE_f is determined for one test it may be applied for all tests.

Substituting into equation (11), we obtain;

$$\log\left(\frac{\Delta E_f}{E_0}\right) = \log\left(\frac{\Delta E_i}{E_0}\right) + c(\log(N_f) - \log(N_i)) \tag{12}$$

and;

$$N_f = N_i \left(\frac{\Delta E_f}{\Delta E_i} \right)^{\frac{1}{c}} \tag{13}$$

N_f= cycles to failure.

Figure 3 shows the agreement between the proposed model and actual data. The good correlation and the similarity in test conditions were attractive features for applying this model to CMC fatigue.

Set	Experimental Data N_f	N_i	$\Delta E_i/E_o$	$\Delta E_i/E_t$	C	Proposed Model N_f*	Errors %
1[b]	50,000	10000	0.02	0.435	1.8	55,245	10.5
2[b]	60,000	10000	0.02	0.435	1.8	55,245	7.9
3[c]	200,000	7000	0.072	0.29	0.423	189,888	5.056
4[c]	10,000	150	0.072	0.28	0.32	10,454	4.54

Figure 3 Experimental Results Vs. Proposed Model

Hwang and Han [16] developed a power function model based on the concept of fatigue modulus. They assumed fatigue life is a function of the fatigue modulus and behaved according to strain failure criterion.

The fatigue modulus is shown in figure 4 as the line o-n. It is the slope of the stress versus resultant strain

at n^{th} cycles and is given by;

$$F(n,r) = \frac{\sigma_a}{\epsilon(n)} = \sigma_u\left(\frac{r}{\epsilon(n)}\right) \tag{14}$$

where $F(n,r)$: fatigue modulus at n^{th} loading cycle

$\epsilon(n)$: resultant strain at n^{th} loading cycle

σ_a: applied maximum cyclic stress

r: applied stress to ultimate stress, σ_u, ratio

note that

$$F(0,r) = F_0 = E_0$$

$$F(N,r) = F_f$$

E_0 is defined as the initial cycle modulus and F_f is the fatigue modulus at failure cycle, N.

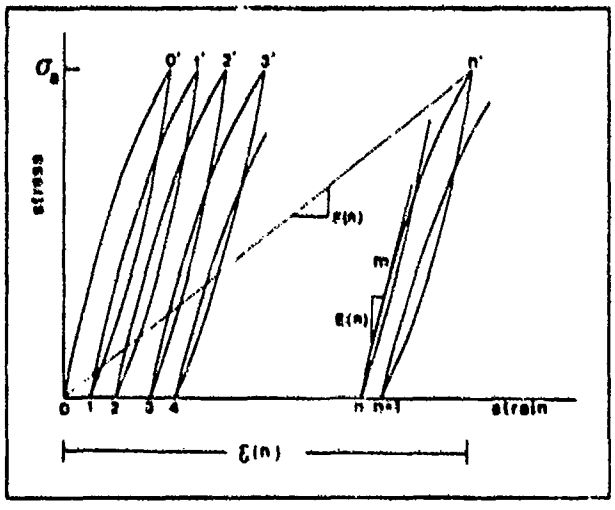

Figure 4 Fatigue Modulus Concept

By assuming that the fatigue modulus behaves as a power function of cycles, the authors arrived at the following equation;

$$\frac{dF}{dn} = -Ac(n)^{c-1} \tag{15}$$

where A and c are material constants.

Integration of (15) yields;

$$F(n_2) - F(n_1) = -A(n_2^c - n_1^c) \tag{16}$$

Substituting equation (14) into (16) gives;

$$F(n) - E_0 = -An^c \tag{17}$$

At failure, n=N and equation (17) becomes;

$$F_f - F_0 = -AN^c \tag{18}$$

Rearranging yields an expression for the number of cycles to failure;

$$N = \left[B\left(1 - \frac{F_f}{F_0}\right)\right]^{\frac{1}{c}} \tag{19}$$

where $B=F_0/A$

Equation (19) may be simplified by applying strain failure criterion. This criterion states that final failure

of a material occurs when the fatigue resultant strain reaches the static ultimate strain [17]. This is given by equation (20).

$$\sigma_u = E_0 \epsilon_u = F_0 \epsilon_u \tag{20}$$

ϵ_u: ultimate strain

Using the fatigue modulus concept, the authors obtained;

$$\sigma_a = F_f \epsilon_f \tag{21}$$

ϵ_f: resultant strain at failure under stress σ_a

Strain failure criterion ($\epsilon_u = \epsilon_f$) allows a relation to be developed between the fatigue moduli and stresses as shown in equation (22).

$$\frac{F_f}{F_0} = \frac{\sigma_a}{\sigma_u} = r \tag{22}$$

Substituting (22) into (19) gives the final form for the model.

$$N = [B(1 - r)]^{\frac{1}{\alpha}} \tag{23}$$

This model was selected due to the fact, as will be shown later, that stress versus strain over test life was determined for all tests in this project. Therefore, fatigue modulus could be easily calculated and the model applied.

The next model to be examined was developed by Whitney and Nuismer. The Whitr y-Nuismer model was originally intended for static tensile tests on specimens with stress concentrations due to notches in the material, ie. holes or cut-outs. It has been successfully extended by others to fatigue on unidirectional composites [18],[19].

Analysis begins by considering a circular hole with radius R in an isotropic plate as shown in figure 5.

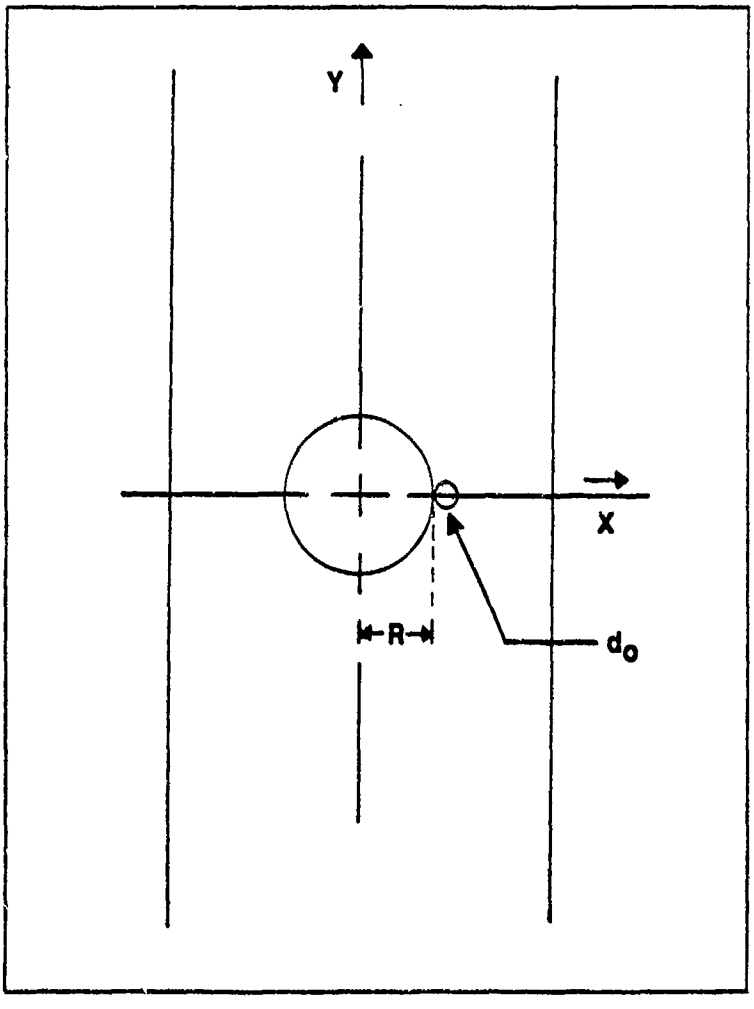

Figure 5 Isotropic Plate With Center Hole

If a uniform tensile stress, σ, is applied at infinity parallel to the Y-axis, then the normal stress, σ_y, along the X-axis is given by Timoshenko and Goodier [20] as

$$\frac{\sigma_y}{\sigma} = 1 + \frac{1}{2}\left[\frac{R}{X}\right]^2 + \frac{3}{2}\left[\frac{R}{X}\right]^4 \qquad (24)$$

Whitney and Nuismer assumed that failure will occur when the stress some distance d_0 along the X-axis away from the discontinuity is equal to or greater than the strength of the unnotched material. They further assumed that this characteristic distance is a material property independent of laminate geometry and stress distribution. Using these assumptions, they obtained their stress failure criterion for an orthotropic plate by applying equation (24) such that;

$$\frac{\sigma_n}{\sigma_0} = \frac{2}{\left[2 + 2X + X^2 + X^3 + (K_T^{\infty} - 3)X^6(1 + X)\right]} \qquad (25)$$

where

$$X = \frac{R}{R + d_0}$$

σ_n - *Notched Strength*

σ_0 - *Unnotched Strength*

The theoretical stress concentration factor, K_T^*, for an orthotropic plate is given by;

$$K_T^{\infty} = 1 + \left[2\left(\sqrt{\frac{E_{11}}{E_{22}}} - \nu_{12}\right) + \frac{E_{11}}{G_{12}}\right]^{\frac{1}{2}} \tag{26}$$

The authors developed a relation to correct for finite width. This correction factor is given by equation (27).

$$\frac{K_T}{K_T^{\infty}} = \frac{\left[2 + \left(1 - \frac{2R}{W}\right)^3\right]}{3\left(1 - \frac{2R}{W}\right)} \tag{27}$$

W is the specimen width.

Tsangarakis extended this model to fatigue. He used Whitney and Nuismer's assumption that the characteristic length, d_0, is a material constant. He let σ_n and σ_0 in equation (25) become the notched and unnotched endurance limits respectively. The endurance limit is that stress that will allow run-out, ie. no failure, in fatigue. His experimental results showed good agreement with values predicted by the Whitney-Nuismer model [21]. This model is applicable to this research because endurance and static strengths of unnotched SiC/1723 are available [22] and the notched static strength will be experimentally determined. Thus, the model can be employed to find the notched endurance limit. This value can then be compared to the experimentally

determined endurance limit for correlation.

The models discussed thus far are to be used for the unidirectional SiC/1723 data. The final analytical tool to be examined will be applied to the $[(0/90)_2]_s$ data. It is called Total Ply Discount method and it uses elements from classical laminated plate theory. It can not be applied to the unidirectional specimens because it assumes total failure of all plies of a certain orientation. Classical laminated plate theory is developed as follows [23].

Start with stress-strain relations for an orthotropic material;

$$\sigma_i = [\, Q_{ij} \,] e_j \tag{28}$$

where $[Q_{ij}]$ is the reduced stiffness matrix for an individual ply in that ply's principal material coordinates. Next, the reduced stiffness of each lamina is transformed to the coordinate system of the laminate. The transformed reduced stiffness is given by $[\overline{Q_{ij}}]$ where,

$$[\, \overline{Q_{ij}} \,] = [T]^{-1} [\, Q_{ij} \,] [T]^T \tag{29}$$

$[T]^{-1}$ is the transformation matrix between lamina coordinate system to laminate or structural coordinate system. The stress-strain relations now become;

$$\sigma_x = [\, \overline{Q_{ij}} \,] (e_x) \tag{30}$$

The transformed stiffness matrices for each lamina are then combined to form the extensional stiffness matrix $[A_{ij}]$. Since this thesis is only concerned with testing in tension and the laminate is symmetric, the coupling and bending stiffnesses need not be computed. $[A_{ij}]$ is given by equation (31).

$$[\,A_{ij}\,] = \sum_{k=1}^{N} [\,\overline{Q_{ij}}\,]_k t_k \tag{31}$$

t_k: thickness of k^{th} ply

N: total number of plies

Now we go to the laminate stress-strain relations. For a symmetrical lay-up with no bending, the following relationship exists.

$$\begin{bmatrix} N_x \\ N_y \\ N_{xy} \end{bmatrix} = [\,A_{ij}\,] \begin{bmatrix} \epsilon_x^{\,o} \\ \epsilon_y^{\,o} \\ \gamma_{xy}^{\,o} \end{bmatrix} \tag{32}$$

where: $N_{x,y}$ = normal force resultant in x,y direction (per unit width)

N_{xy} = shear force resultant (per unit width)

The longitudinal modulus that will be measured in this study is given as;

$$E_x = \frac{\sigma_x}{\epsilon_x^o} \tag{33}$$

Testing will only be in the X-direction, therefore, set N_y and N_{xy} equal to zero. Equation (32) is then inverted to obtain strain as a function of load. The result is shown below.

$$\begin{bmatrix} \epsilon_x^o \\ \epsilon_y^o \\ \gamma_{xy}^o \end{bmatrix} = [\, A_{ij} \,]^{-1} \begin{bmatrix} N_x \\ 0 \\ 0 \end{bmatrix} \tag{34}$$

However, $\sigma_x = N_x h$, where h is the specimen thickness. With the equation above, the longitudinal modulus is given as;

$$E_x = \frac{\sigma_x}{\epsilon_x^o} = \frac{A_{11}A_{22} - A_{12}^2}{hA_{22}} \tag{35}$$

The initial stiffness of the bidirectional laminate can now be calculated. To the apply total discount method, set the reduced stiffnesses of the 90^0 plies to zero. Tracy [24] found as the stiffness decreased below the discounted stiffness level, failure in a specimen in fatigue occurred. This technique can also verify certain damage modes as will be shown in chapter four. This method shall be used with the bidirectional specimens to see if it is applicable and affected by the presence of a hole in the specimen.

III. EXPERIMENTAL SET-UP AND PROCEDURE

The focus of this chapter will be to describe the modifications and alignment procedures used to prepare the 22.24 kN MTS tensile test machine for fatigue testing. This machine is located in building 640, room 150. In addition, The SiC/1723 system will be described as well as methods that were used for specimen preparation and test procedures. Finally, the non-destructive evaluation techniques used in the present study will be discussed in detail.

A. Test Station Modifications

The 22.24 kN MTS tensile test machine has been used previously by Tracy [24] to investigate the fatigue properties of a ceramic matrix composite. He developed a rigid grip system which developed its gripping power from an air-driven fluid pump that takes pressurized air from an established line and converts that pressure to hydraulic pressure which closes the grips, thus, securing the specimen. One grip was connected to the load cell transducer via several spacers. The second grip was attached to a Wood's metal pot which was connected to the actuator piston. An anti-rotation device was developed to prevent any rotation of the actuator during actual testing. Since CMCs are susceptible to failure in torsion, this device was essential in ensuring torsion stresses were kept to a minimum. Further

details of the station set-up are given in reference [24].

Several modifications of this system were necessary before fatigue testing could be accomplished. The grips that had been used had experienced severe wear and were not recommended for further use. A new set of grips was made to the same dimensions as the previous grips; see figure 6 for actual dimensions. However, holes were drilled in the new set to provide a passage for water cooling in the event high temperature testing is conducted on this machine.

The anti-rotation device consisted of a stainless steel pin rigidly mounted on an aluminum block which was attached to a base plate on the test stand. The pin slid vertically in a machined groove that was cut into an aluminum collar on the actuator. Tracy encountered difficulty with the pin binding in the groove when specimens failed, severely bending the pin's holding fixture. In order to alleviate this problem, the aluminum block and steel pin were modified. The pin was extracted from the block and press fit on to a rotating shoulder bearing. The bearing was then press fit into the aluminum block and reattached to the holding fixture. This modification allowed the pin to rotate freely as it moved vertically in the actuator collar groove, eliminating any binding.

The spacers that had been used between the upper grip and the transducer were eliminated. Instead, two locking rings were installed which provided a better capability for

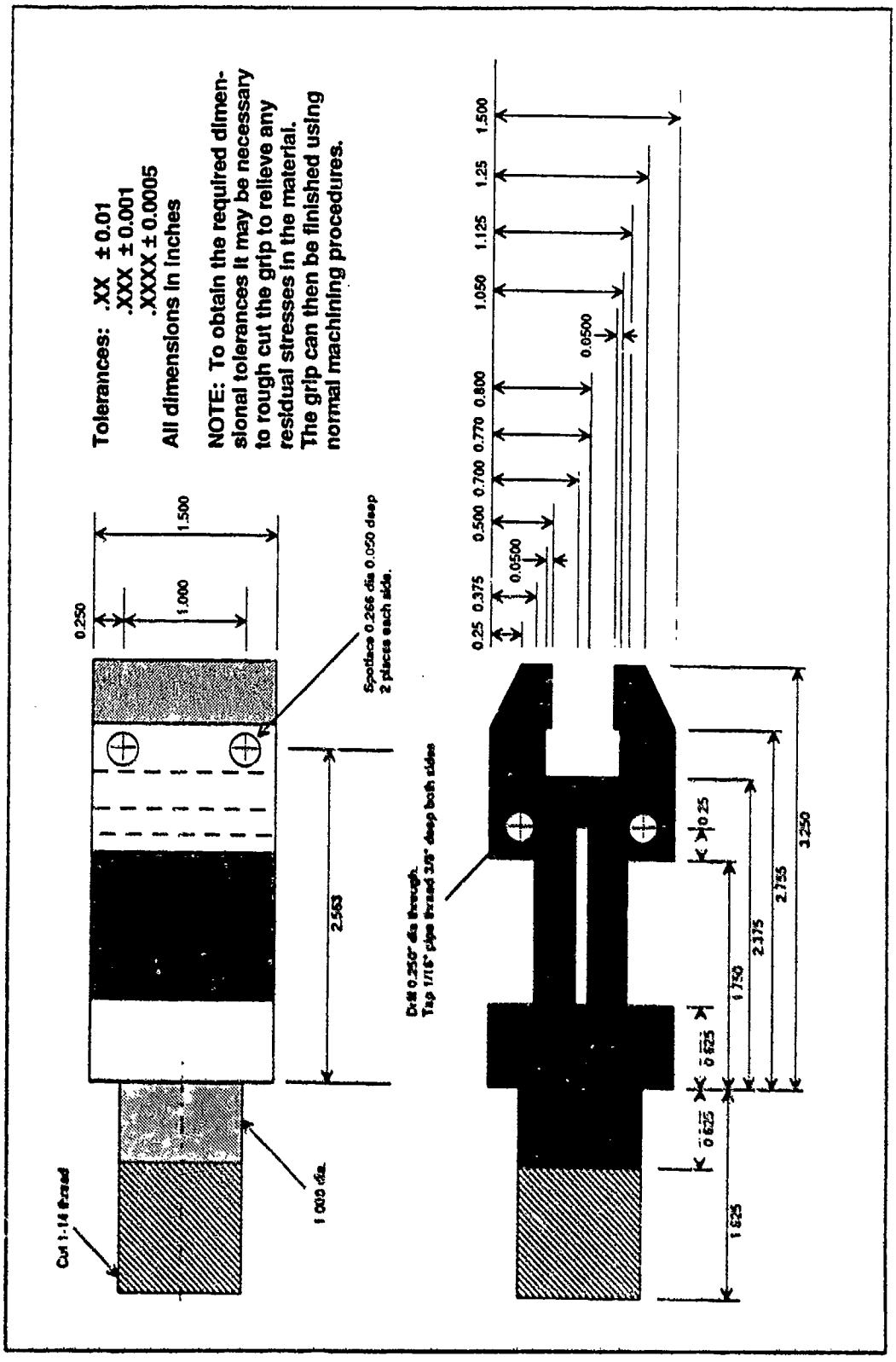

Figure 6 Grip Dimensions

the grip to remain in a fixed position.

The grips were then aligned with each other using two 90^0 angle brackets. Two heat lamps were placed on each side of the Wood's metal pot. The pot consisted of an outer stainless steel cylinder which held a much smaller diameter steel plug inside it. The lower grip was attached to the plug. Wood's metal filled in the gap between the plug and the outer cylinder. Wood's metal is a bismuth, tin, lead and cadmium alloy with a 71.1^0 melting point. When the two lamps were activated, the Wood's metal melted allowing the plug to move freely in the outer cylinder. The brackets could then be clamped over the grips, aligning them nearly perfectly. The lamps were removed and the Wood's metal allowed to cool. After cooling, the brackets were removed and excellent alignment was obtained.

The final modification consisted of removing the MTS 436 Control Unit, MTS 406 Controller and the MTS 408 Modular Testing Panel. These devices were replaced by a more efficient MTS 458 Microconsole. The fatigue testing would be run by an IBM PC-AT and a Wavetek model 75 waveform generator. Both devices would control the MTS 458 Microconsole.

The final system configuration consisted of a data display monitor, signal amplifier, A/D converter, computer, waveform generator, tensile test unit and microconsole. It is shown in figure 7. The gripping system is shown in fig. 8.

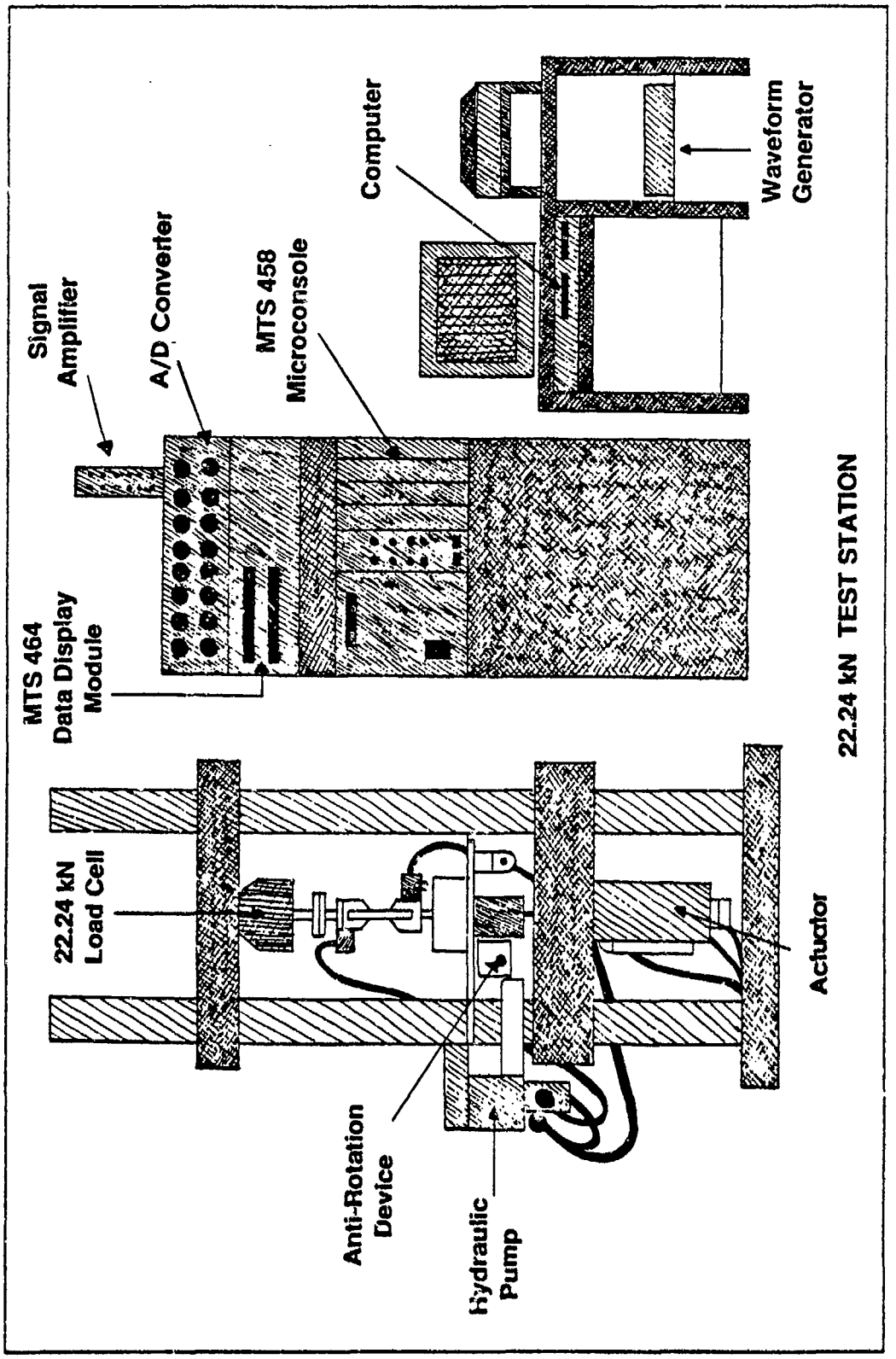

Figure 7 Test System Configuration

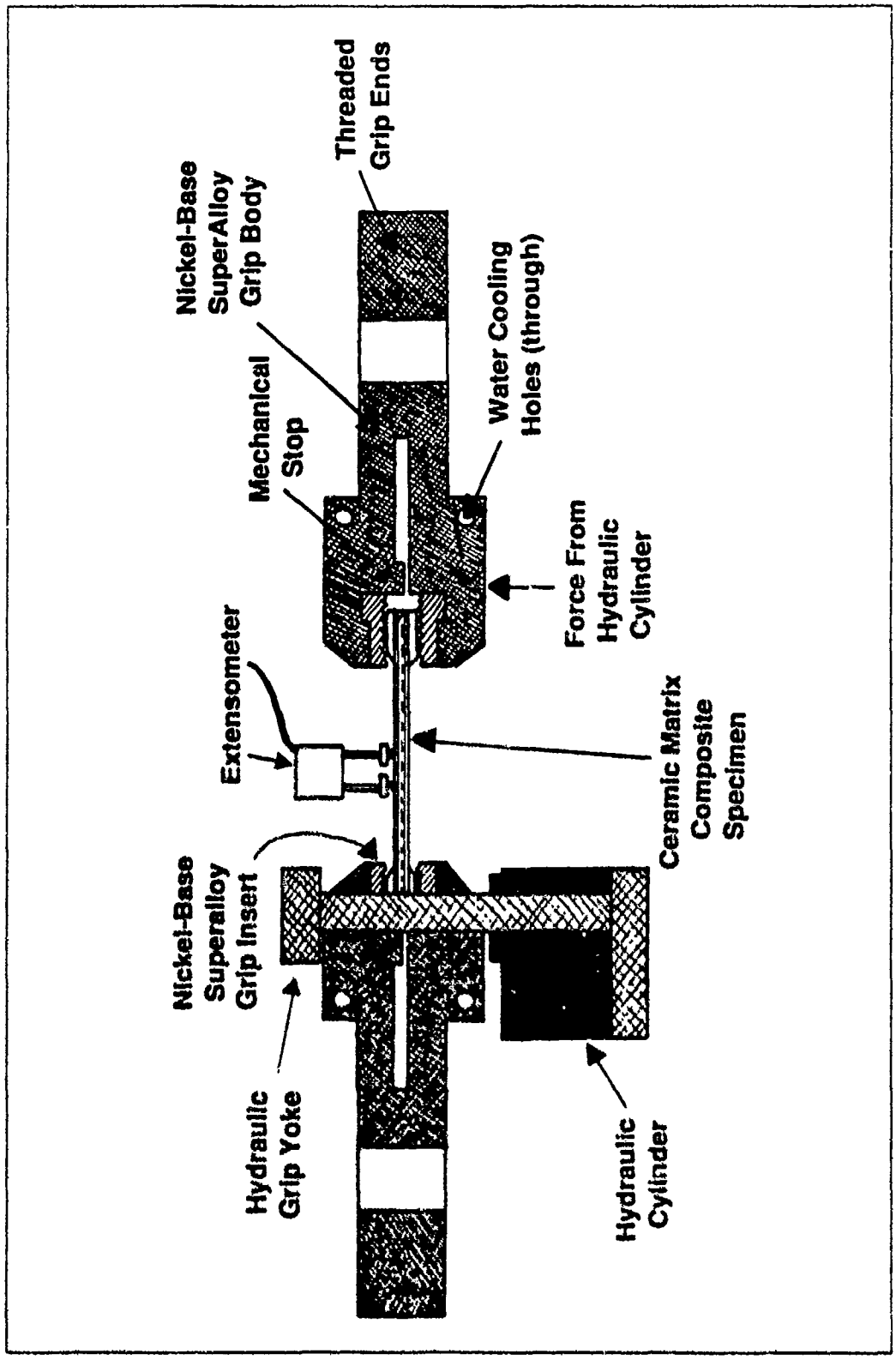

Figure 8 Specimen Gripping System

B. Test Station Alignment Proof Testing

Once the grips had been aligned as described in part A., it was necessary to run two proof tests to ensure bending was kept to a minimum. One test chosen was developed by the Ceramics Division of the Air Force Materials Laboratory. The second test used was from the American Society for Testing and Materials (ASTM). ASTM proposed a standardized test for tensile test alignment.

The former test involved using a dial indicator to determine alignmnet of the grips with the servoram actuator and with each other. The dial indicator had a magnetic base that was attached to a fixed support on the tension test machine. The dial indicator was positioned so that it contacted a flat surface on the lower grip. This grip was attached to the servoram such that lateral movement of the ram could be recorded. The ram was then moved vertically using manual control a total of 50.8 mm. Ram movement was considered adequate if there was less than .0254 millimeters of lateral movement on each of two orthogonal surfaces over 50 8 millimeters of vertical movement of the ram. The results of this test indicated lateral movement was within acceptable limits. The test configuration is shown in figure 9.

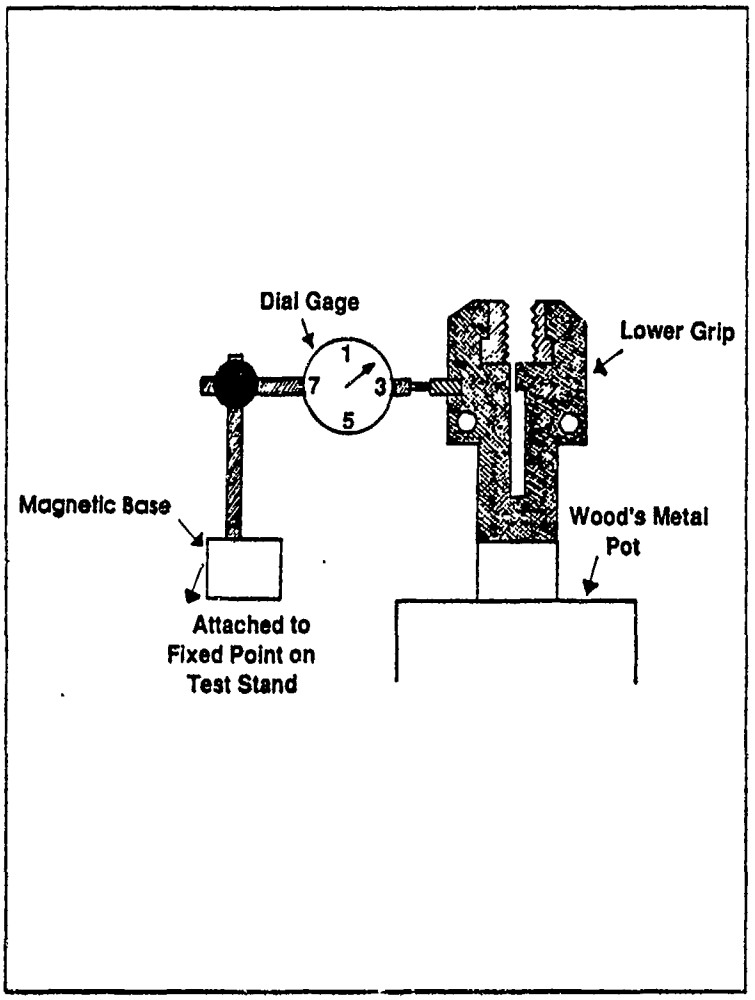

Figure 9 Alignment Test One Configuration

The second part of this test involved mounting the magnetic base of the dial indicator to the lower grip and setting the indicator on to a flat surface on the upper grip. Once again, the indicator was positioned such that lateral movement could be recorded. This test was considered successful if there was less than .0254 millimeters of lateral movement on each of two orthorgonal surfaces.

As before, the results of this test indicated lateral movemnent was within acceptable limits. The configuraton for this test is shown in figure 10.

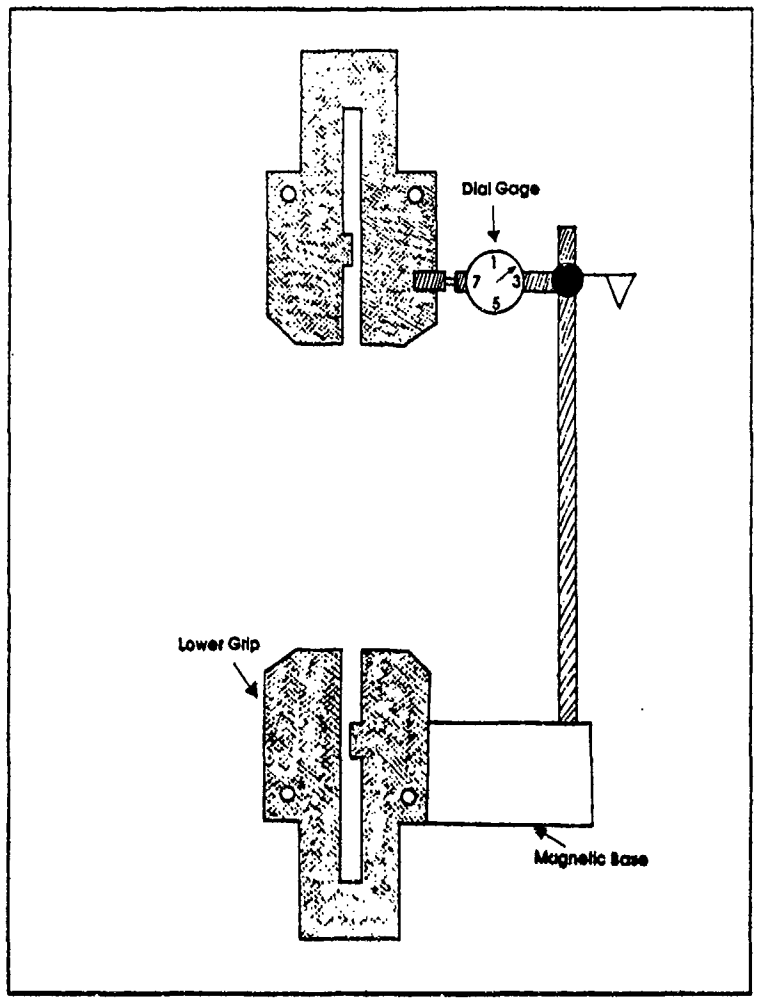

Figure 10 Alignment Test Two Configuration

The second test, designated ASTM procedure E1012-89, Standard Practice for Verification of Specimen Alignment Under Tensile Loading, was also conducted to increase confidence level in test station alignment.

A square cross-sectioned aluminum specimen was loaded in the grips and an extensometer attached to the gage length of the specimen. The extensometer measured the absolute displacement of the specimen under load over the extensometer's gage length of 25.4 millimeters. This procedure dictates that the strain on each side of the specimen be measured at a specified maximum load based on actual test conditions. The load is then reduced to zero and the extensometer moved to another side of the specimen and load applied again to the level previously reached. This process is repeated until strain on all four sides of the specimen have been recorded at the same maximum load.

Let the strain on each side, i, of the specimen be denoted by e_i. ASTM E1012 defines the axial strain, a, in load direction as;

$$a = \frac{(e_1 + e_2 + e_3 + e_4)}{4} \tag{36}$$

and the local bending strain, b_i as;

$$b_i = e_i - a \tag{37}$$

Note that the subscript indicates the order around the specimen as shown in figure 11.

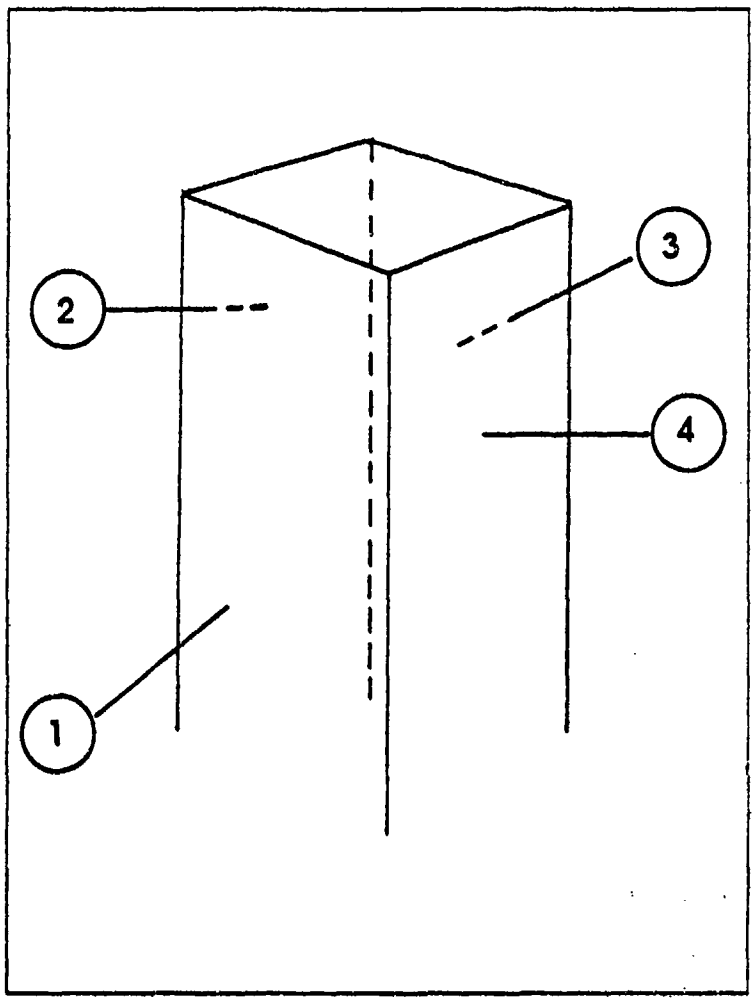

Figure 11 Test Specimen Orientation

The maximum bending strain, B, is calculated as follows;

$$B = \frac{|b_1 - b_3|}{2} + \frac{|b_2 - b_4|}{2} \tag{38}$$

and percent bending, PB, is given by;

$$PB = \left(\frac{B}{a}\right) x\ 100 \tag{39}$$

Several maximum loads were used to determine how bending varied as load was applied. Figure 12 shows the results of this procedure. Percent bending approaches 3.45 percent with loads approaching test conditions. This is in good agreement with results obtained by Butkus and Zawada [22]. This correlation provides excellent confidence that the system is properly aligned. As stated in reference [22], the increase in bending at small loads is somewhat artificial since the bending would become infinite at zero load unless all bending strains were exactly zero. However, at such low load levels, bending does not play a significant role since axial strains are negligible.

C. Specimen Background

The composite being studied is silicon carbide fiber reinforced aluminosilicate glass, designated SiC/1723. This composite has been the focus of several studies done by the Air Force Materials Laboratory Ceramics Division.

In the past, silicon carbide fibers consisted of two categories. Fibers existed in whisker form, which resulted in widely varying properties, both strength and geometric. They were also available in a form produced by chemical vapor deposition. In this process SiC is vaporized and then deposited on a carbon or tungsten core. The result was a fiber that was inflexible and had a large diameter.

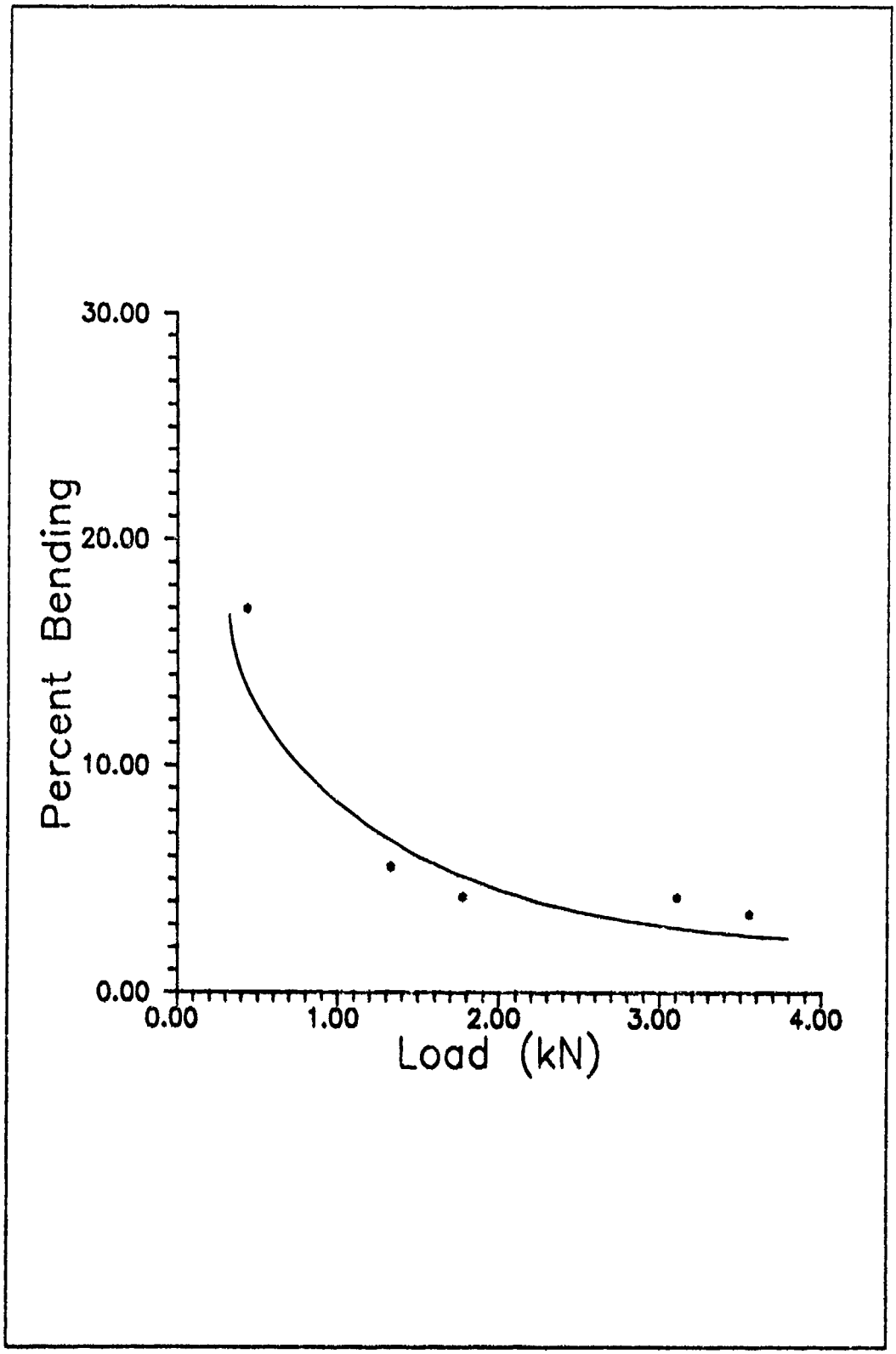

Figure 12 Percent Bending Vs. Applied Load

Yajima [25] developed a third form of SiC fiber that was both flexible and small in diameter. It has the advantage of being able to be formed into complex shapes and also properties that are much more consistent than whiskers.

Yajima started with a polymeric precursor, Dichlorodimethysilane, and through several chemical processes, including melt spinning, curing and pyrolysis, he was able to achieve a flexible, high-strength SiC fiber. The trade name of this fiber is Nicalon and the manufacturing process is shown in figure 13.

Yajima [26] developed a second polymeric precursor SiC fiber by chemically reacting titanium tetrabutoxide ($Ti(OC_4H_9)_4$) with polycarbosilane, see figure 13. This yielded a SiC fiber with titanium. The fiber has an average diameter of 2.54×10^{-4} millimeters. This fiber has strength and modulus slightly higher than Nicalon. Its trade name is Tyranno. Tyranno fiber provided the fiber reinforcement for the composite used in this study.

The matrix material is a silicate glass manufactured by Corning Glass Works. The glass was modified with the addition of oxides of aluminum, magnesium, calcium, barium and boron. The predominant oxide by weight being aluminum oxide. The industry designation for aluminosilicate glass is 1723.

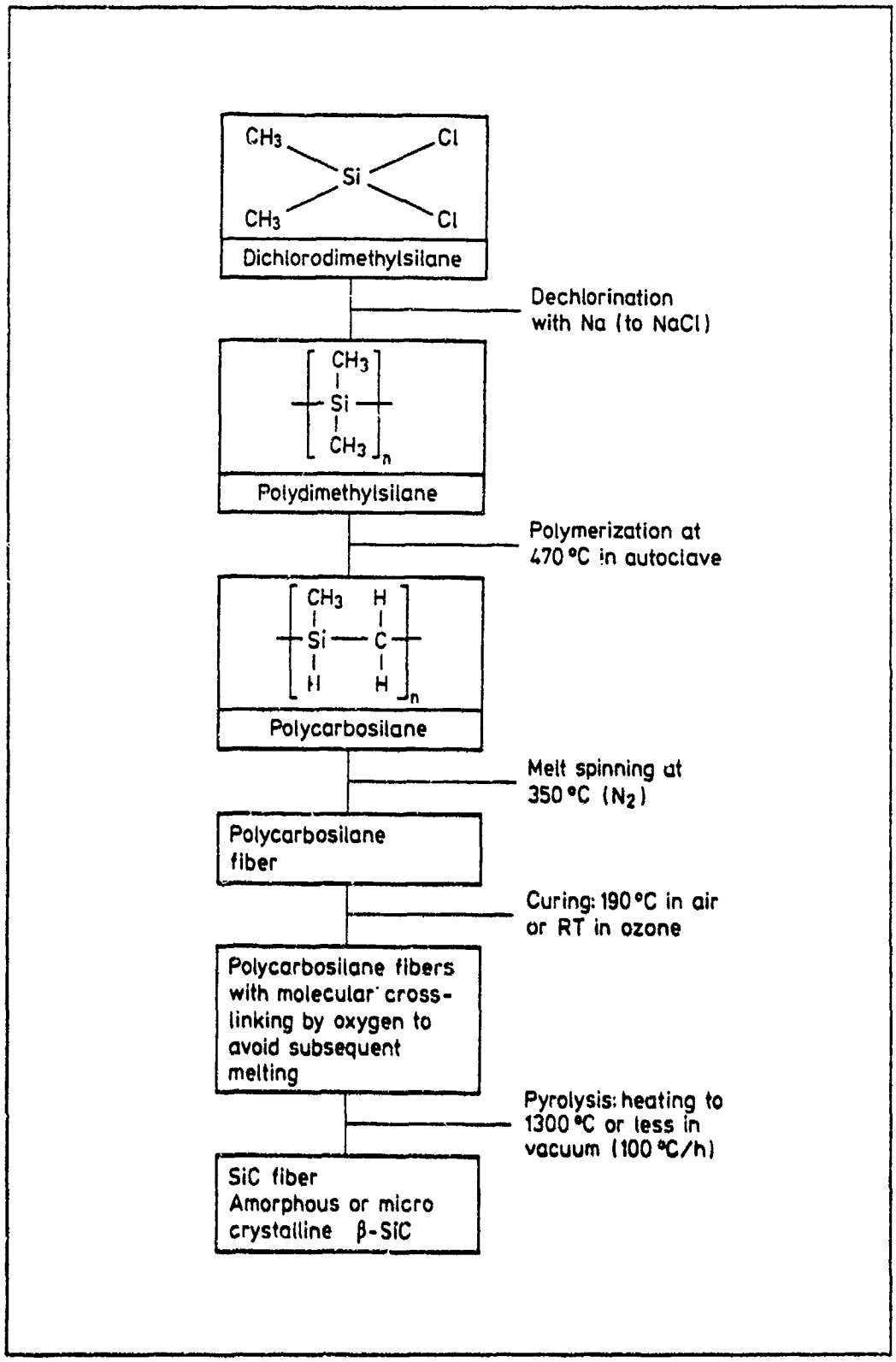

Figure 13 Nicalon Manufacturing Process

The processing of the composites was done at the Materials Laboratory. The Tyranno fibers were drawn through a slurry of 1723 glass frit in powder form, liquid binder and distilled water. The slurry-impregnated fiber yarn was wound on a mandrel and dried. After drying, sheets were cut from the mandrol and laid such that the required laminate stacking sequence was achieved. The sheets were then hot-pressed at high temperature and pressure to yield the final form of the composite.

D. Specimen Preparation

The composite was received as 50.8 mm x 127 mm or 76.2 mm x 127 mm plates. On average, the plates were 2.54 mm in thickness. It was decided that the specimens would have 25.4 mm on each end held by the test station grips. Furthermore, the specimens were designed so they had a gage lenth of 50.8 mm. Therefore, all specimens used in the test were 101.6 mm in length. Testing would only be done on one D/W ratio so the width of all specimens was nearly constant. A D/W ratio of .26 was chosen. The holes were ultrasonically drilled using a 1.524 mm diameter rod. The diamond slurry used by the ultrasonic drill caused the hole to be 1.6 mm in diameter. In order to obtain a D/W of .26, specimen width had to be 5.97 mm.

Plates were cut into specimens using a Buehler Isomet low speed saw. The saw incorporated a diamond cutting wheel which allows for a straight smooth cut. Once specimens had been cut from the plate, they had a hole drilled in the center of them using the Sheffield Bendix ultrasonic drill.

Originally, it had been planned to take acetate film replicas inside the specimen hole to record the damage that occurred. Klang and Hyer [27] obtained excellent replicas from inside the hole of a notched specimen. The surface inside the hole had to be polished to get a good replica. Attempts were made to polish the hole by installing a cloth covered rod into a drill press, then inserting the rod into the hole of the specimen. Diamond slurry and later alumina paste were applied to the hole area and the press was activated. However, the surface could not be polished enough to provide an adequate replica. In addition, the hole diameter was so small that inserting the film into the hole and applying acetate to melt the film to the specimen proved unwieldy and difficult. During actual testing, an extensometer would be attached over the hole allowing very little room for maneuvering. Thus, the author decided this approach would prove impractical.

Due to the fracture behavior of the $[0]_8$ and $[(0/90)_4]_s$ specimens, which will be discussed in Chapter IV, the bidirectional laminates were polished on one edge to obtain an edge replica. Polishing occurred in several stages.

The specimens were gripped in a holding fixture and the edge to be polished was laid on a Buehler grinding wheel. The wheel was covered with a nylon cloth with adhesive backing. Three micron diamond paste was applied to the nylon. The diamond paste was the polishing medium. The nylon cloth was chosen because it did not wear down the specimen at all. Wheels with more abrasive surfaces could grind down the specimen such that the drilled hole would end up off center.

The wheel was set at 200 revolutions per minute. The specimens were held on the wheel for approximately forty-five minutes while diamond paste was constantly applied. After this time, a new nylon covering was put on the wheel and one micron alumina powder was used as a polishing medium. alumina powder allows for greater relief between fiber and matrix in CMCs. This relief allows for replicas of good quality. This step also took an average of forty-five minutes.

The final step was the application of .05 micron alumina powder to a new nylon covering for ultrafine micropolishing. This fine size of powder removed all nicks and grooves caused by the diamond paste. After forty minutes of polishing at this stage, the specimen was polished to an acceptable level for replicas.

Finally, fiberglass tabs were epoxied on the ends of the specimens as shown in figure 14.

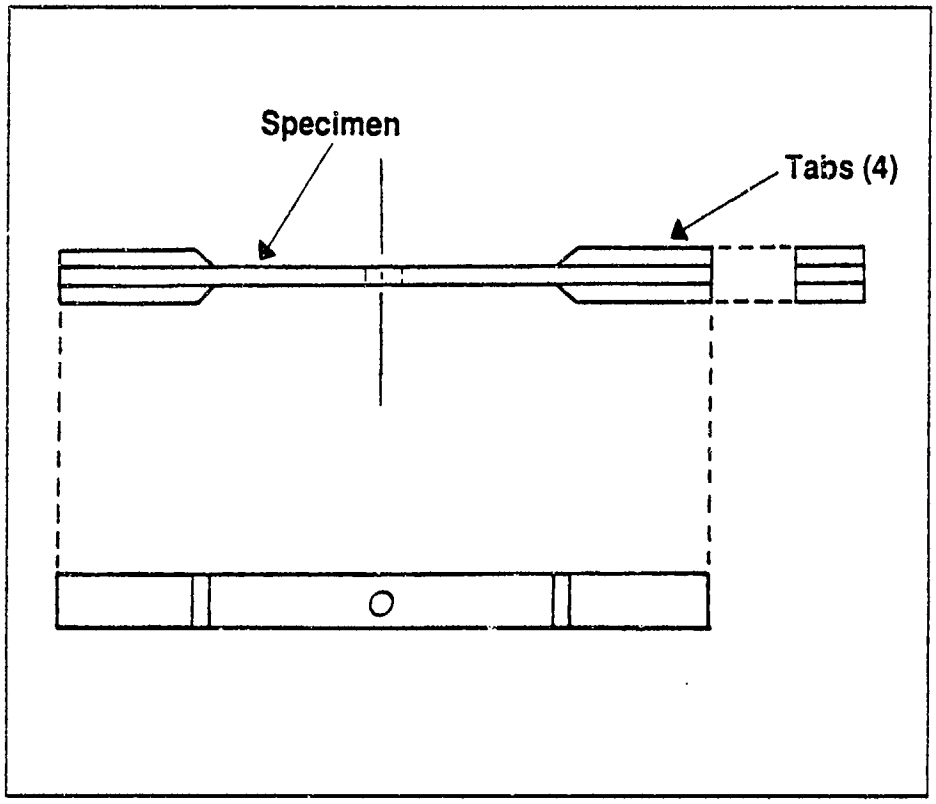

Figure 14 Final Specimen Configuration

These tabs are what would be gripped by the hydraulic grips of figure 8. The tabs absorb the cutting teeth of the grip inserts that will be described in the final section of this chapter. It was imperative that the surface of the specimens remain notch-free since ceramics are very susceptible to failure due to cuts or grooves on their surfaces.

The tabs were applied to the specimens using a 50-50 mixture of EPON brand Epoxy resin and EPON brand V-40 curing agent. After application, the tabs were held on to the specimens by binder clips. The specimens were then placed in an oven at 78.3^{0} Celsius for ninety minutes.

After the elapsed time, the specimens were removed and allowed to sit twenty-four hours. The binder clips remained in place. The specimens were then ready for fatigue testing.

E. Damage Assessment Methods

A portion of this study is to determine the initiation and progression of damage mechanisms during the fatigue testing. This damage assessment must be on the microscopic level as well as macroscopically, therefore evaluation techniques must be sensitive and accurate. Several methods were evaluated with varying degrees of success. These techniques include acetate film replicas, X-Ray radiography, ultrasonic C-scan, scanning electron microscope and modulus degradation. Each method will be discussed and how effective they worked with SiC/1723.

Acetate film replicas have been used successfully in the past on several studies [24],[27]. The procedure involves placing acetate film which has been coated on one side with acetone on to the desired specimen surface. The wetted side of the film comes in contact with the specimen. The film is then gently pressed on the specimen such that trapped air bubbles are forced out. The acetone melts part of the film on the specimen. Once the film has dried it is removed from the specimen with an imprint of the specimen surface melted on the film. The film can then be examined under the

microscope while the specimen continues to undergo testing. As will be shown in Chapter IV, this procedure was quite successful in allowing the author to observe microscopic damage in the specimens.

X-Ray radiography involves applying a dye penetrant, usually Diiodomethane or Iodine, to a specimen and allowing the penetrant to soak into the material. The specimen is then X-Rayed and penetrant that has gathered in cracks or other damage zones shows up prominently. This technique was used to show matrix cracking and delaminations in notched graphite/epoxy specimens under fatigue loading [28]. However, in tests performed in this study, the penetrant did not seem to be able to seep into cracks because no damage could be picked up by the X-Ray. This was the case even though the penetrant was applied while the specimen was under load and on areas where cracks had been detected by acetate replicas.

Ultrasonic scans were also used to evaluate composite damage. The general method in an ultrasonic scan is to apply sound pulses to the material being tested. The waves travel through the object to the far side of the specimen. An extreme change in medium, such as composite to air or water, causes the waves to be reflected back to the sending point as an echo. However, a crack or flaw in the material also represents a change in medium causing an echo to be reflected. This echo reaches the sending point prior to a

pulse that can transmit through the medium, thus indicating a flaw exists on the interior of the specimen. By accurately timing the flaw echo in relation to the transmitted pulse, it can be determined how far into the material the flaw exists [29].

Three different types of ultrasonic flaw detection systems exist. The three are referred to as A-scan, B-scan and C-scan. The difference between the scans is the detail with which a flaw can be detected. A-scans will produce a simple RF or video pulse of the flaw on a CRT display. B-scans will give only two dimensional images of flaws while C-cans have the ability to determine size, shape and depth of flaws [30].

The depth at which a specimen is examined is controlled by a "gating" technique. A gate is a short interval in the scanning time during which a signal is allowed to pass through the scanning equipment amplifiers and be recorded. At other times the system is "dead" [31]. By shifting the gate, information can be obtained at different depths in the specimen. This technique was applied to the test specimens to determine cracks or other damage at each ply in the laminate. Results were good for the composites, especially the unidirectional specimens, as will be shown in Chapter IV.

Elastic modulus reduction is a simple parameter to gage damage accumulation in a composite. It has been used by others [24],[32] to give a quantatative assessment of damage as a specimen is fatigued to failure. The software that was used to run the testing in this project measured the longitudinal modulus, E_x, over the life of the test. Therefore modulus degradation was used extensively as shown in chapter four. The disadvantage to this technique is that damage that occurs cannot be differentiated, ie. microcracks, fiber breakage, delaminations, etc.. Only the cumulative effects of all the damage modes can be recorded.

The final damage assessment tool used was the Scanning Electron Microscope (SEM). This device provided for microscopic examination of the specimens at magnifications much higher than replicas. In addition, photographic quality was typically better than micrographs taken from replicas. Unfortunately, the SEM cannot be classified as non-destructive because specimens had to be cut down to small pieces in order to fit into the SEM examination chamber. Specimens could not be examined during testing until failure or run-out, therefore the SEM was ineffective in monitoring damage progression. It was used though to verify damage modes at the fracture surfaces as will be seen in Chapter IV.

F. Testing Procedures

This section will detail the steps followed in installing and preparing test specimens in the 22.24 kN tensile test station. The initial set-up portion was controlled by the MTS 458.20 Microconsole whose control panel is shown in figure 15.

The hydraulic pressure to the actuator was applied; first at low, then set to high. The actuator could be manually moved by adjusting the set point on the AC controller, shown in figure 15. The ram actuator was manually run through at least 300 cycles of 25.4 mm vertical travel prior to all tests. This step allowed the hydraulic pump and lines to warm up.

The display on the microconsole was switched to the DC controller which provided for load-controlled tests. The hydraulic grip yokes were placed over the grips as shown in figure 8. The microconsole display select switch was set to zero. By adjusting the zero switch on the DC controller, the weight of the hydraulic grip yoke on the transducer could be eliminated. Once this was accomplished, the display select switch was set to transducer output and the span on the DC controller was set to zero, refer to figure 15. Air pressure was supplied to the pump that would pressurize the hydraulic grip yokes. Pressure was initially set at 6.9 MPa. However, the valves that controlled pressure to the grip yokes were

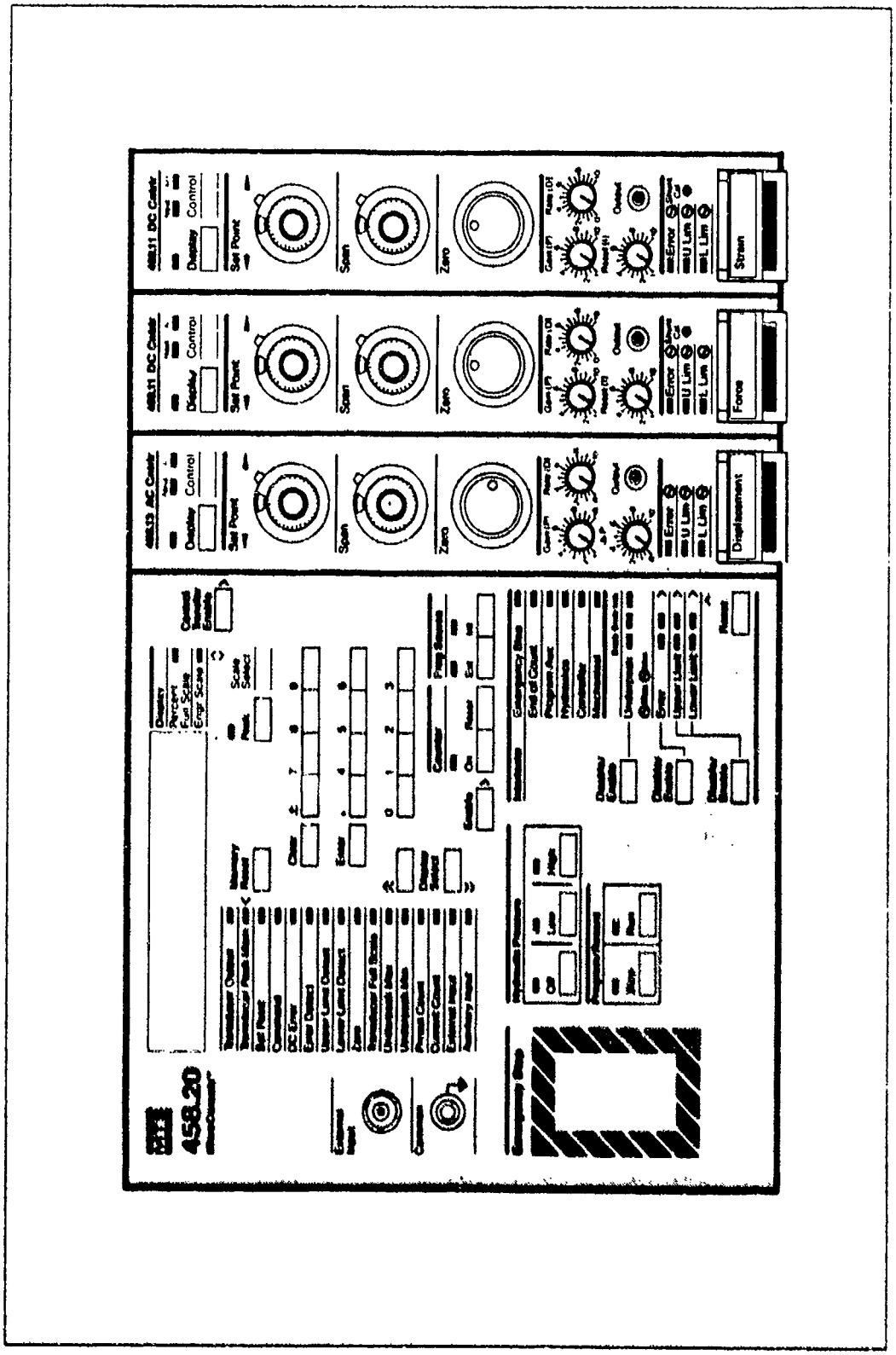

Figure 15 MTS 458.20 Microconsole Panel

kept closed until the specimen was properly aligned. 6.9 MPa grip yoke pressure was selected because at this pressure the grips would just clamp down a specimen. Large increases in pressure on the grips could result in sudden loads imposed on the specimen. The pressure used avoided this problem.

Removable inserts were placed inside the grips as shown in figure 8. These inserts came in various sizes to accomodate specimens of assorted widths. The surfaces of the inserts that came in contact with the specimen had "teeth" machined into them to better hold the specimen.

The specimen was then aligned in the grips and the hydraulic yoke grip valve was opened, allowing the grip yokes to clamp down and secure the specimen in the grips. The air regulator was adjusted to increase hydraulic pressure to the 15.9 to 20 MPa range. Hydraulic pressure was adjusted according to the applied load on the specimen.

If the load controller had not already been selected, it was chosen at this time. Using the set point, load on the specimen was adjusted to zero load. The 4.448 kN load cartridge, seen as "force" on the DC controller, figure 15, was used for all test in this thesis.

An MTS model 632.11B-20 clip-on extensometer was then attached to the middle portion of the specimen and its connector hooked-up to the test station signal amplifier. Once the restraining pin on the extensometer was removed, specimen displacement could be monitored on the MTS 464.80

Data Display Unit. The test was now ready for switchover to software control.

The software used to control the fatigue testing had been developed by George Hartman of the University of Dayton Research Institute. The program, MATE 233, had been used previously at the 22.24 kN test station for CMC fatigue testing [24]. The software provided for load versus displacement measurements at any time in the test.

It was decided that data would be collected logarithmically in all tests. This meant at cycles one, two, five, ten, twenty, fifty, one hundred, etc., load versus displacement data would be stored by the program. Logarithmic data acquisition was appropriate because substantial damage in CMCs occurs during the early portion of cyclic testing. Damage increases slowly after the initial abrupt changes, hence, data acquisition later in the test is not needed as frequently.

Tensile-tensile testing was the form of fatigue testing selected in this study. Throughout the testing, a load ratio of .1 was used. This indicated that the minimum tensile load is one tenth the value of the maximum load. Testing was accomplished at eleven hertz except for the first one thousand cycles. During the first one thousand cycles, the test was cycled at one hertz. A slower frequency was needed because the program was taking many data acquisition cycles at this time. Higher frequencies caused the software to miss

data acquiring at specified cycles.

Once specimen properties and test conditions had been entered into the program, fatigue testing could begin. The first step taken was to make an acetate replica of the specimen. This was accomplished to show the initial state of the specimen. Damage that showed up in later replicas could then be attributed totally to fatigue damage.

Several "check-out" data acquisition cycles were then executed. These cycles were run at 40 MPa maximum stress. At this level, the specimens showed no damage as evidence by their linear stress-strain curves. The program determined initial elastic modulus by using data on the loading portion of the cycle up to a stress of 20 MPa. If after four or five check-out cycles, the modulus approached a constant value, the system was ready for high stress fatigue testing. On all tests, the author had the software measure the initial elastic modulus only on the loading portion with data up to 20 MPa. In this way, modulus degradation could be conveniently referenced against original values determined in the check-out cycles.

Testing was halted periodically to make acetate replicas. This was done to record the growth of microcracks and other damage as the test cycles increased. Actual test levels and how they were determined will be discussed in detail in Chapter IV.

IV. RESULTS AND DISCUSSION

A. Introduction

This chapter will focus on actual tests performed. Results of these tests and how they compare to the work of others will be discussed. In addition, the effects of the stress concentration in the specimens due to the hole will be addressed. Section B will cover all unidirectional tests. Section C will be concerned with test results of the $[(0/90)_4]_s$ specimens. Correlation with the models discussed in chapter two will be covered for each lay-up.

B. Unidirectional Specimens

1. Experimental Results A fatigue study has been done previously by Butkus and Zawada on unidirectional SiC/1723 [22]. They examined unnotched specimens in tension-tension fatigue. Two important conclusions came from their work. First, the proportional limit of the material, defined as the point on the stress-strain curve where subject curve becomes non-linear, was a critical factor in determining whether a specimen survived or failed. If the maximum fatigue stress was above the proportional limit, the specimen would fail. If the maximum stress was below the proportional limit, the specimen would run-out. Run-out was defined as one million

cycles of testing. Prewo [33] also reached this conclusion in fatigue tests which he performed on SiC reinforced lithiumaluminosilicate (SiC/LAS) glass.

The second conclusion reached by Butkus and Zawada was that there was a second critical stress level below the proportional limit. Butkus and Zawada theorized that at a certain stress, matrix microcracking would begin. It was possible for the specimen to run-out above this stress, but damage, as evidenced by longitudinal modulus decrease, was observed. Kim and Pagano [34] performed tensile tests on SiC/1723 and used acoustic emission techniques to record actual matrix cracking occurring above a certain stress level that was below the proportional limit.

Therefore, a static tensile test had to be performed on notched SiC/1723 specimens to determine the non-linearity point on the stress-strain curve. Specimens were prepared from plate 90G03XX, obtained from the Materials Laboratory. Unidirectional testing was also conducted on specimens from plates 90G04XX and 90G07XX. See appendix I for specimen dimensions and test conditions. As will be discussed later, these plates provided specimens that had significantly different failure stresses from plate to plate. This difference had an impact on tests performed.

Three tests from plate 90G03XX were executed on specimens that had D/W ratios ranging from .25 to.28. The stress-strain graph for one specimen is given in figure 16.

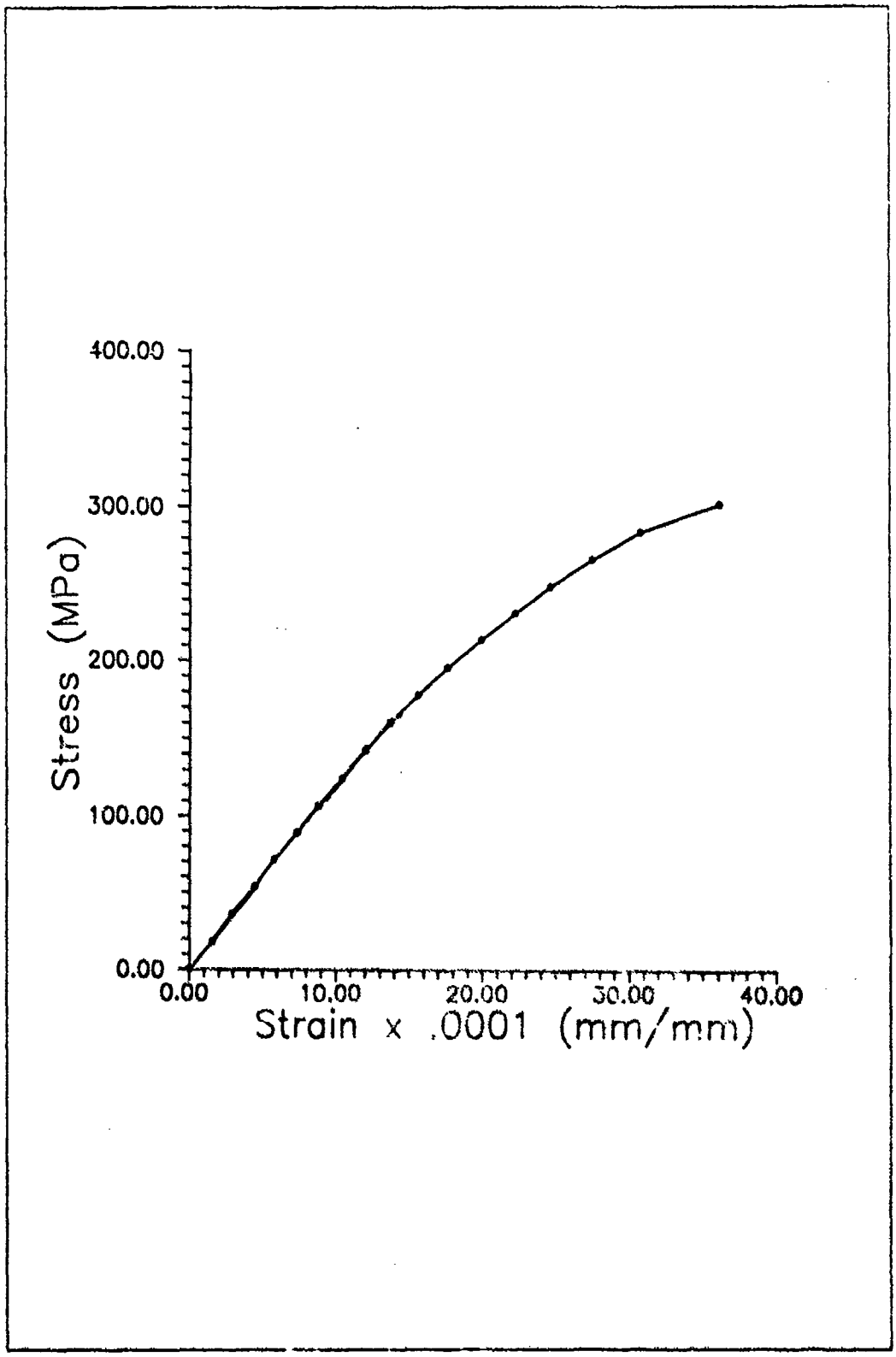

Figure 16 Stress vs. Strain, 90G0303

The proportional limit of the three specimens ranged from 140-170 MPa. The average failure stress was 300 MPa. The specimens all fractured as shown in figure 18.

The effect of the hole was significant since unnotched SiC/1723 had a static failure stress ranging from 550 MPA [35] to 680 MPa [22] and a proportional limit of 400 MPa. Hence, it can be concluded that the notch induces a significant stress concentration causing failure at a much lower level than unnotched specimens. The fracture cracks all emanated near or at the maximum stress concentration points on the hole, at 90^0 and 270^0, see figure 17. (From Jones, Ref. (6), page 290.)

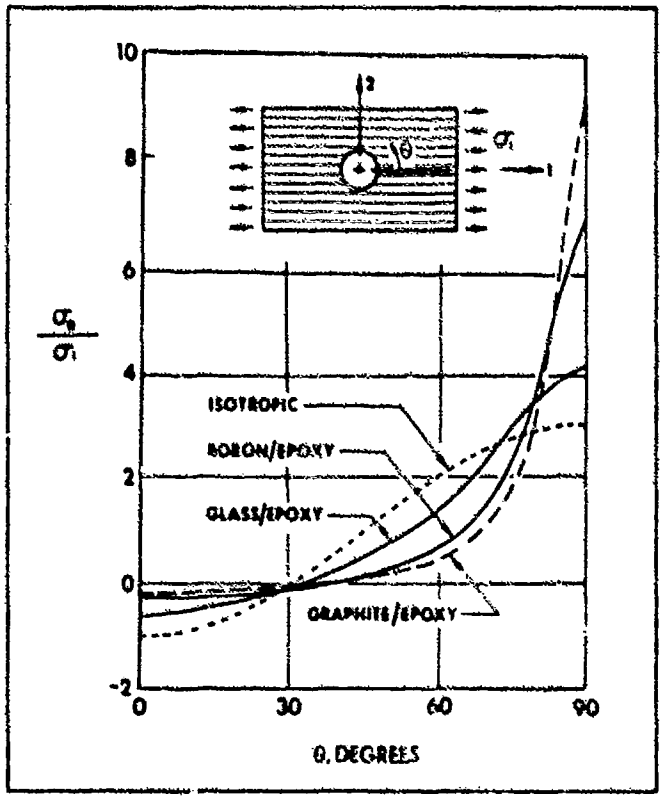

Figure 17 Stress Concentration Values

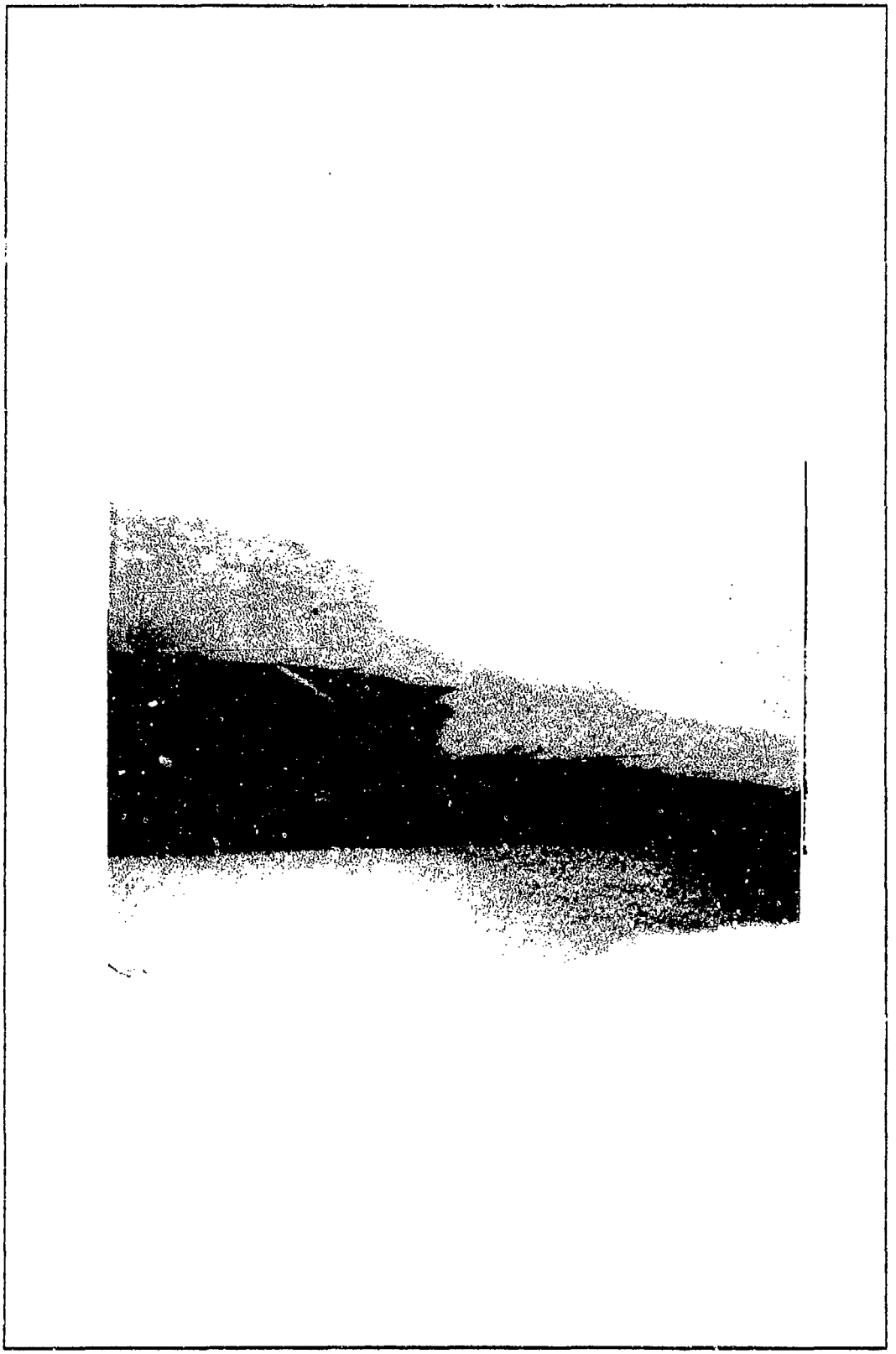

Figure 18 Fracture Surface, 90G0303

The first fatigue test was performed below the proportional limit determined from the static tests. A maximum stress of 130 MPa was chosen. As stated earlier, a load ratio of .1 was used with loading frequency of 11 Hz. The early portion of the test, below 1000 cycles, was run at 1 Hz for data collection purposes.

The objective of this test was to verify that below the proportional limit, a specimen would achieve run-out. A second objective was to determine whether damage would occur due to matrix microcracking, as stated by Kim and Pagano or whether the specimen would remain damage-free as shown in tests done on SiC/LAS by Prewo.

Since cracks that eventually led to failure were emanating from the sides of the hole and propagating longitudinally, the author decided edge replicas would be of little value. Instead replicas were taken across the width of the specimen. In this way, the propagation of the longitudinal cracks could be recorded.

The 130 MPa test results are shown in figure 19 (stress vs. strain over test life cycle) and figure 20 (modulus ratio vs. cycle count). The modulus ratio is defined as the ratio of the longitudinal modulus at cycle n over the modulus calculated for cycle one. As stated in chapter three, the modulus was computed from the linear loading portion of the stress-strain curve. Figure 19 shows stress vs. strain at four particular cycles in the test.

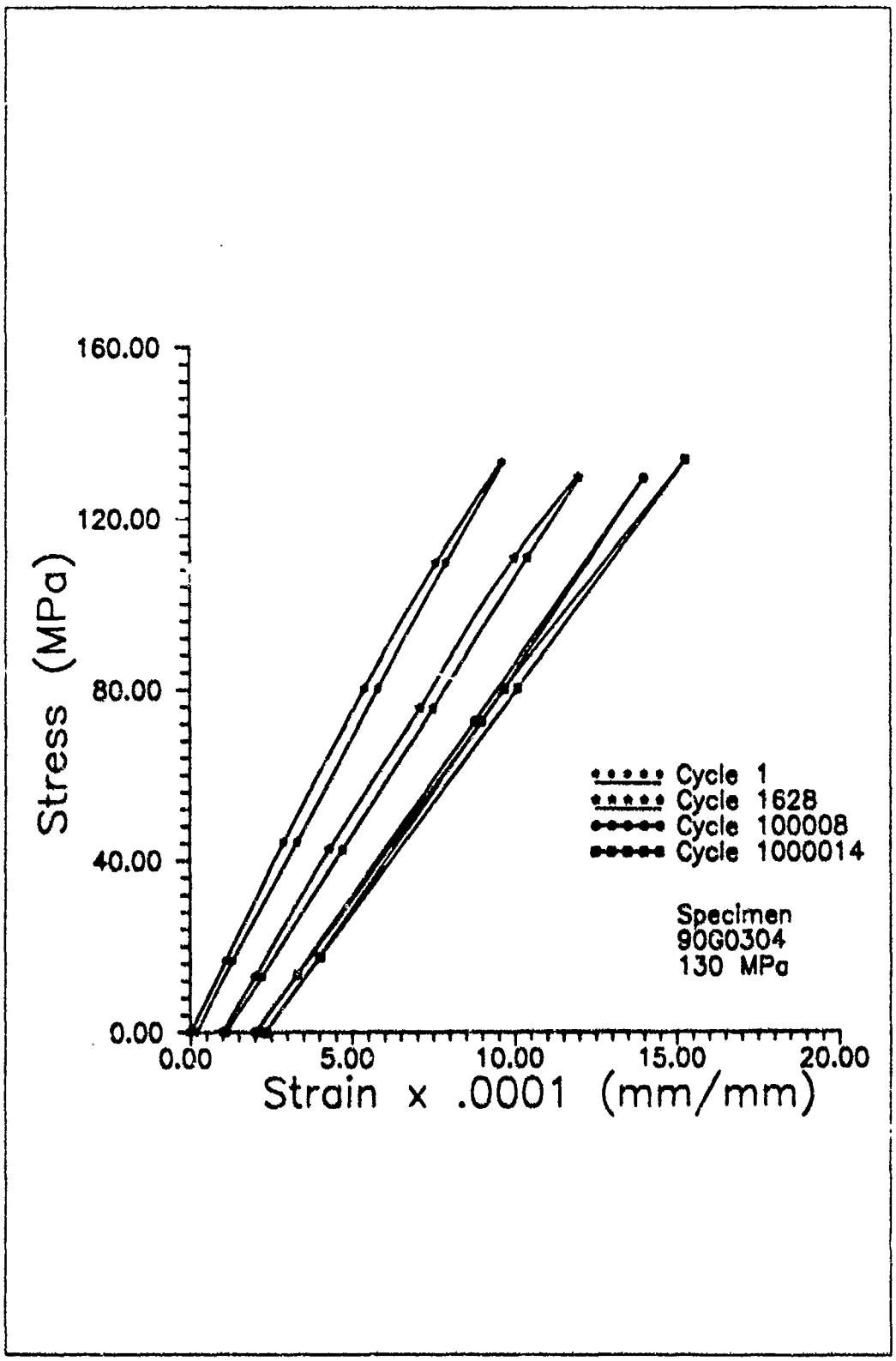

Figure 19 Stress vs. Strain 130 MPa Test

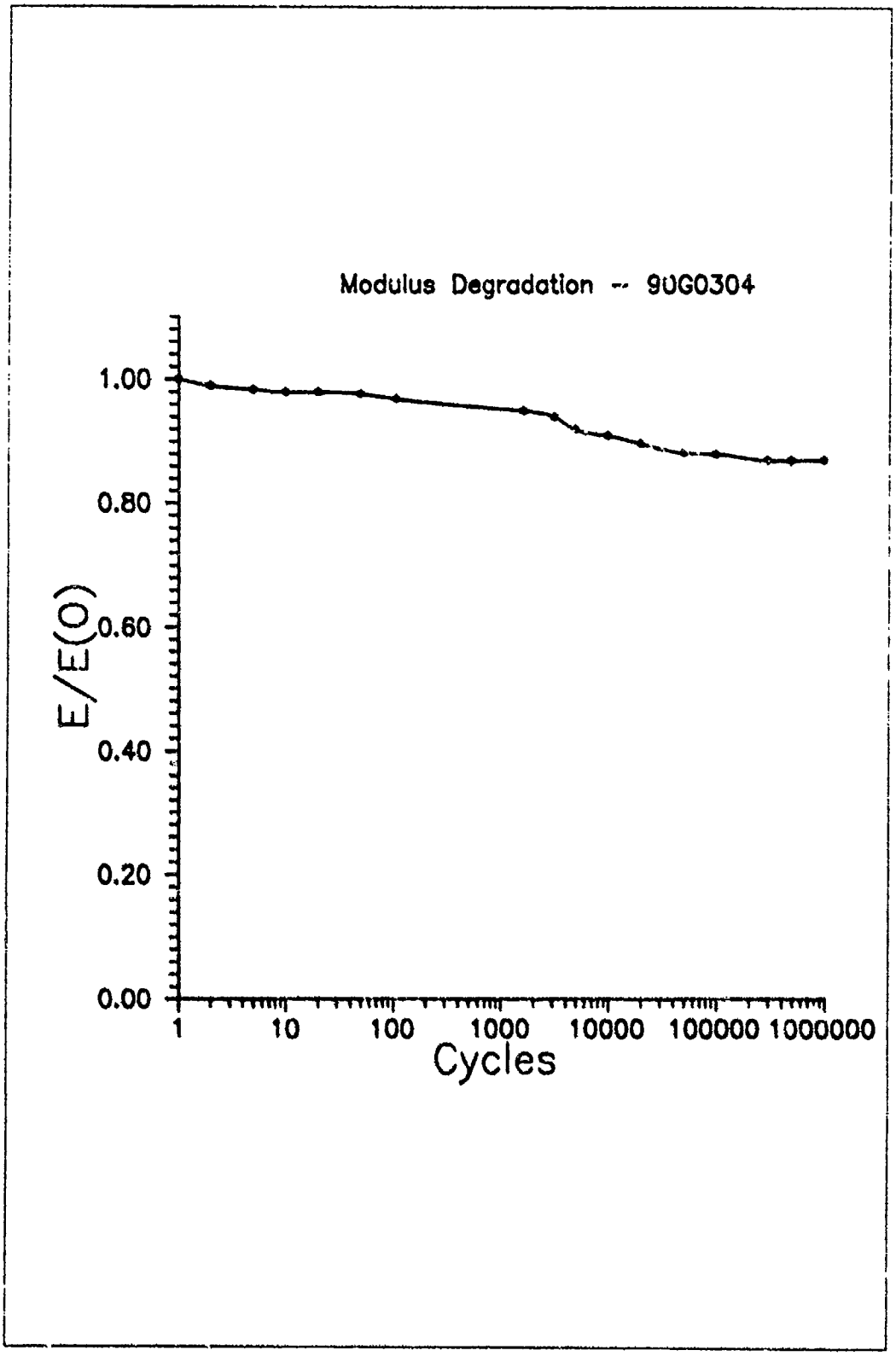

Figure 20 Modulus Reduction 130 MPa Test

This specimen showed very slight non-linearity indicating the test was actually above its proportional limit. There is residual strain accumulation even though it is minor and a change exists in the slope of the curves. This indicates the specimen has undergone damage during the test. This is further supported by figure 20 which shows a decrease in modulus, approximately eight percent, over test life.

The question of what type of damage occurred is of definite interest. Replicas taken showed no damage existing on the surface. Mallick [37] states that in [0^0] laminates, fatigue damage is dominated by matrix microcracking or fiber breakage. In work done by Marshall and Evans [36], matrix microcracking was the initial damage mode observed. This was also observed by Kim and Pagano [34]. Since no cracks were observed in the replicas, a small amount of matrix microcracking must have occurred, all confined to the interior of the specimen. Due to the strength difference between the fiber and matrix, fiber breakage would seem an unlikely damage mode at this stress level. Therefore, notched SiC/1723 does show fatigue damage below or near the proportional limit even though the specimen survived one million cycles of testing.

Maximum stress levels were increased for the next two tests. Specimens 90G0305 and 90G0307 were fatigue tested at

a maximum stress of 140 MPa and 170 MPa respectively. These levels were chosen because they represented the bounds of the proportional limit from the static tensile tests.

Figure 21, stress vs. strain over test life and figure 22, modulus ratio vs. cycle, show the results of testing at 140 MPa. Once again there is a slight accumulation of residual strain indicating damage in the specimen. The results are consistent with the first test since the strain accumulation is only marginally greater the the 130 MPa test. Very slight non-linearity in the stress-strain curves suggest the test levels are definitely close to this specimen's proportional limit. Figure 22 shows a modulus degradation of ten percent, two percent more than test one. This test also showed no surface evidence of damage suggesting matrix cracking was minimal and confined to the interior of the specimen.

The 170 MPa test, specimen 90G0307, was significant because it was the first test in which damage at the surface became evident. This is shown in a replica photograph of the surface in figure 23.

The cracks shown in figure 23 coincide with the fracture surface of figure 18. In all static tests, the specimen broke due to longitudinal cracks, (loading direction), extending from the hole similar to figure 23.

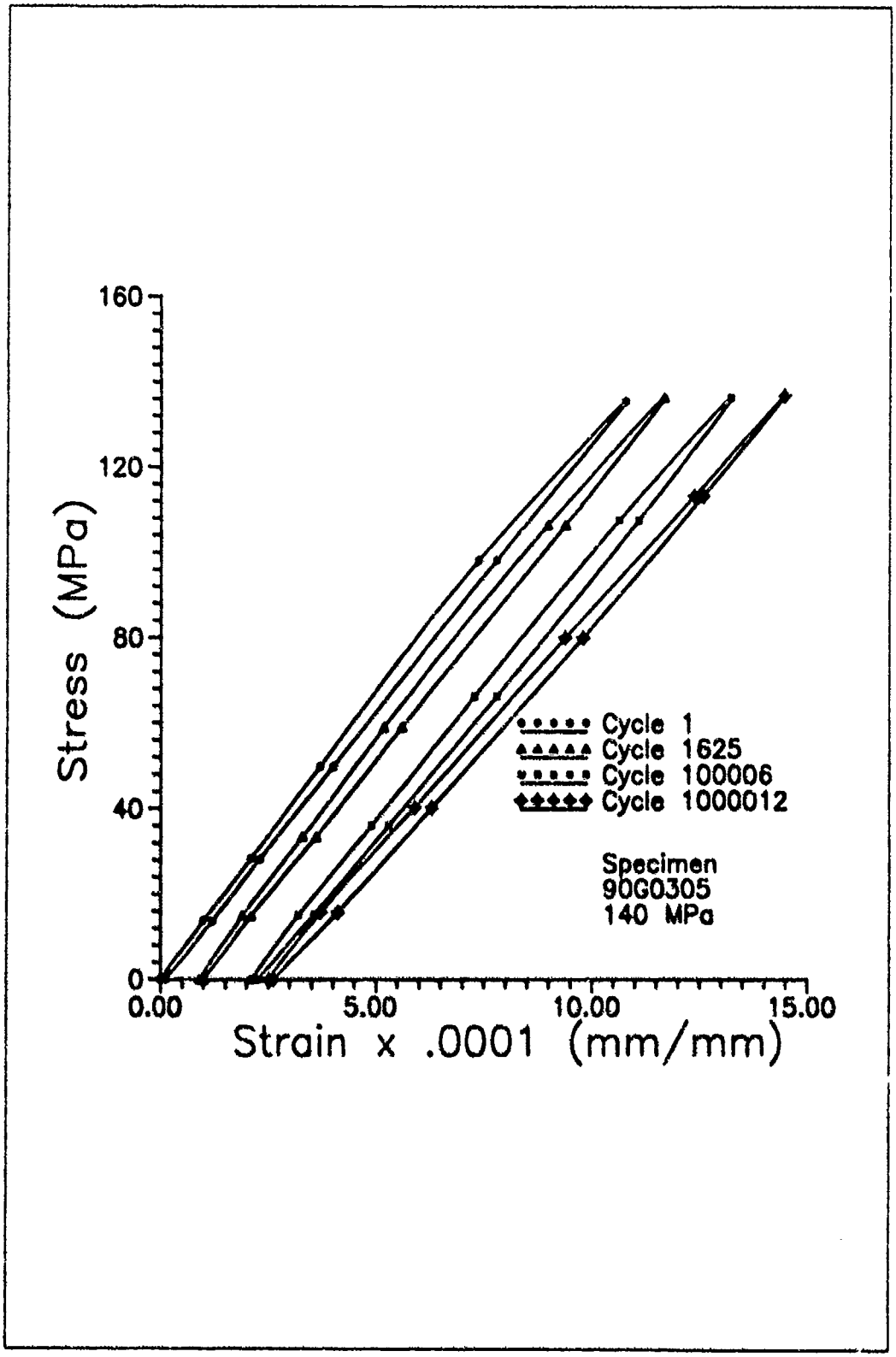

Figure 21 Stress vs. Strain 140 MPa Test

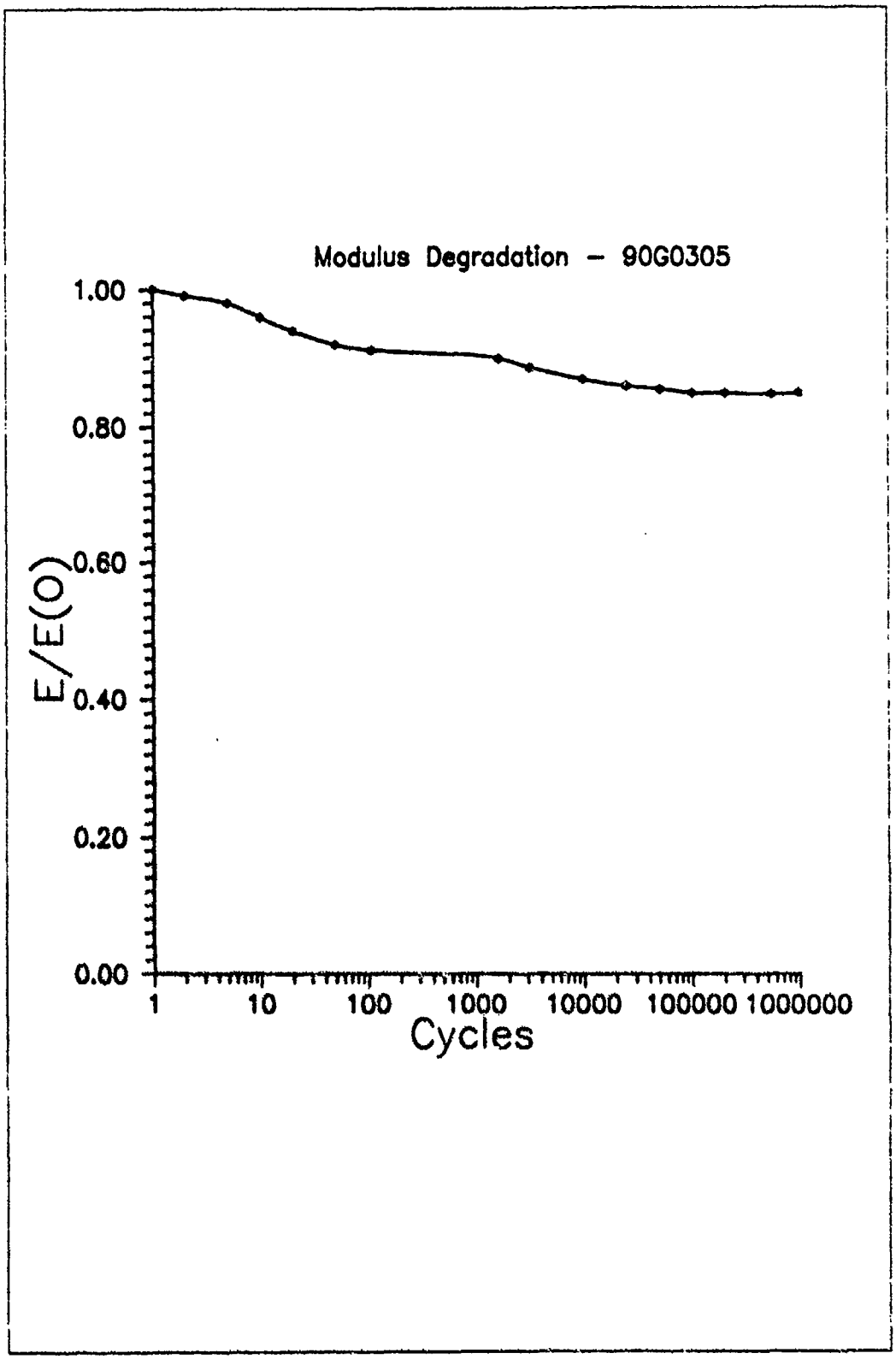

Figure 22 Modulus Reduction 140 MPa Test

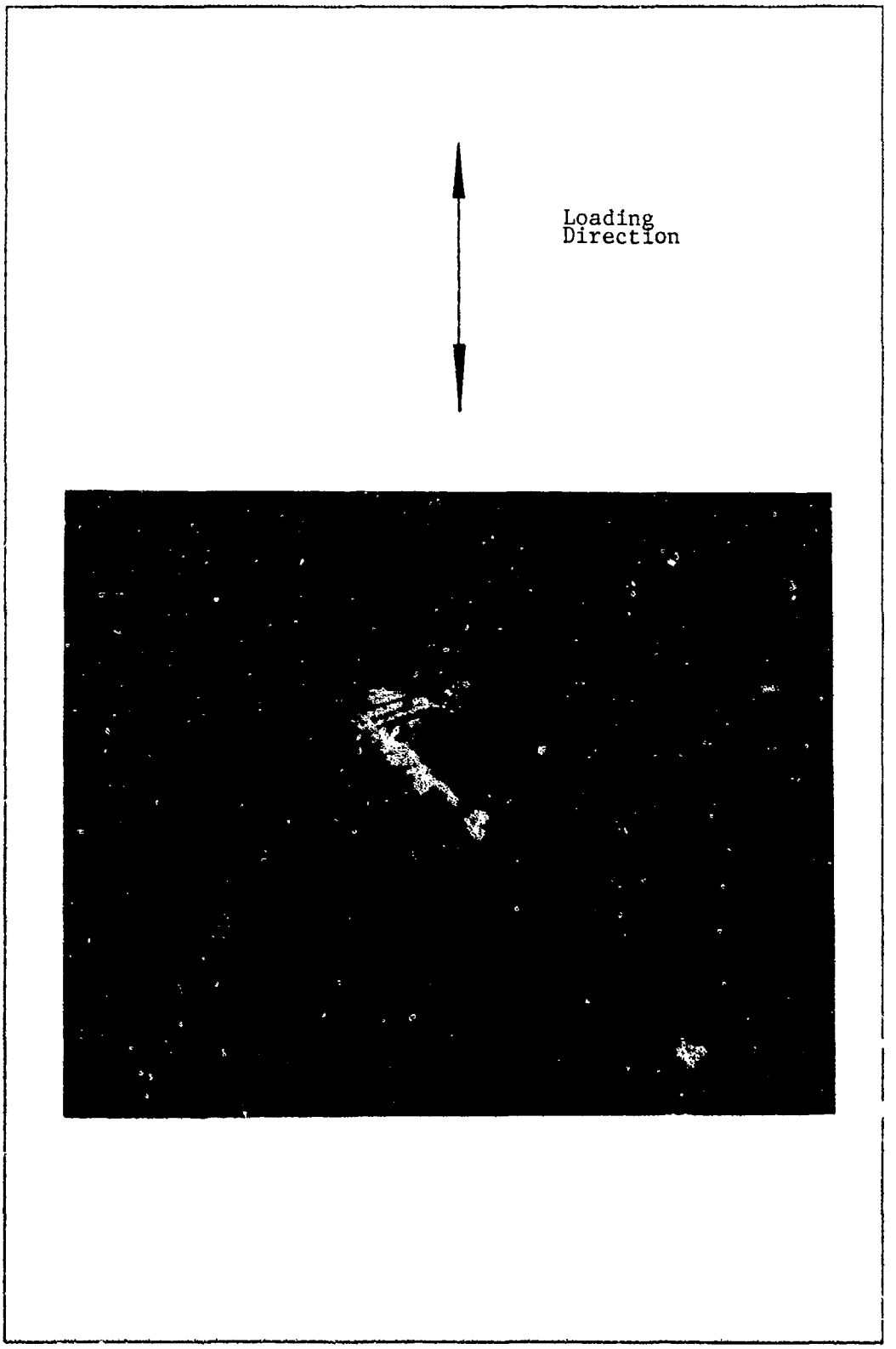

Figure 23 Damage Region 170 MPa Test
25X Magnification, Cycle 4731

The dark area to the right of the hole in figure 23 is not due to fatigue. This area is drilling damage caused during specimen preparation. The ultrasonic drill broke off a portion of the matrix material that coats the surface of the composite.

The crack pattern is very similar to that obtained by Tsangarakis on fatigue tests which he performed on unidirectional SiC reinforced aluminum [38]. The fatigue damage development was also similar to Tsangarakis. The development is shown in figure 24.

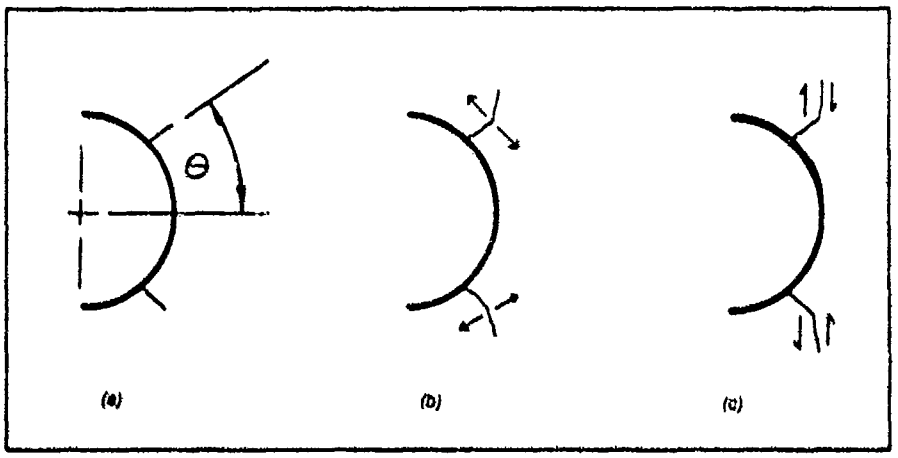

Figure 24 Notched Fatigue Damage Development

The average value of θ for tests in this thesis was 20.85^{0}. Radial cracks extended from the hole near the maximum stress concentration points; fig. 24(a). These cracks then grew longitudinally, opening and closing as a mode I (load is normal to crack plane) crack; fig. 24(b). Tsangarakis stated that continued fatigue turned the cracks into rubbing or Mode II (load is parallel to crack plane) cracks; fig. 24(c).

This was the case with SiC/1723 also. Small radial cracks would appear, turning into longitudinal cracks growing along the length of the specimen. However, examining the specimen under the microscope, it became evident that the fibers exposed by the crack near the hole were still intact. The question arose whether these surface cracks were indicative of damage to the interior of the specimen or just peculiar to the top layer of matrix material. Ultrasonic C-scan provided a clue to this riddle.

Figures 25 and 26 are C-scans of specimen 90G0307. Areas of damage, ie., cracks, show up as dark areas next to the hole. The top scan output of figure 25 is a C-scan of the top surface in the composite. The bottom scan output in the same figure is at a depth near the second and third plies. As can be seen, the damage patterns are similar yet not identical. Scanning deeper into the composite, near the center of the specimen, yields output as shown in figure 26. The damage zone consists of longitudinal dark areas that are consistent with the damage in the plies near the surface. However, they are not identical, indicating that the gating used by the scan is not producing a "shadow" of damage in the middle plies resulting from actual cracks near the surface. Therefore, although, the cracks may grow slightly differently and a differing rate, the mode is the same.

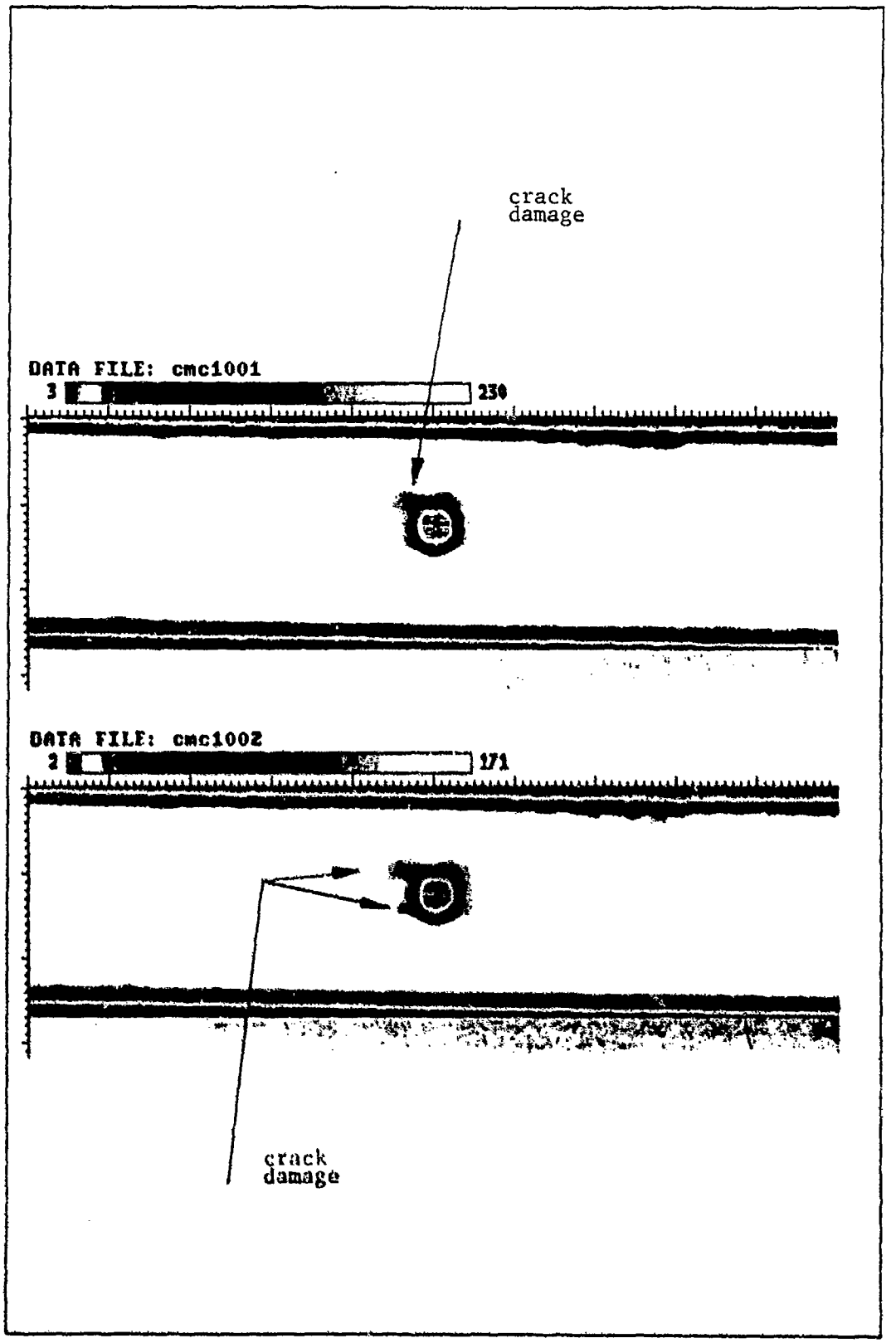

Figure 25 C-Scan, Top Plies, 90G0307

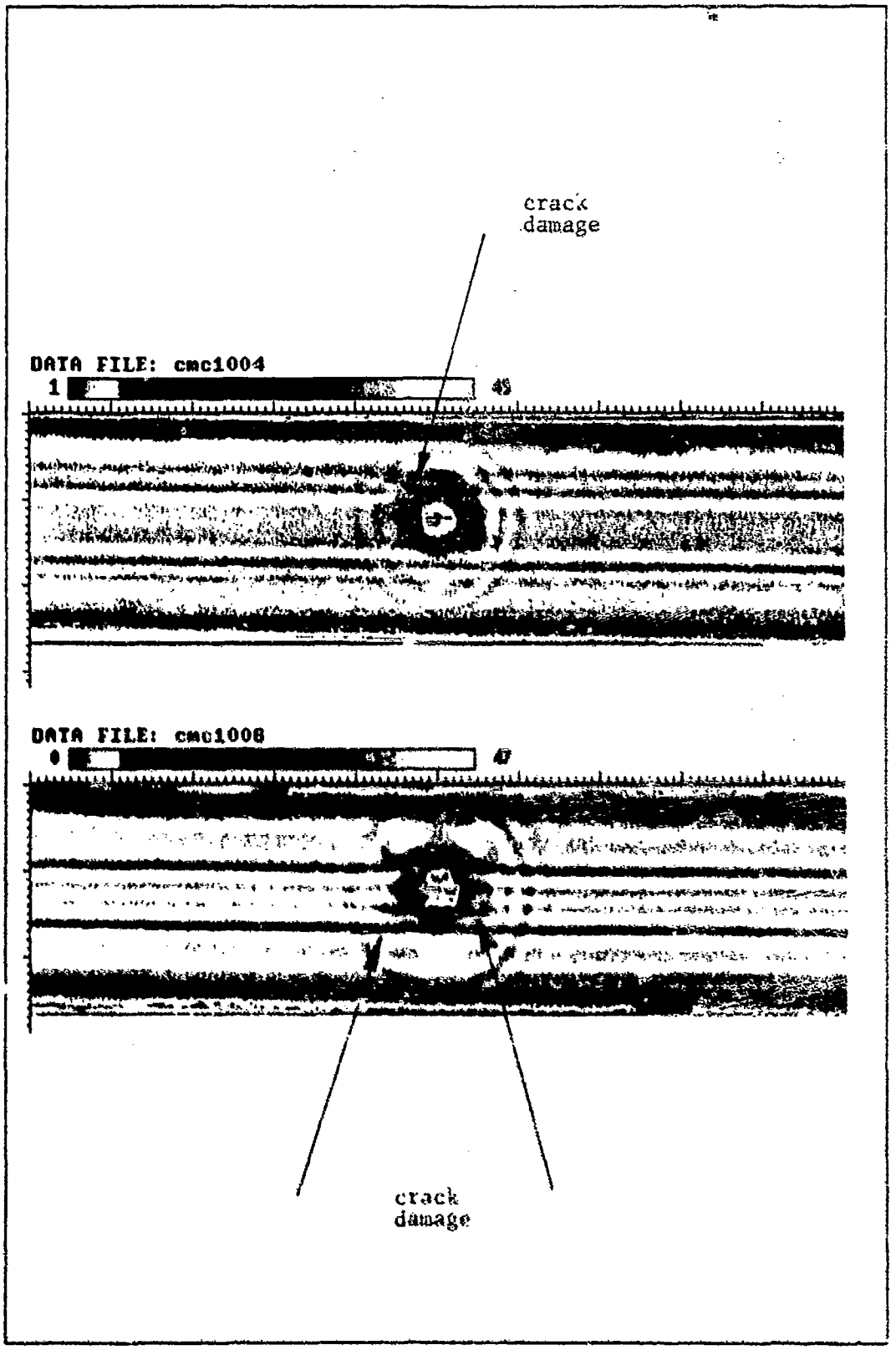

Figure 26 C-Scan, Middle Plies, 90G0307

The matrix cracks throughout the laminate must be growing longitudinally and eventually coalesce into the large fracture cracks that were evident in the static tensile tests. Based on these facts, the surface replicas were considered a good indication of damage in the composite.

The cracks shown in figure 23 had fully developed by five thousand cycles. Replicas taken at one million cycles showed no further crack growth. Figure 27 depicts the modulus degradation for the 170 MPa test. The specimen ran-out with a decrease in stiffness of twelve percent.

The next test levels were chosen in order to obtain a reasonable chance of failure. Specimen 90G0308 had a maximum stress of 250 MPa. Based on where this specimen failed, other tests would be run to fill in the S-N curve. The results of this test are shown in figures 28, 29 and 30. The stress-strain curves in figure 28 clearly show a much higher residual strain effect than prior tests. There is clear change in the slopes of the curves indicating a change in stiffness.

Figure 28 also shows the first indication of a phenomenon observed by Prewo [33]. He found that when the minimum stress in the test was low enough, the material would appear to gain most of its stiffness back. The slope of the stress-strain curve would approach that of the initial cycle. He attributed this to the closure of the matrix cracks.

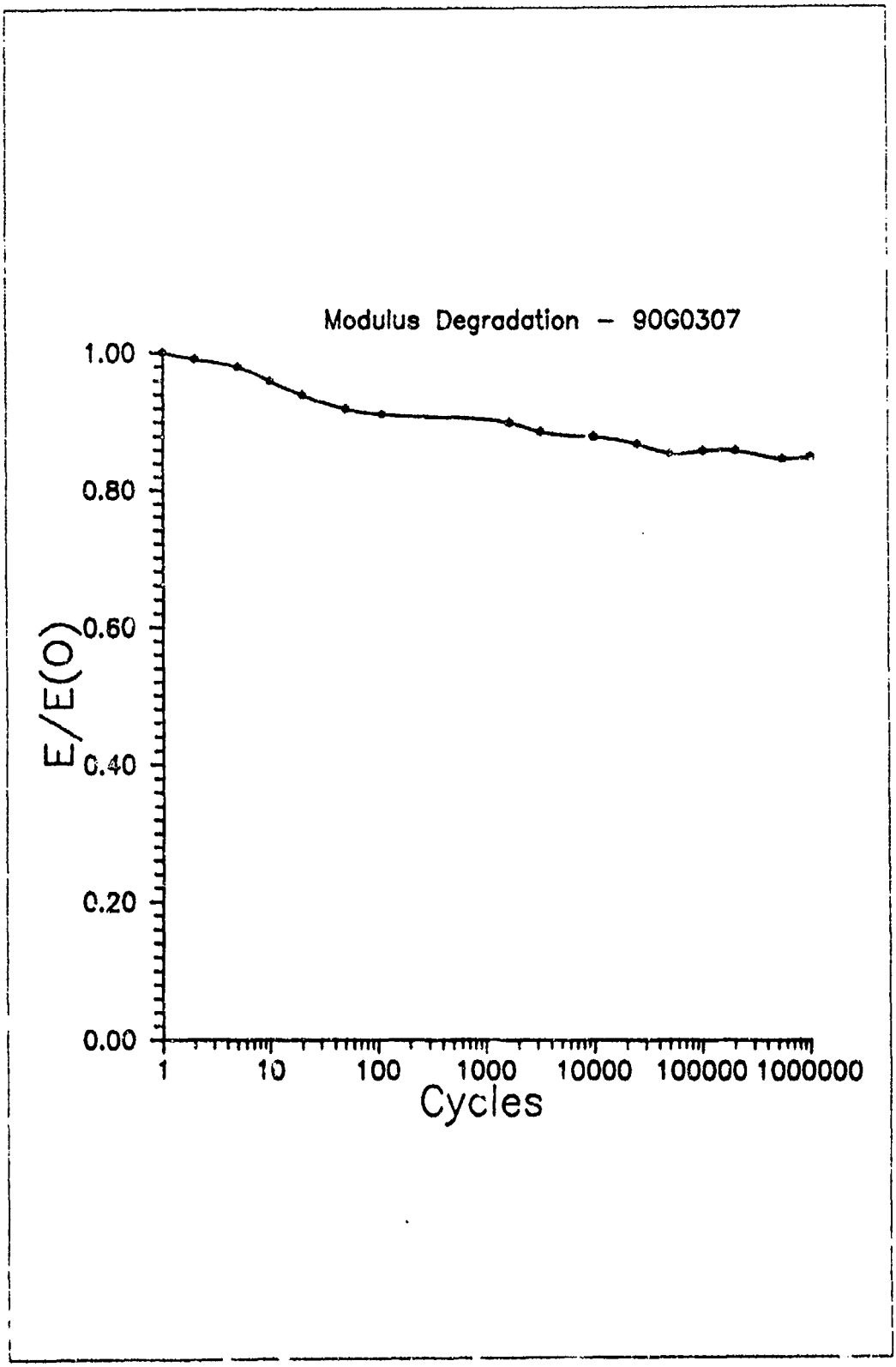

Figure 27 Modulus Reduction 170 MPa Test

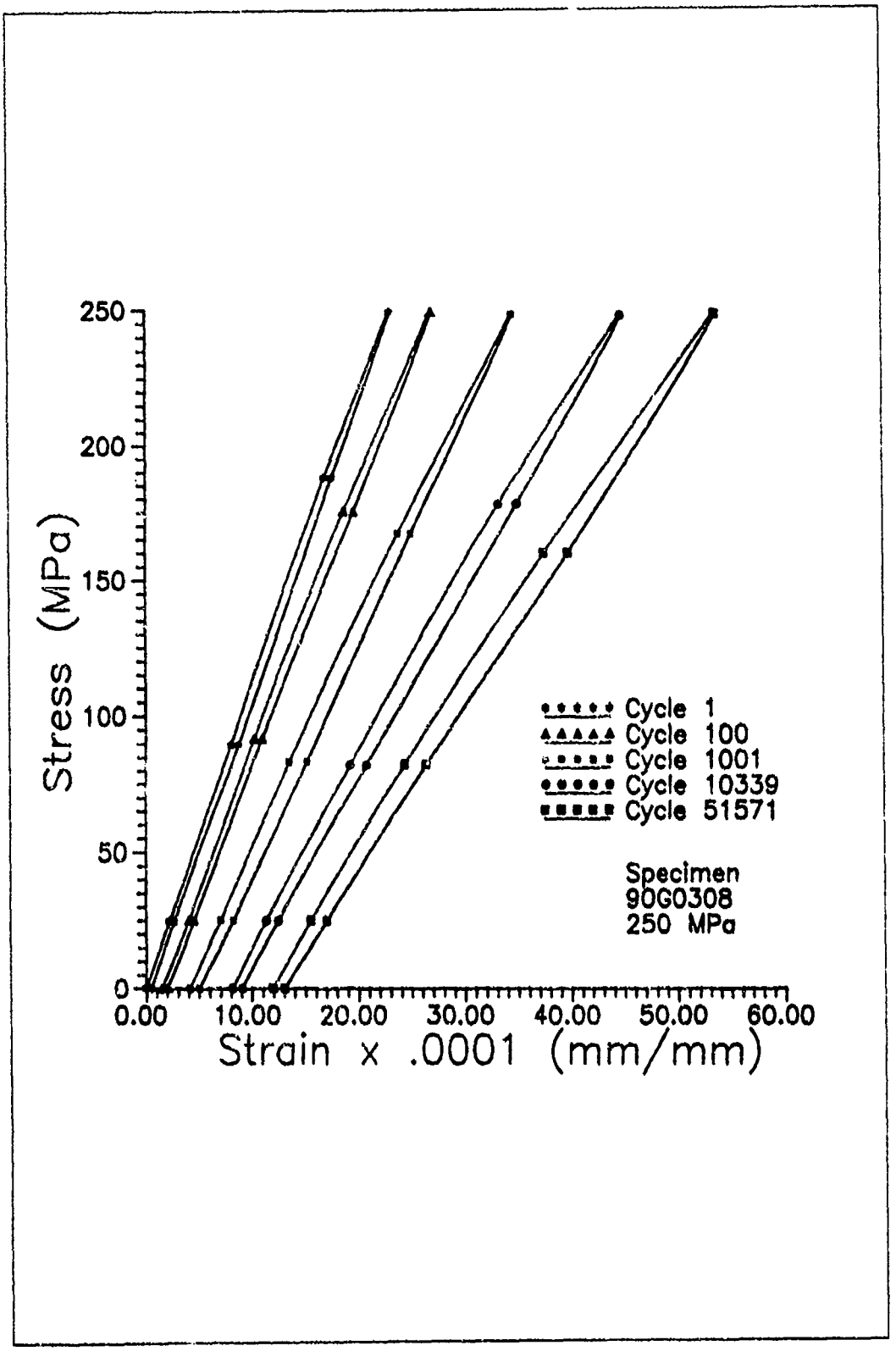

Figure 28 Stress vs. Strain 250 MPa Test

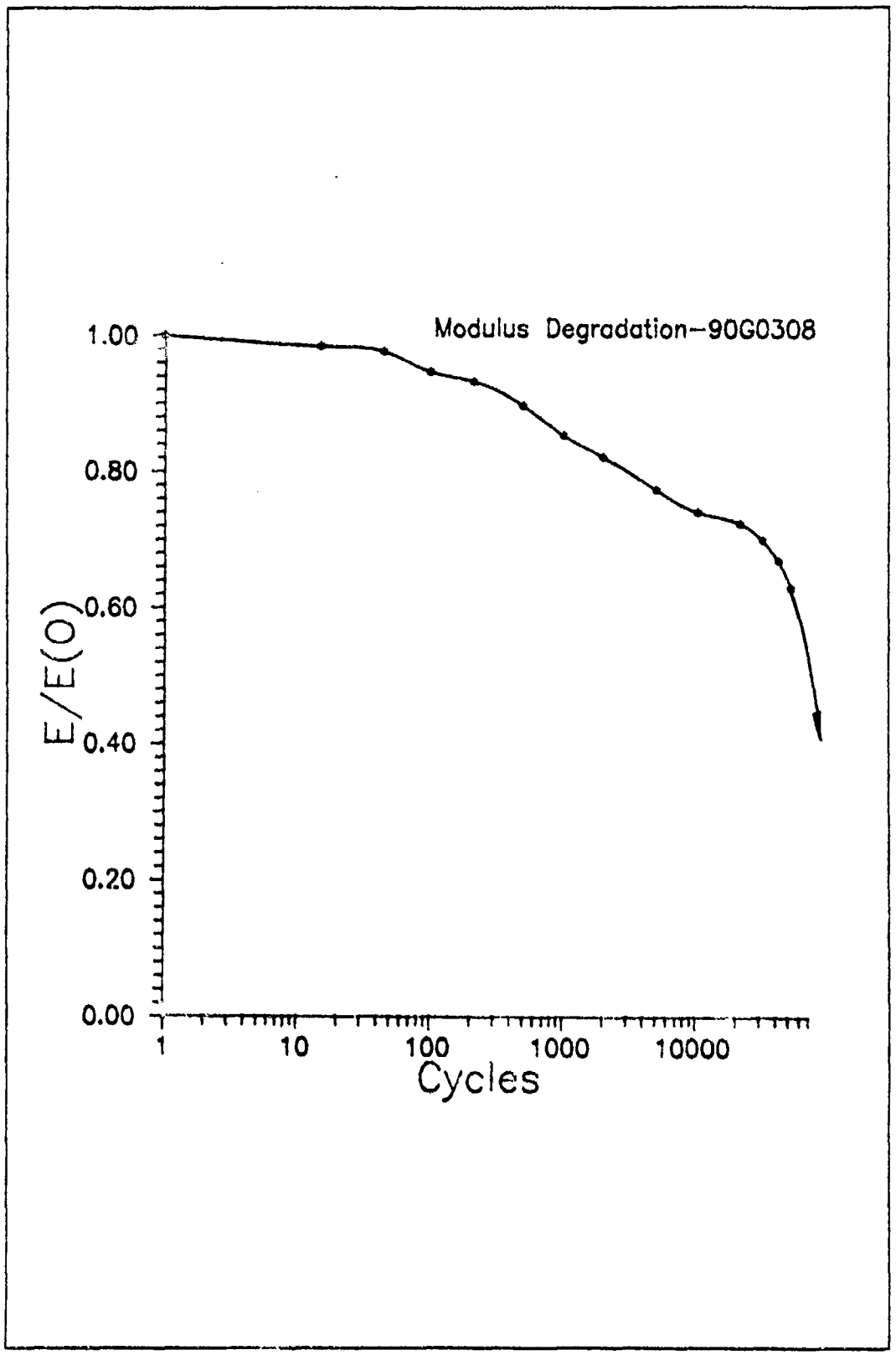

Figure 29 Modulus Reduction 250 MPa Test

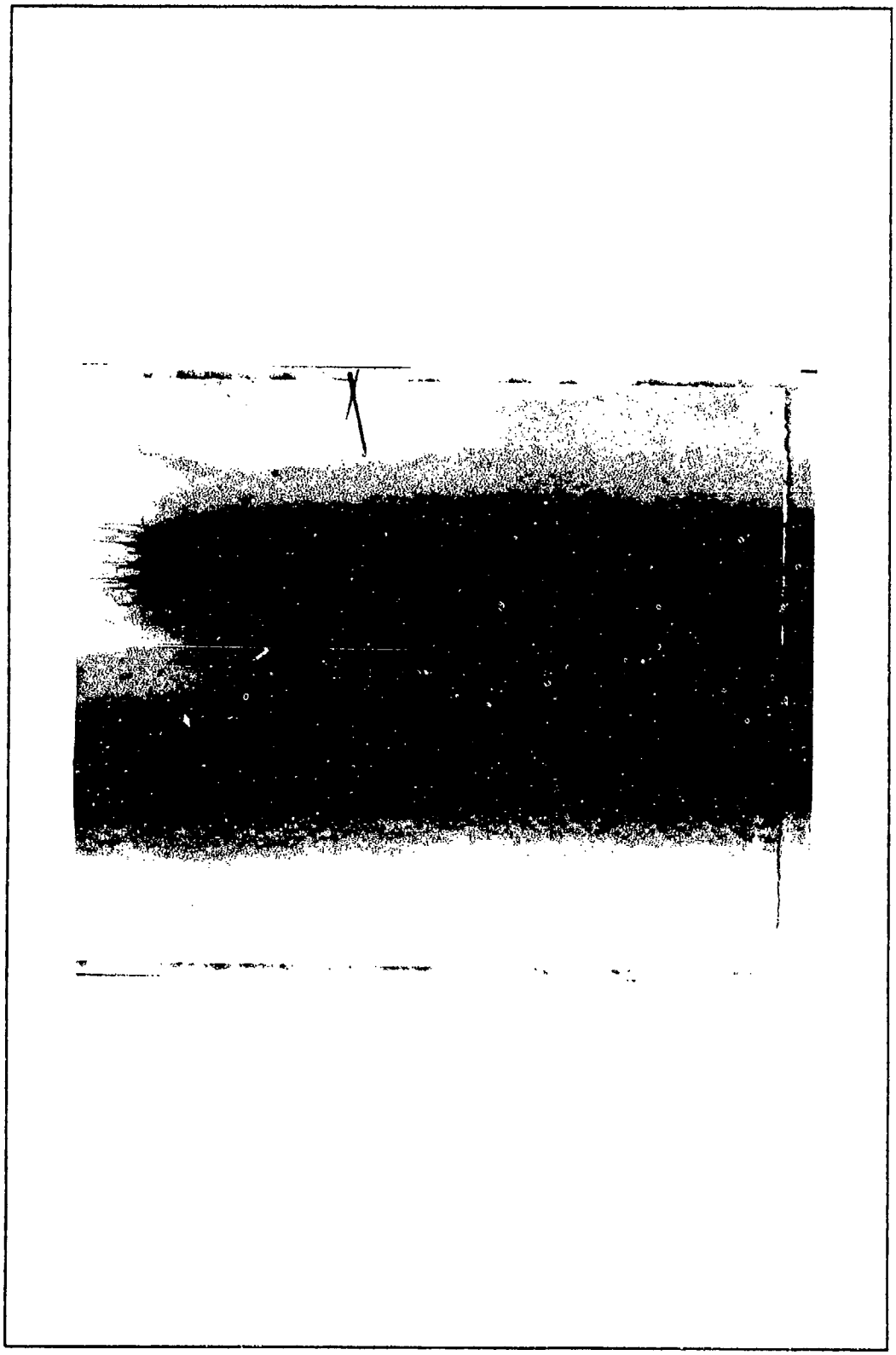

Figure 30 Final Fracture, Specimen 90G0308, 6.3X Mag.

As the stress was raised, the cracks would open allowing the material to extend more than an undamaged specimen. When the cracks opened, the modulus would then decrease. This phenomenon appears in figure 28. For cycles 100, 1001, 10339 and 51571, the slopes are nearly equal to cycle one at a stress less than approximately 80 MPa. Above that stress, the modulus would decrease; a greater amount for each subsequent cycle. This theory makes sense since CMCs are a brittle material with little plastic deformation. The material would attempt to regain its original configuration after the load was reduced. The fact that the slopes of the stress-strain curves at low stress do not totally recover to the initial cycle slope indicates some permanent damage has occurred. This is verified by the accumulated residual strain. If the material regained its original state, the residual strain would be zero.

Figure 29 presents the modulus degradation for the 250 MPa test. The modulus shows steady decrease until 50000 cycles where the specimen begins a sudden decrease in stiffness until failure at 53803 cycles.

Cracks propagated longitudinally from the maximum stress concentration points. Final fracture, which occurred in these damage zones is shown in figure 30.

Plate 90G03XX had been consumed when specimen 90G0308 was processed. Testing continued with specimens from plate 90G07XX. A static tensile test was performed to ensure

the notched failure stress was the same as those obtained in the first plate. The proportional limit was 152 MPa and the failure stress was 348 MPa. This stress was somewhat higher than the 300 MPa failure stress from the 90G03XX plate. Because of this fact, the final S-N curve for this lay-up would be non-dimensionalized relative to each plate's static tensile failure stress. Using this non-dimensional stress approach, specimen 90G0308 failed at eighty-three percent of its static ultimate stress at 53803 cycles.

Testing continued with specimens having maximum stresses greater than eighty-three percent of ultimate to fill in the S-N curve. Specimen 90G0701 was tested at 313.8 MPa maximum stress. This level represented ninety percent of ultimate stress. Results of this test are shown in figures 31 and 32. The stress-strain curves show large residual strain accumulation after only five cycles. Unfortunately, the data in this test was acquired logarithmically. The next cycle where data would have been taken was cycle ten. However, the specimen broke at cycle ten and the software will not record data on a cycle unless the cycle is completed. Therefore, at cycles eight and nine where severe decrease in modulus would occur, data was not taken. This is shown better in figure 32, modulus degradation for specimen 90G0701. At cycle five, there is an eight percent decrease in modulus, dropping off quickly towards zero by cycle ten. It can be concluded from this figure that severe crack growth occurred in cycles six

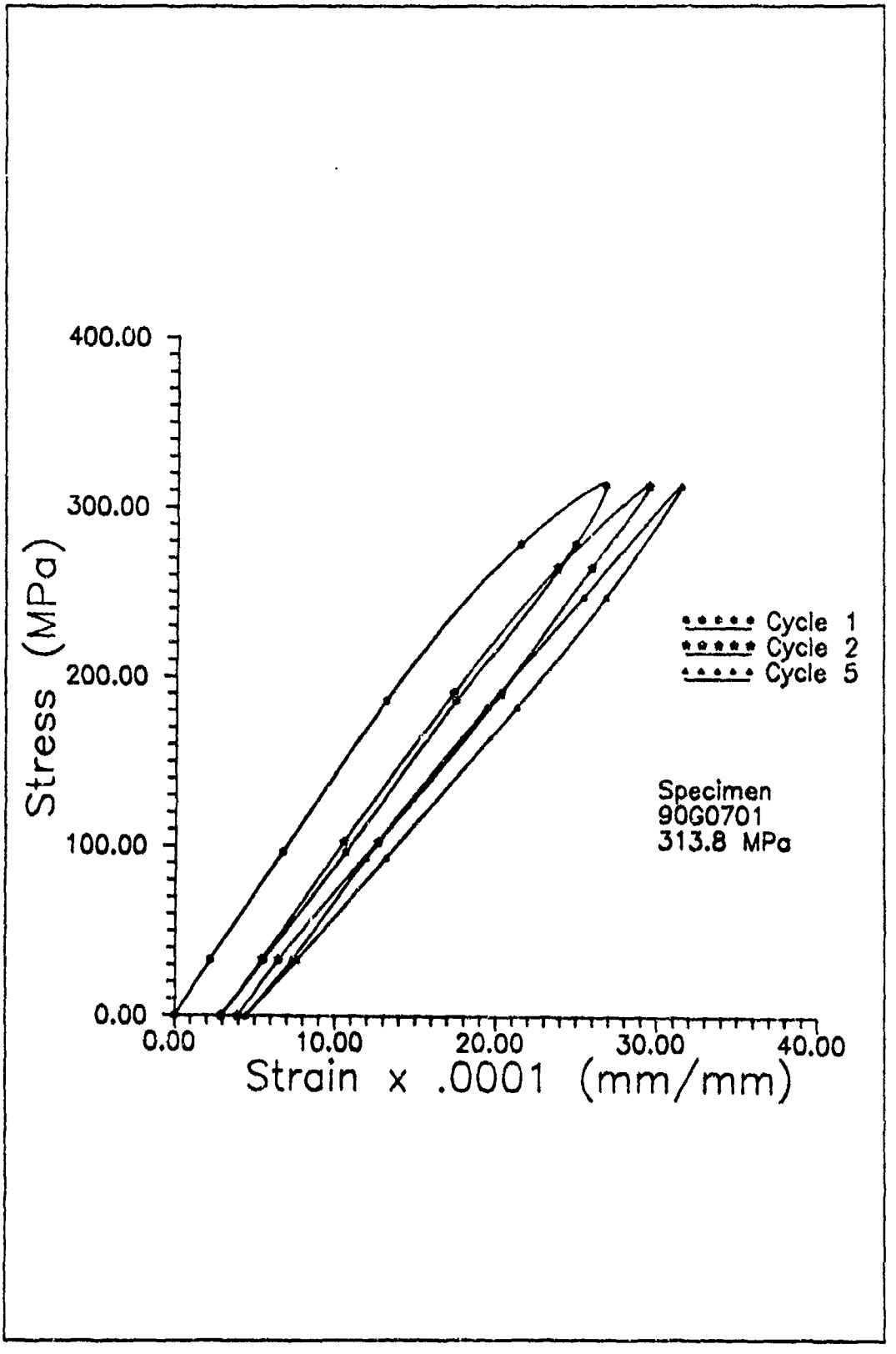

Figure 31 Stress vs. Strain 313.8 MPa Test

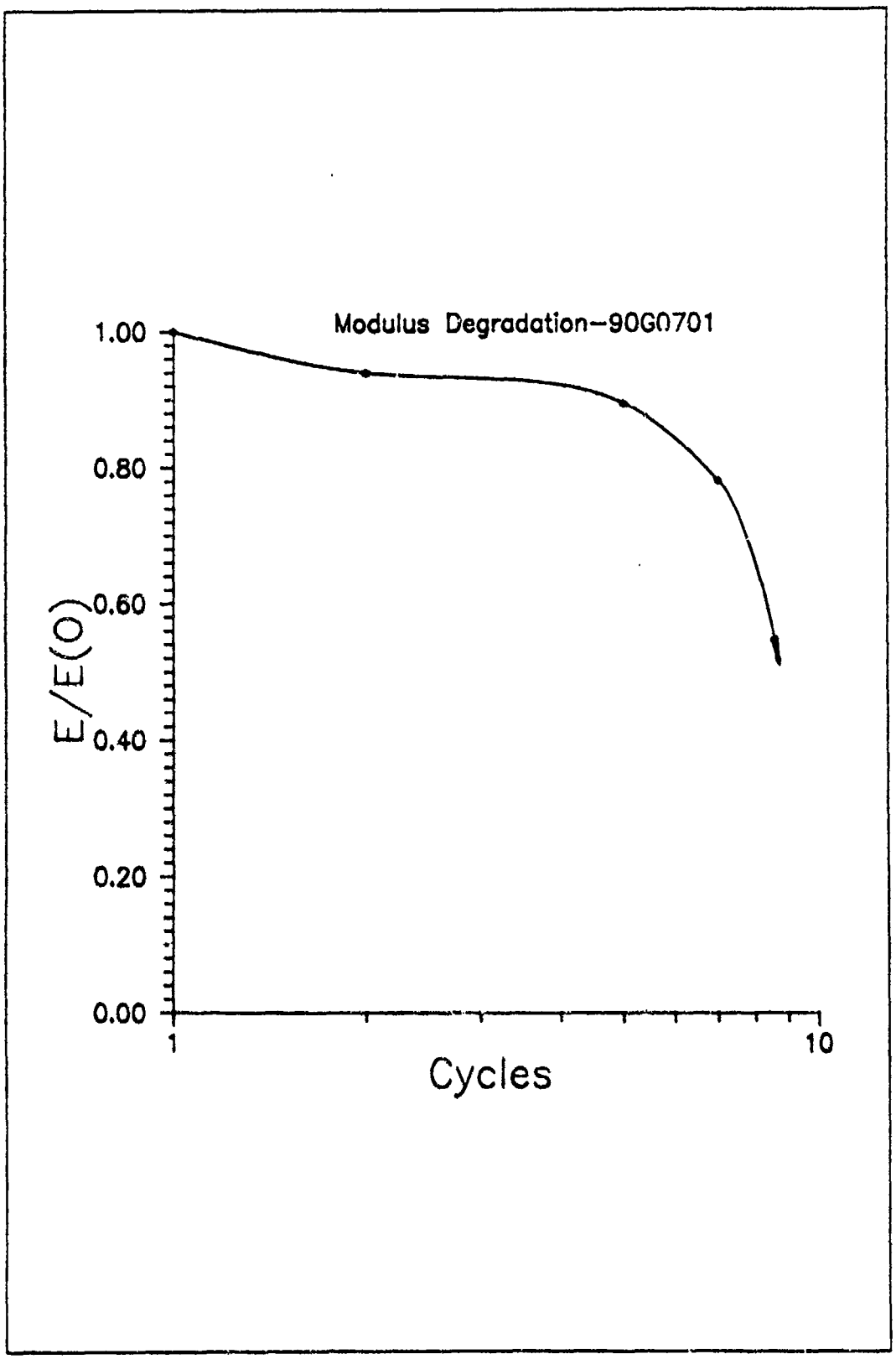

Figure 32 Modulus Reduction 313.8 MPa Test

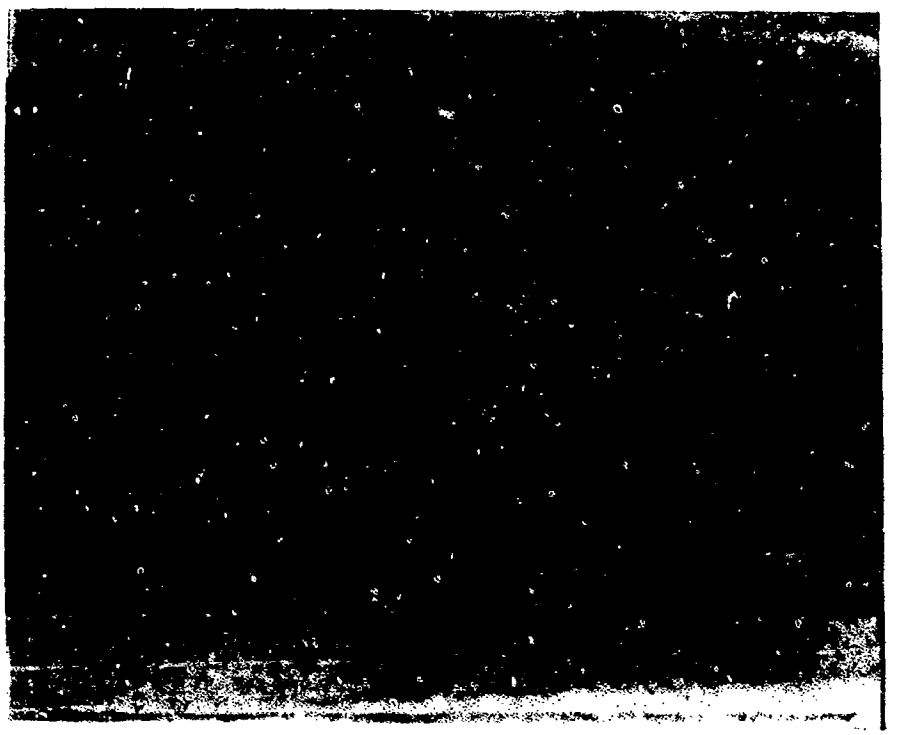

Figure 33 Final Fracture, Specimen 90G0701, 6.3X

to nine. The final fracture appearance is shown in figure 33, which clearly indicates failure occurred due to unstable growth of the longitudinal cracks emanating from the sides of the hole.

SEM photographs of this specimen were taken to verify the C-Scan results of the earlier test. The author wanted to examine the crack in Specimen 90G0701 where failure did not occur. This would be the lower crack extending to the left in figure 33. This crack appears as a surface matrix crack. It was necessary to microscopically show that the crack extended through the thickness and was not confined to the top matrix layer. The cracks on opposite sides of the specimen were not identical so it could not be assumed that the crack was through the thickness. Figure 34 is an SEM photograph taken looking down into the hole. In the left portion of the figure, the surface longitudinal matrix crack is visible, with intact fibers below it. However, as can be seen, the matrix crack extends through the hole as predicted earlier. The specimen was then cut in half several millimeters below the hole. Figure 35 is an SEM photograph of one of the cut surfaces. It is obvious in the figure that the matrix crack has extended totally through the thickness. The somewhat random path of the crack accounts for the different crack appearances on opposite sides of the specimen.

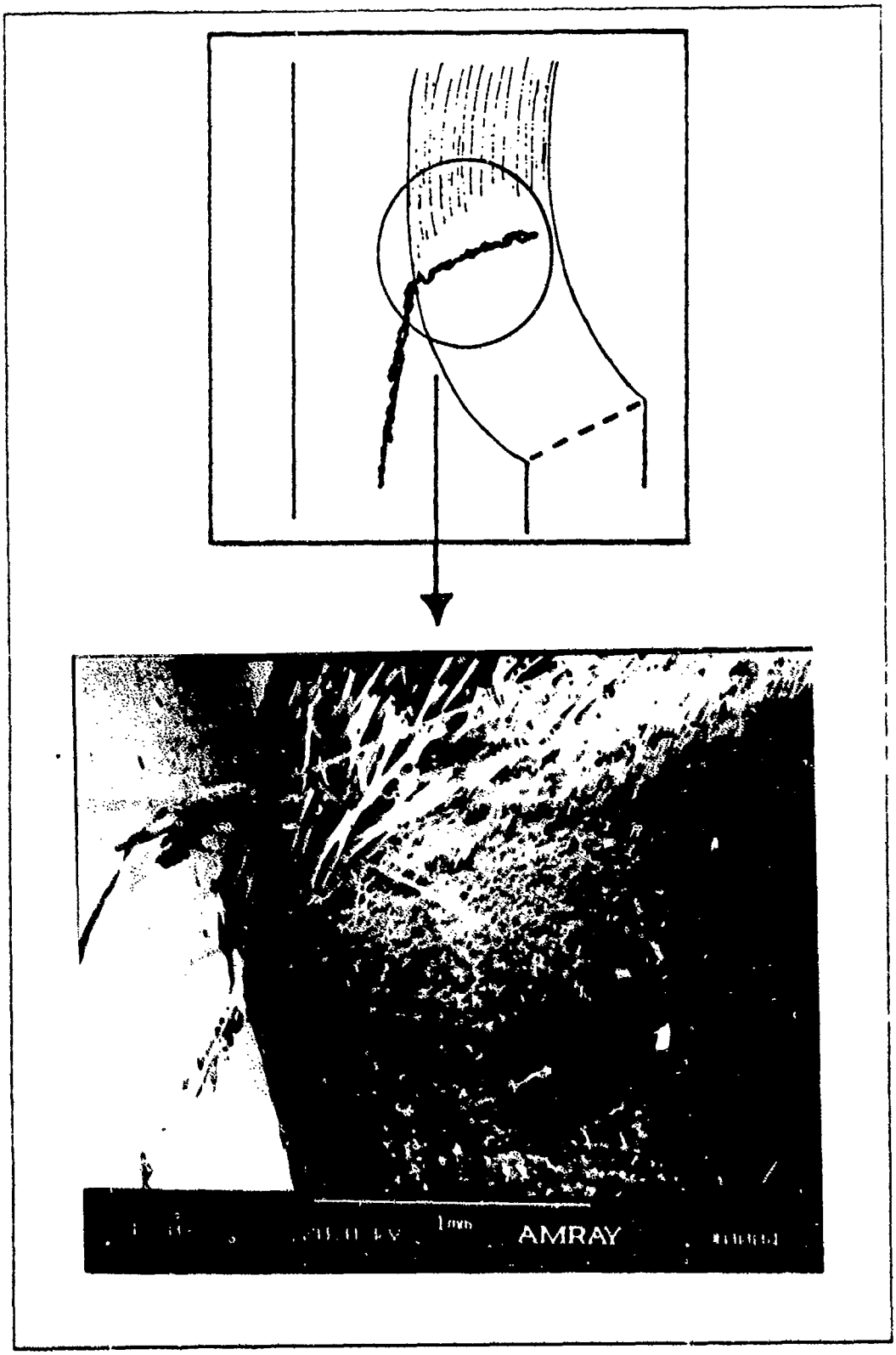

Figure 34 SEM Photograph, Specimen 90G0701

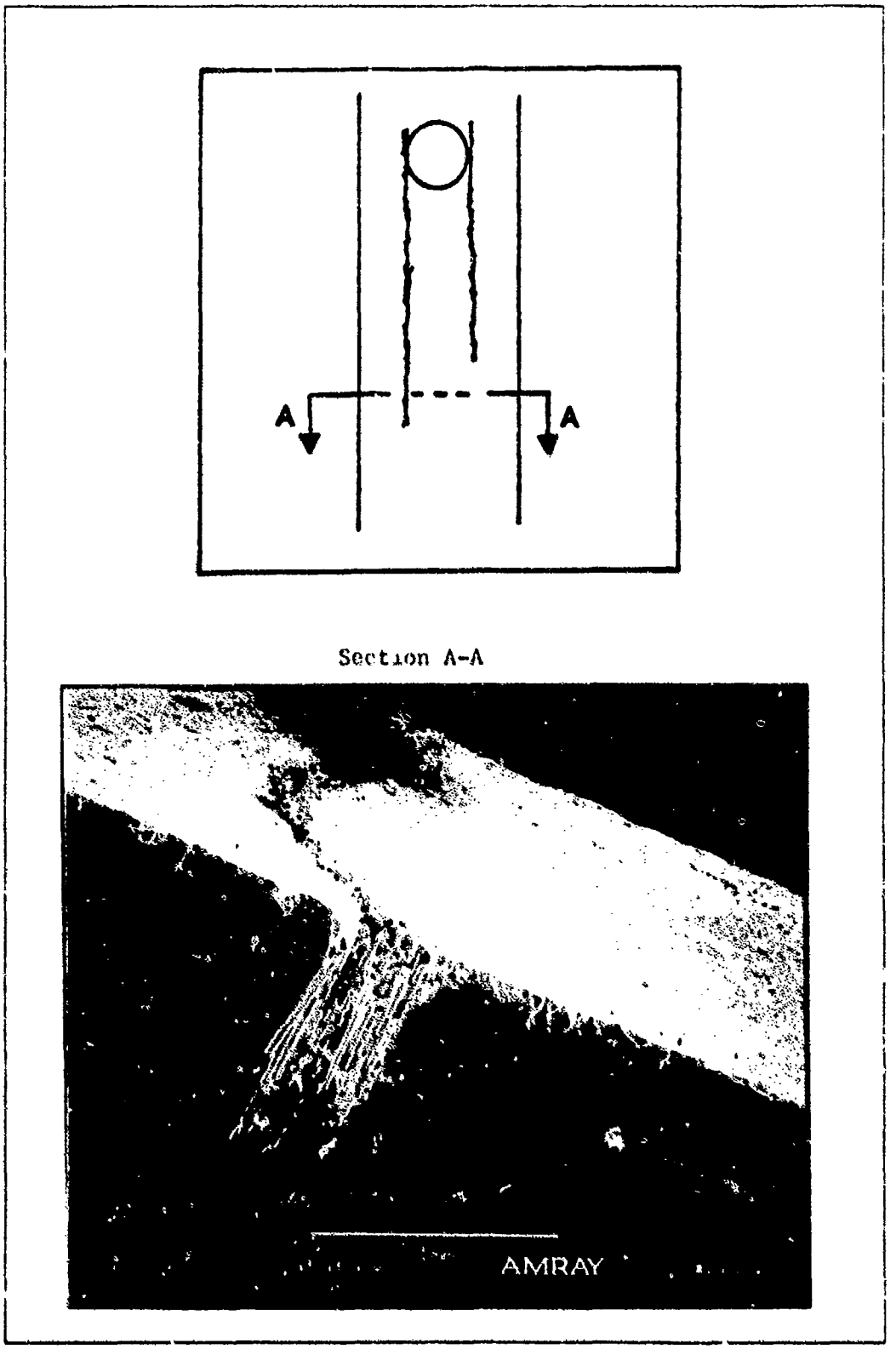

Figure 35 SEM Photograph, Specimen 90G0701

Failure stresses had now been obtained for ninety and eighty-three percent of ultimate static tensile strength. Cycles to failure were ten and 53803. Since there were three orders of magnitude between these cycles, two more points were chosen to fill in this gap.

Specimen 90G0703 was fatigue tested at 298 MPa. This represented eighty-six percent of ultimate strength. Results of this test are given in figures 36, 37, 38, and 39. The stress-strain curves of figure 36 show a great deal of residual strain accumulation. Plate 90G07XX seemed to have more strength and stiffness than plate 90G03XX. Failure strains were also larger. However, trends that appeared in the first plate also show up in 90G0703. Notice in figure 36 that at stresses below approximately 70-100 MPa the slope of the stress-strain curves approach cycle one. This is consistent with the crack closing theory discussed earlier. Above the "matrix crack closing" stress, each subsequent cycle shows a further decrease in slope consistent with accumulating damage.

The longitudinal modulus degradation is shown in figure 37. There is stable decrease in modulus until ten thousand cycles at which point crack growth begins to grow substantially resulting in a large decrease in modulus. This specimen failed at 17001 cycles.

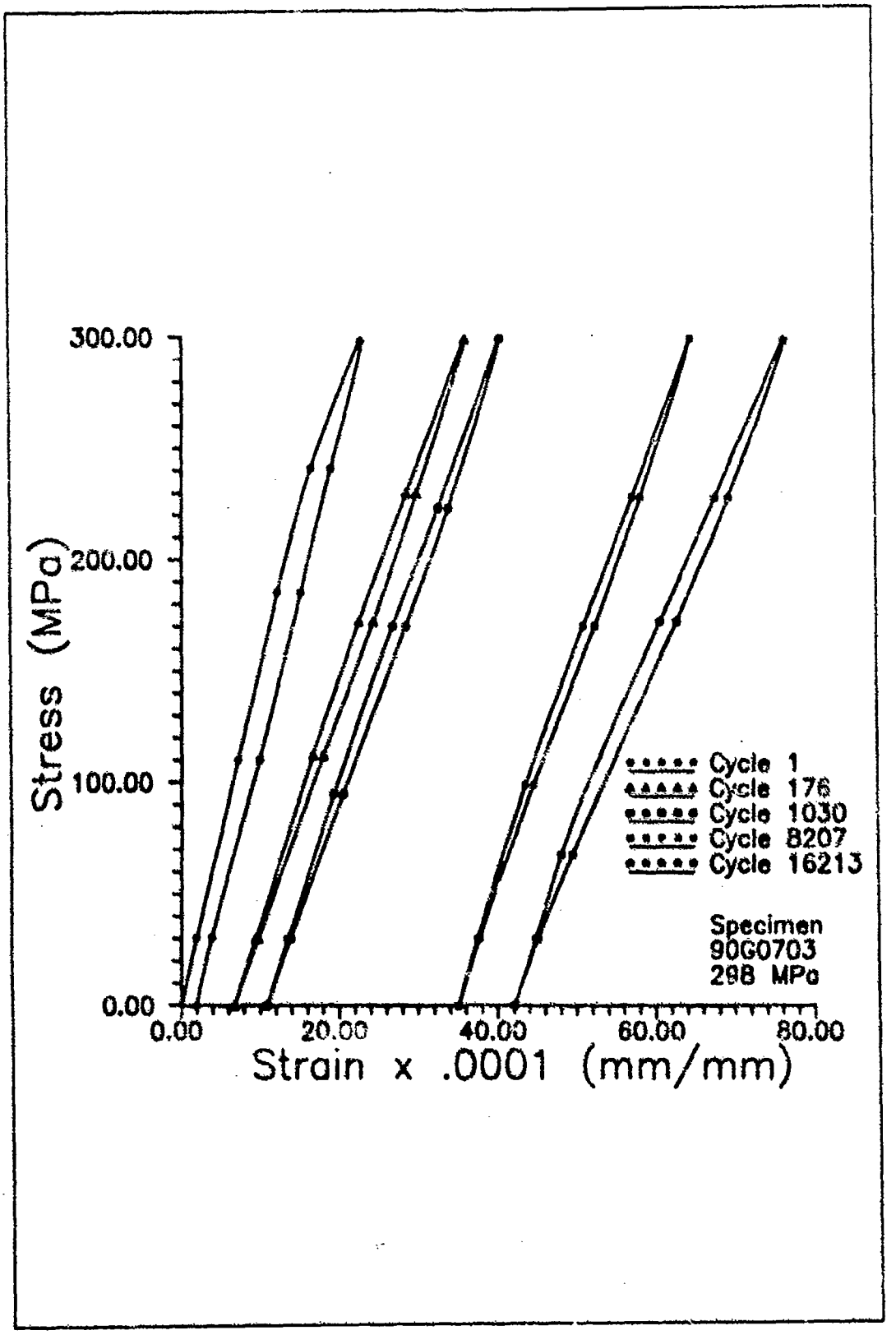

Figure 36 Stress vs. Strain 298 MPa Test

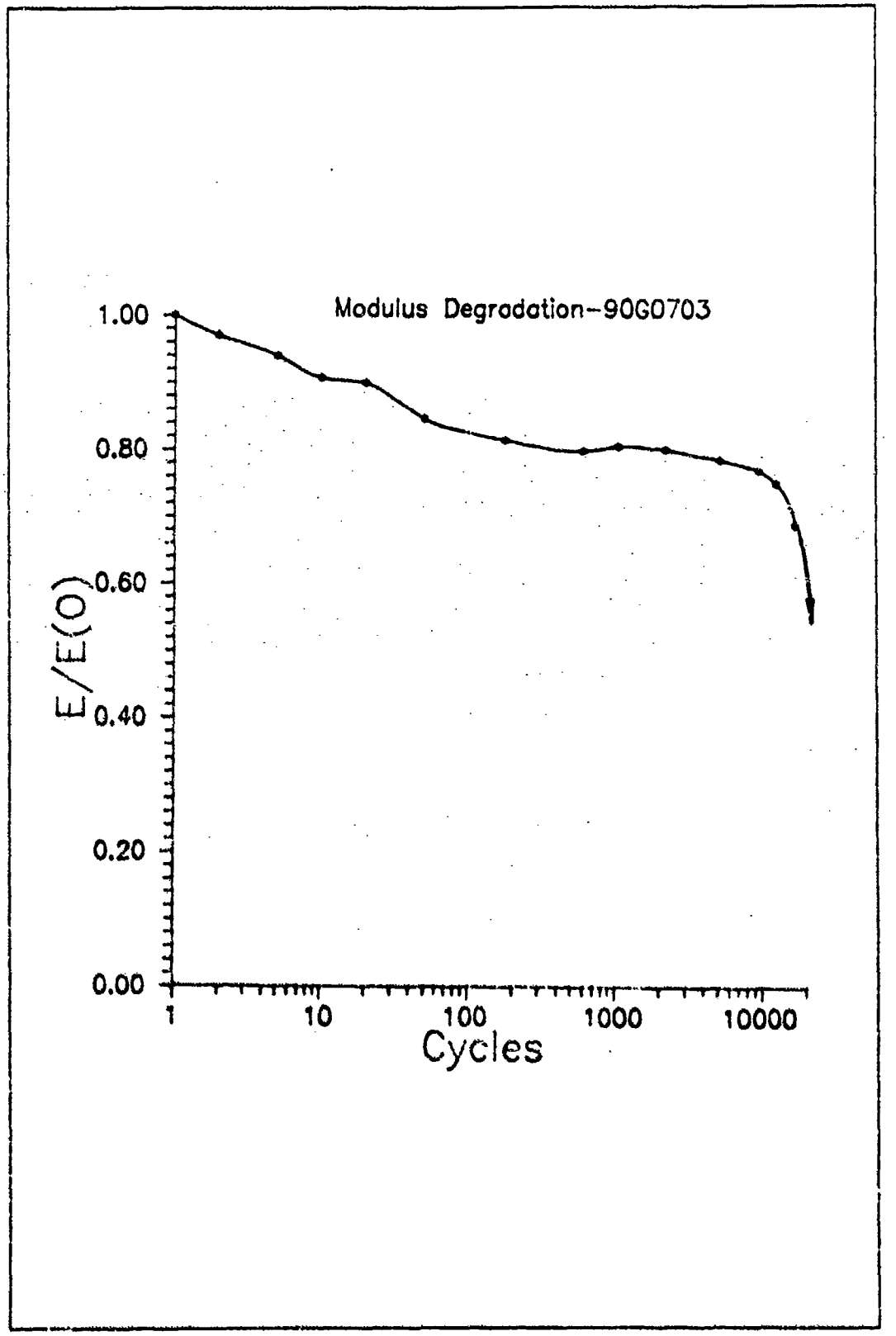

Figure 37 Modulus Reduction 208 MPa Test

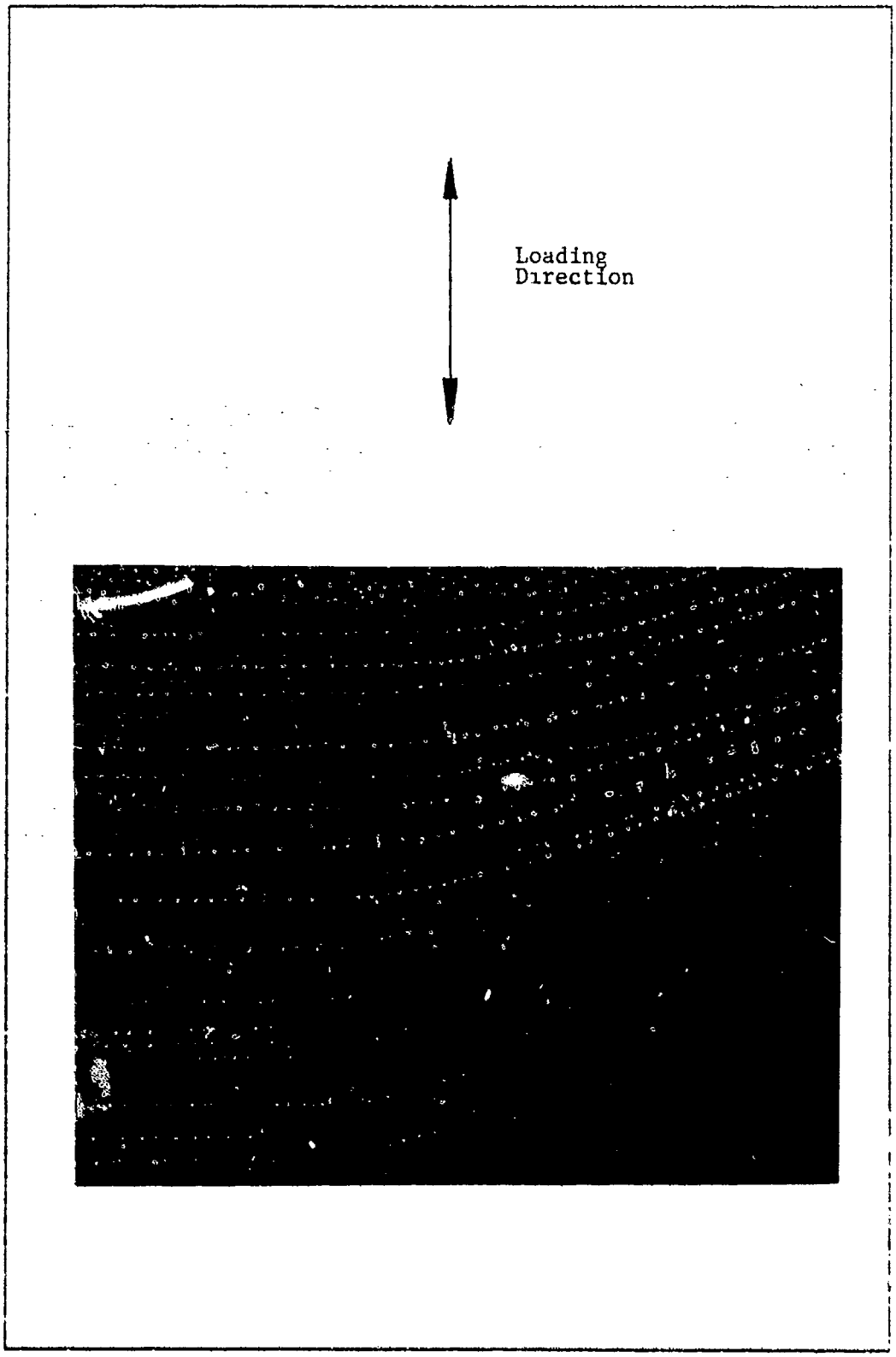

Figure 38 Damage Region, 298 MPa Test
25X Mag, Cycle 1027

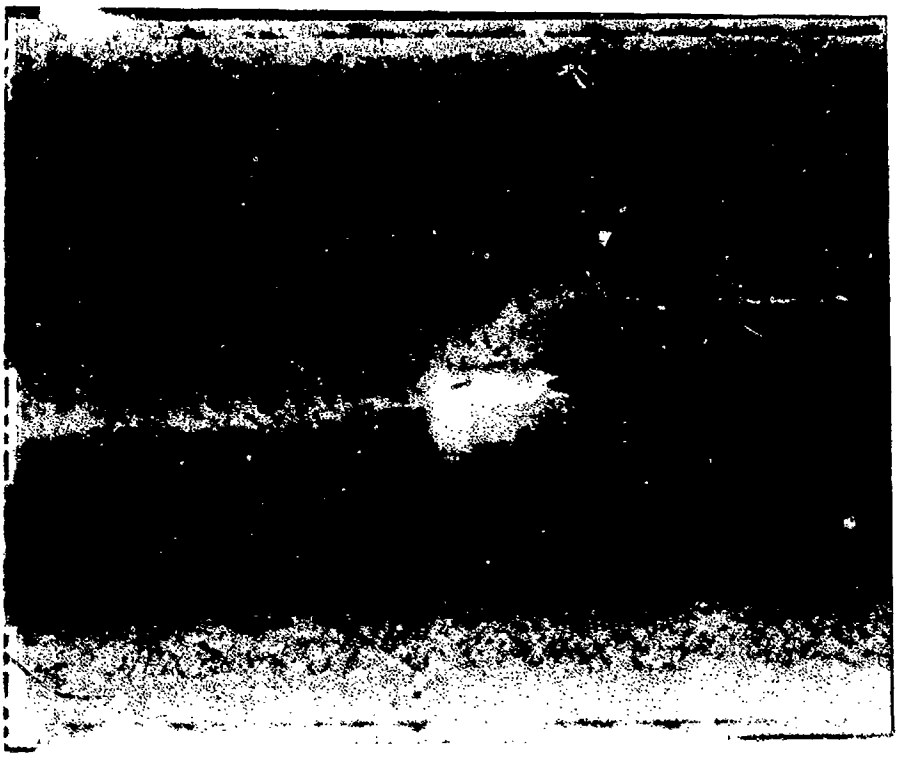

Figure 39 Final Fracture Specimen 90G0703

Figure 38 presents a replica photograph of 90G0703 after 1027 cycles. The longitudinal cracks are already well formed and extended a substantial distance from the hole. For the specimens that failed in the unidirectional tests, surface cracks appeared early. Cracks grew between plies eventually extending as the large fracture cracks seen in figure 39.

The second specimen chosen to fill in the failure points on the S-N curve was 90G0704. This specimen was tested at 310 MPa, eighty-nine percent of ultimate. The specimen failed after 1105 cycles of testing. Modulus degradation is shown in figure 40. This specimen showed a steeper decrease earlier than 90G0703 which is to be expected since the stress is higher and more damage is occurring. Unstable degradation begins at 600 cycles, culminating in failure at 1105 cycles. The fractured specimen is shown in figure 41. The pattern is consistent with all other fractures discussed thus far.

Four failure points had been obtained at this point. Failure stresses ranged from ultimate tensile to eighty-three percent of ultimate. However, the highest stressed test with run-out was only fifty-six percent of ultimate. This was the 170 MPa test, specimen 90G0307. The strategy was to now test a specimen in between the lowest failure stress and highest stress at run-out. This would fill in th S-N curve and determine if notched SiC/1723 had a clearly defined endurance limit.

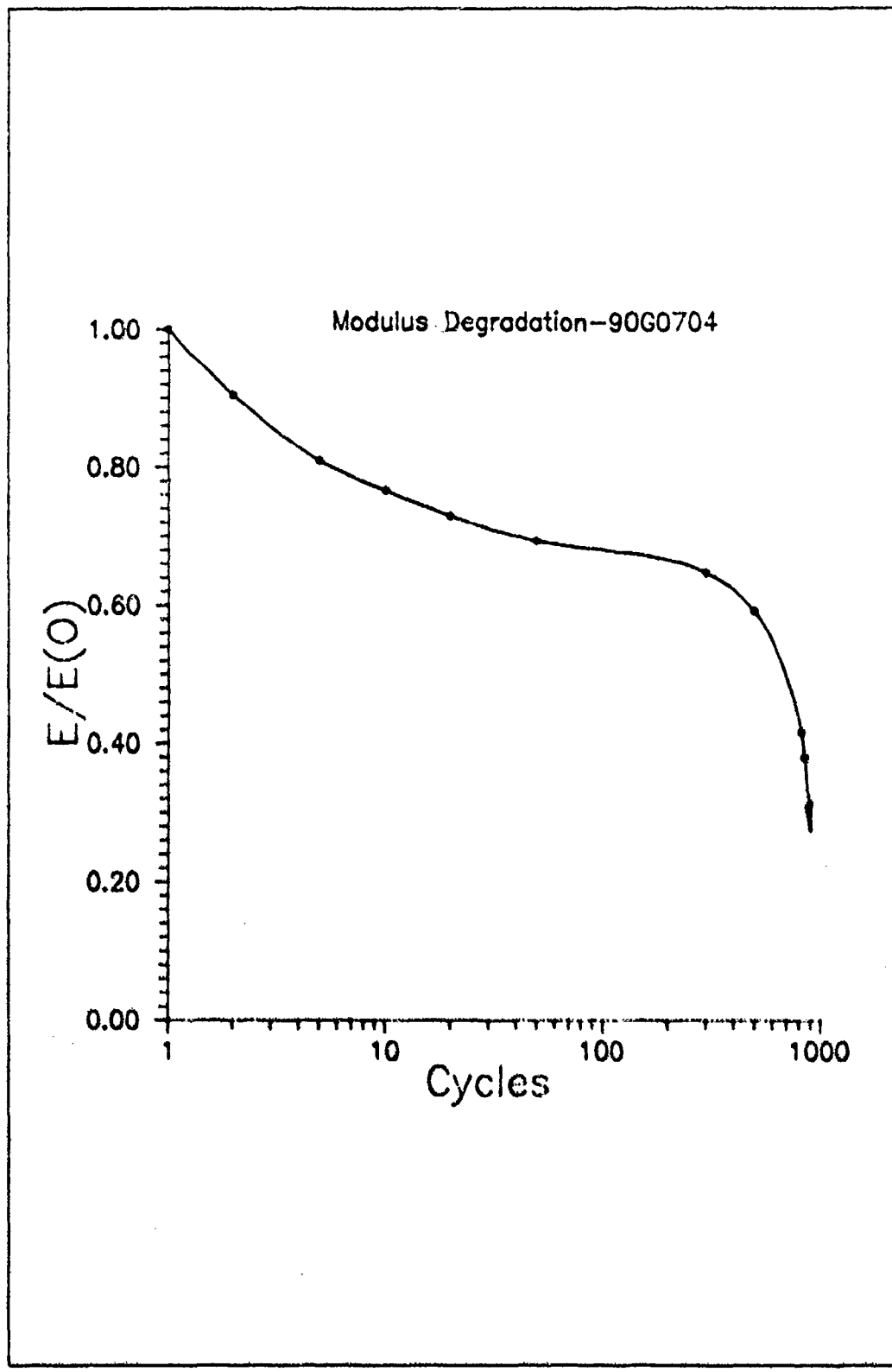

Figure 40 Modulus Reduction 310 MPa Test

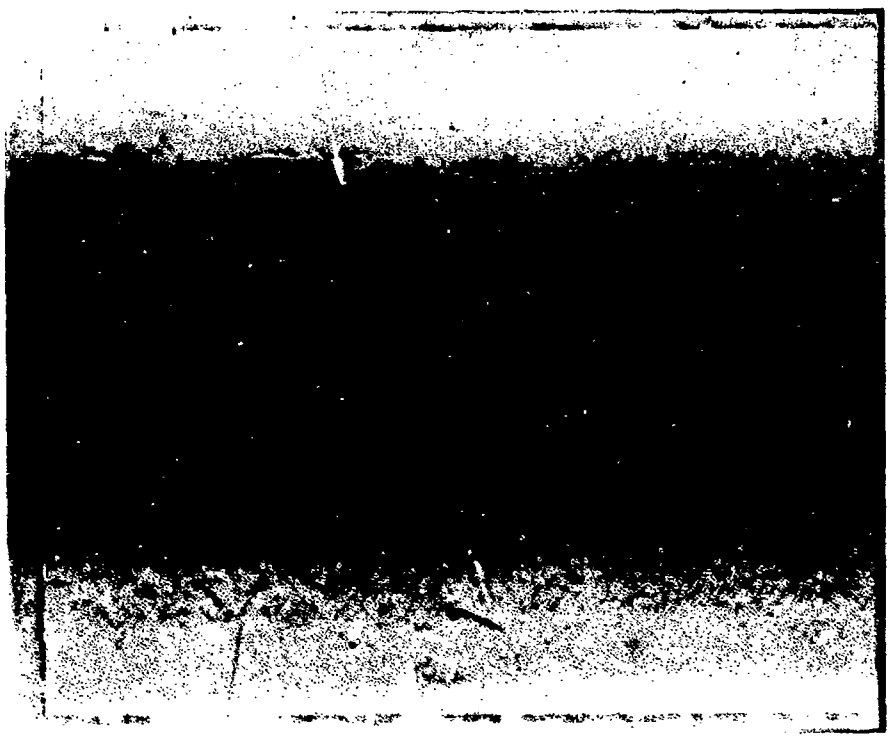

Figure 41 Final Fracture, Specimen 90G0704

Since the lowest stressed failure had fractured at a large number of cycles, 53803, the author determined that a specimen with perhaps a five percent decrease in stress could possibly run-out. Therefore, the final test would be executed at seventy-seven percent of ultimate.

Unfortunately, plate 90G07XX had now been exhausted. A specimen from plate 90G04XX was prepared for testing. Modulus tests on specimens from this plate showed its longitudinal modulus was nearly equal to those obtained from plate 90G07XX. Due to the scarcity of material in this plate, static tensile tests could not be performed. The ultimate stress was assumed equal to 348 MPa, the same as 90G07XX.

Specimen 90G0409 was tested at 270 MPa. As stated earlier, this was designed to be seventy-seven percent of ultimate. The results of the test are given in figure 42 and 43. Figure 42 depicts the stress-strain curves for the specimen. There is residual strain incurred albeit a small amount. The change in slope of the curves is minor. Once again, though, there appears to be a matrix microcrack closure level of approximately 80 MPa, where the slopes approach that of cycle one. The small change in slope is consistent with the results in figure 43. In this graph, a modulus degradation of only five percent occurred in the test.

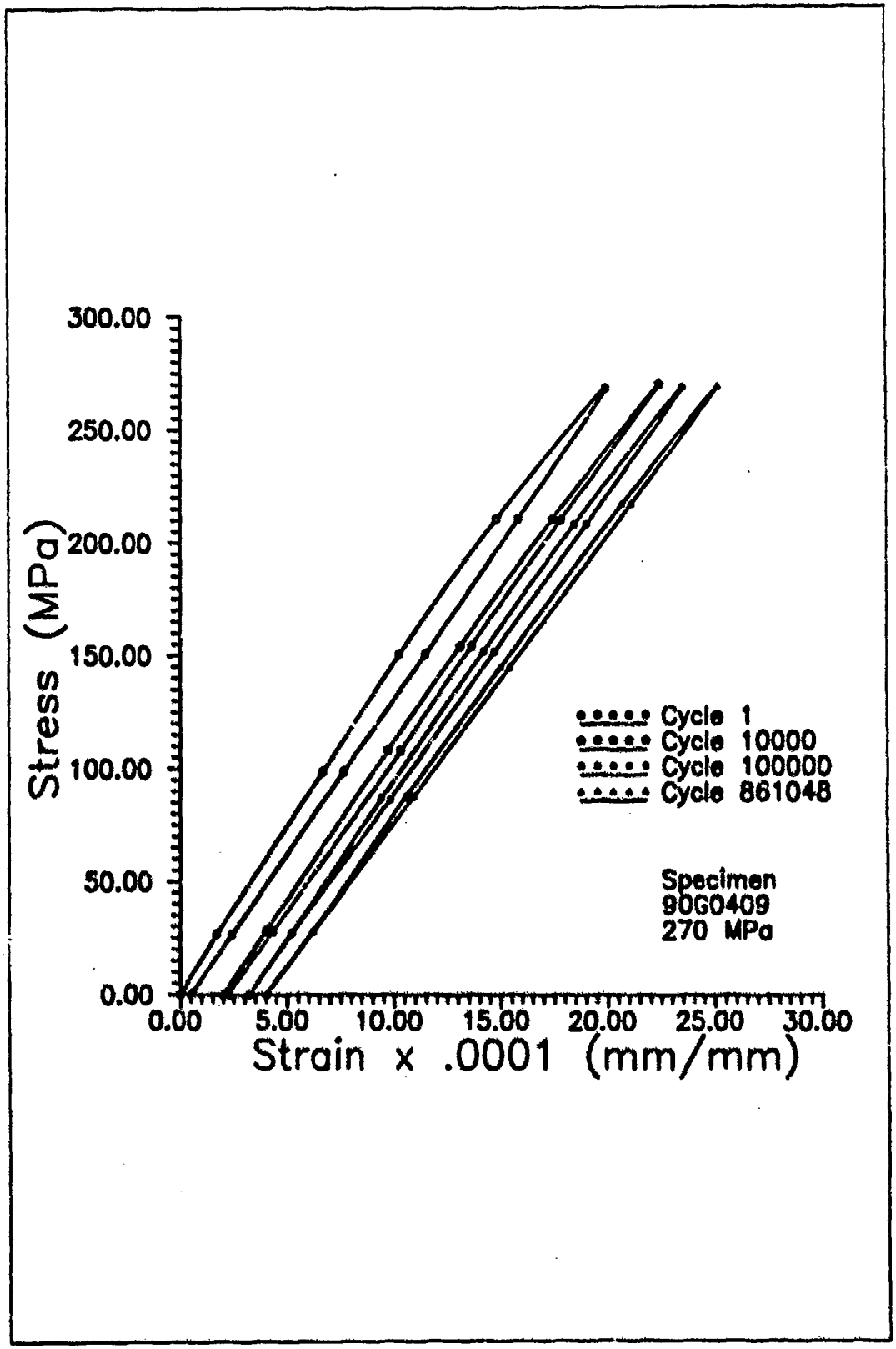

Figure 42 Stress vs. Strain 270 MPa Test

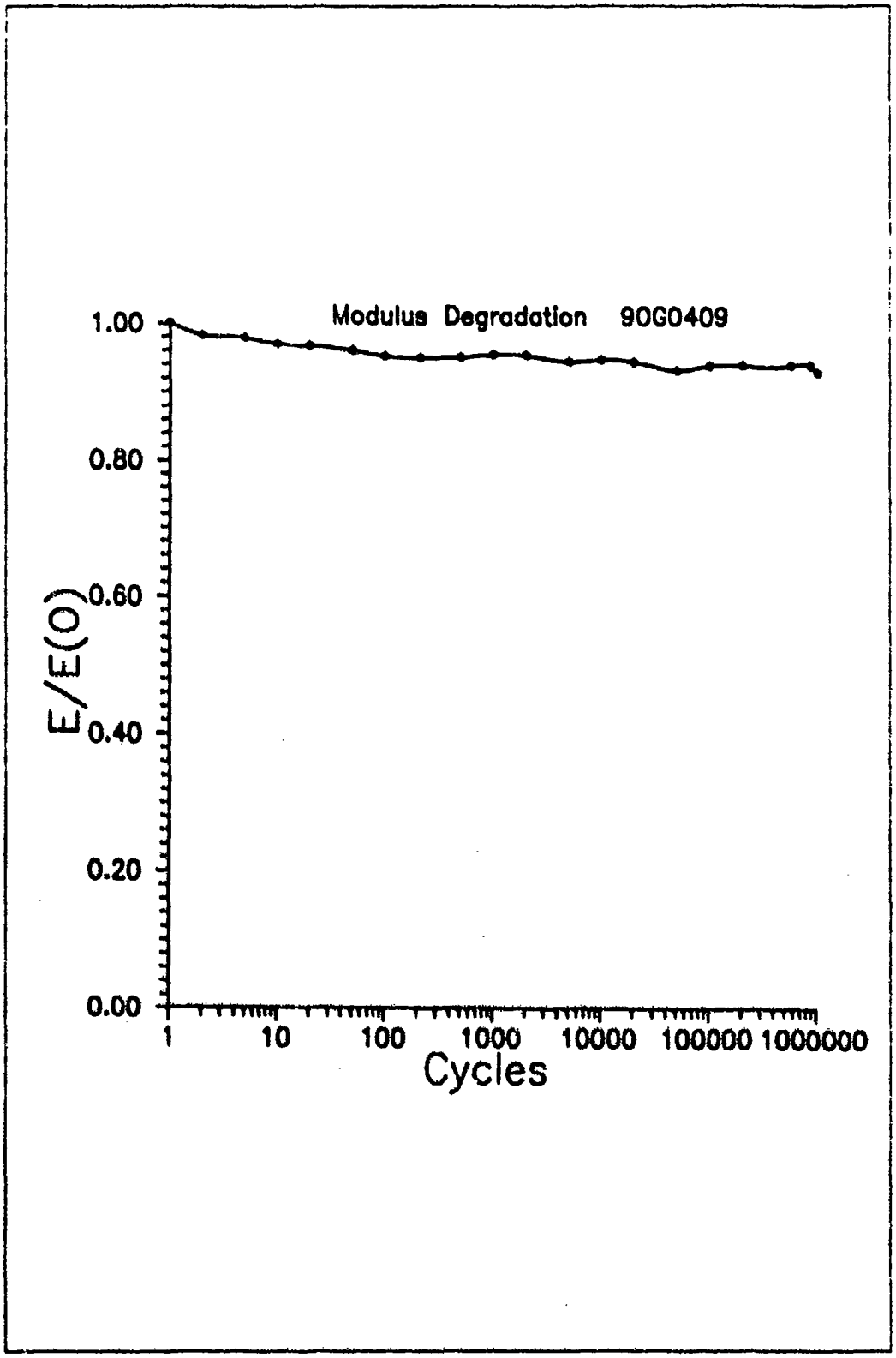

Figure 43 Modulus Reduction 270 MPa Test

Even though this change is less than those of the 90G03XX plate that ran-out with much less stress, the test was considered valid. Plate to plate property variations, due to processing, could account for these differences. This specimen did survive one million cycles of testing. Thus, an endurance limit could now be projected as occurring between eighty-three and seventy-seven percent of ultimate stress.

The final S-N curve is presented in figure 44. This figure clearly shows the dependence of fatigue life on applied maximum stress level. More importantly, there is a clear separation between failure and run-out, designated the endurance limit.

The notch definitely induces a stress concentration on the specimen. This is supported by the much lower ultimate stress versus unnotched ultimate stress. This is also supported by the fracture surface of the specimens which showed large cracks emanating from the points on the hole of theoretical maximum stress concentration. In addition, notched specimens had a much lower endurance limit than unnotched SiC/1733 specimens. Cracks grew in the matrix longitudinally in each ply, coalescing through the thickness into single cracks growing in the loading direction, eventually leading to fiber breakage in the crack area and specimen failure.

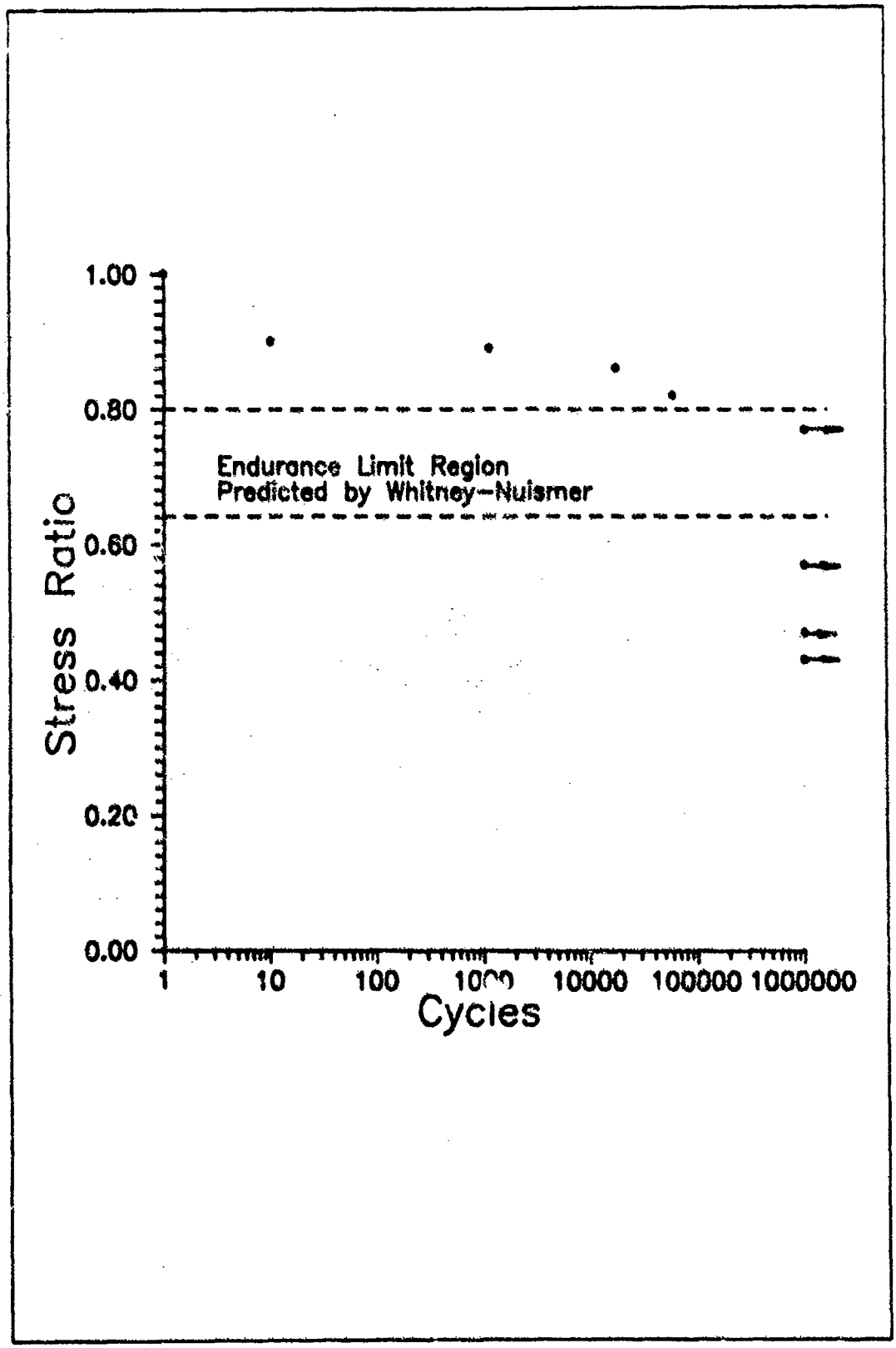

Figure 44 S-N Curve $[0]_s$ Specimens

2. Analytical Comparisons The objective of this section is to apply several models described in Chapter II to see if fatigue behavior of SiC/1723 can be characterized or predicted by existing models. The models examined were the Fatigue Modulus Model, Elastic Modulus Degradation Model and the Whitney-Nuismer Model. The results will be discussed here and how well they correlated to actual data.

The Whitney-Nuismer Model had been extended successfully to fatigue by Tsangarakis [18],[38]. He predicted the endurance limit of a metal matrix composite quite closely using this model. In addition, using thermographic examination of his specimens, he was able to experimentally detect the damage zone, d_0, that is described in Chapter II. This was beyond the scope of this study. However, a basic premise of the Whitney-Nuismer Model is that d_0 is a material property and a constant. Therefore, the notched ultimate strength to unnotched ultimate strength ratio was a function of d_0. Tsangarakis stated that the notched endurance limit to unnotched endurance limit would be equal to the same d_0 function as the ultimate strength ratio.

This model was appropriate because data existed on unnotched SiC/1723 from Butkus and Zawada [22]. In addition, tests had been performed on unnotched, unidirectional SiC/1723 at AFIT [35].

The three plates used in this study yielded a notched average ultimate stress of 324 MPa. The unnotched specimens had an ultimate stress ranging from 550 MPa to 680 MPa. Butkus and Zawada determined the endurance limit for unnotched SiC/1723 to be 440 MPa. The ultimate stress ratio was then equated to the endurance limit ratio of notched (unknown) to unnotched (known) SiC/1723. The author decided not to average the unnotched ultimate strength values, but, to use the maximum and minimum values as a window for the endurance limit. The equations used are shown below.

$$\frac{324}{550} = \frac{\sigma_{N_{el}}}{440} \tag{40}$$

$$\frac{324}{680} = \frac{\sigma_{N_{el}}}{440} \tag{41}$$

The calculated endurance limit from equations (40) and (41) yielded a range of 210 MPa to 259 MPa. These values were normalized by dividing them by the notched average ultimate stress of 324 MPa. The normalized ratios vary from .65 to .80. These endurance limit ratios are depicted in figure 44 as the dashed horizontal lines. The window that the model predicts is quite close to experimentally determined values. Therefore, Whitney-Nuismer is a good candidate for fatigue prediction of SiC/1723.

Results were not as good with the other two models applied to this laminate. These were the Fatigue Modulus Concept proposed by Hwang and Han and the Elastic Modulus Degradation Model put forth by Jen et. al.

The Fatigue Modulus Concept was encouraging because stress-strain data over test life was recorded. The constants A and c, described in Chapter II, were determined from one of the failed specimen's data. However, when the model was applied to other specimens, the life prediction results were grossly in error. Perhaps this model is not applicable to SiC/1723 because the slopes of the stress-strain curves were not linear as assumed by Hwang. Recall that the stress-strain curves were linear up to the matrix microcrack closure stress, then the slope changed suddenly giving the overall curve a non-linear appearance. The author tried to apply the linear assumption to SiC/1723 data and this could be a limitation of the model. Also, Hwang applied the model to graphite/epoxy specimens and their fatigue behavior could be quite different than a ceramic composite such as SiC/1723.

Results were the same using the Elastic Modulus Degradation Model by Jen. This model was also encouraging because the software that controlled the fatigue testing monitored the longitudinal stiffness throughout the test. Therefore the modulus degradation versus cycle could be calculated easily. Unfortunately, when the constants

described in Chapter II were determined from a single cycle as was done on the previous model and applied to the other tests, there was no correlation to actual data. Perhaps the discrepancy arose from the power function assumption of Jen. Looking at his data, figure 1, graphite/epoxy showed little decrease in modulus until almost ten thousand cycles. SiC/1723, however, exhibited steady damage accumulation throughout the test. The higher stressed specimens displayed extensive damage in the first few cycles. Hence, a simple power function assumption may not be appropriate. The difference in materials may also be a key in the discrepancy in correlation. Jen also used graphite/epoxy and, as with the Fatigue Modulus Concept, perhaps SiC/1723 simply is not appropriate due to the difference in behavior and properties from graphite/epoxy.

C. Bidirectional Specimens

1. Experimental Results Phase two of experimental work consisted of the fatigue testing of $[(0/90)_1]_s$ lay-ups of notched Sic/1723. Specimens had the same D/W ratio as the unidirectional laminates and were the same length. The objective of this phase was to determine how the transverse plies in the composite affected the overall fatigue behavior.

A great deal of literature exists describing the fatigue behavior of bidirectional laminates. Caslini, Zanotti and O'Brien [39] performed fatigue test on $[0/90]_{(n)s}$ glass/epoxy. They found the dominant damage modes to be extensive transverse matrix cracking in the 90^0 plies. This was followed by delamination at the $0^0/90^0$ interface. Final fracture occurred with fiber failure in the 0^0 laminae.

Sbaizero and Evans [40] investigated the tensile characteristics of bidirectional SiC/LAS. They also found extensive matrix cracking in the 90^0 plies. However, they did not record delamination at the $0^0/90^0$ interface as was done by Caslini et. al.. Instead, they found longitudinal cracks growing in the 90^0 plies close to the $0^0/90^0$ interface, which they called delamination cracks. In their work, the transverse cracks were intercepted or deflected into delamination cracks.

Mallick [41] confirmed the results of Sbaizero and Evans. He stated fatigue failure in a symmetric cross-ply laminate begins with the formation of transverse microcracks at the fiber/matrix interface in the 90^0 layers. As cycling continues, these cracks propagate across the 90^0 laminae until they reach the 0^0 plies. Some of these cracks are then deflected parallel to the 0^0 plies causing delaminations. Others are stopped at the $0^0/90^0$ interface. This process is shown in figure 45 (from Mallick [41]).

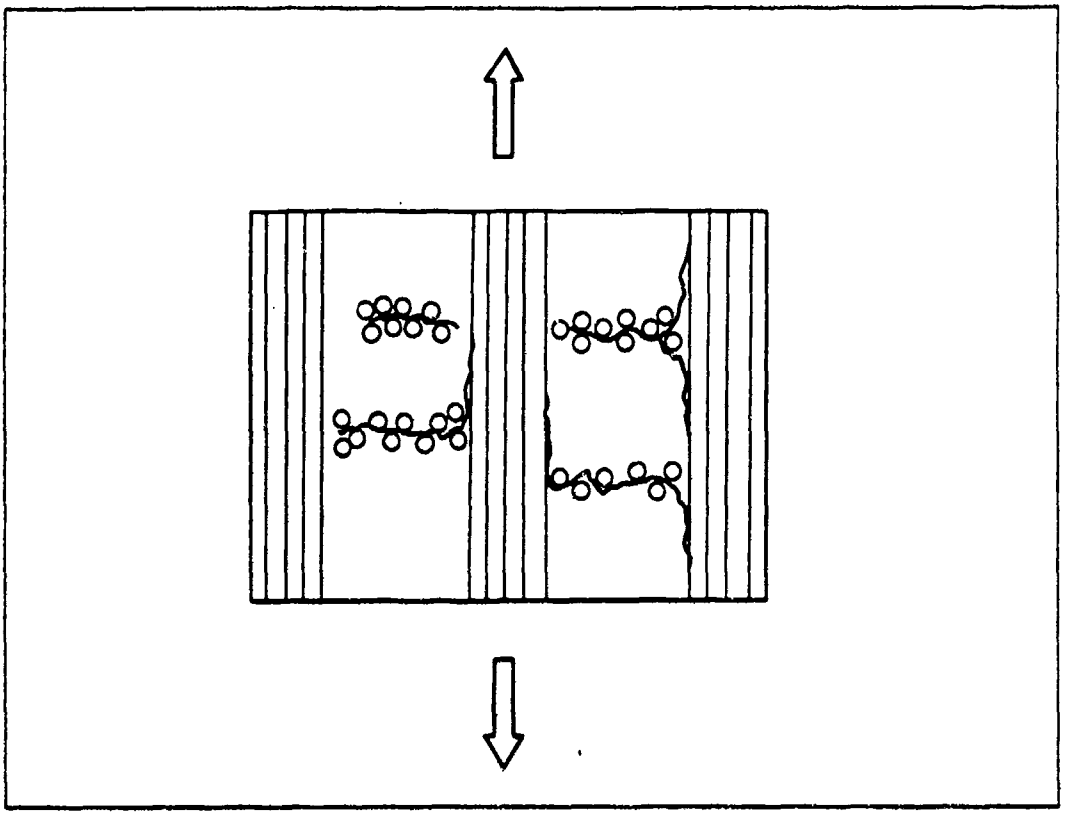

Figure 45 Damage Development During Tension-Tension Fatigue Tests of $[0/90]_s$

Similar results are discussed by Chawla [42] who reported on work done by Hahn and Lorenzo on a bidirectional laminate.

Due to these similar findings, the author concluded that edge replicas would allow recording of the transverse and delamination cracking in SiC/1723, if SiC/1723 had the same damage modes. However, the effect of the hole was unknown. It was possible that fractures similar to the unidirectional lay-up could override the transverse cracking in the 90° plies.

Specimens were prepared from plate 91G01XX, see appendix II for specimen dimensions and test conditions.

All tests were conducted on specimens from this plate. As was done before, tensile tests were performed on notched specimens to determine the ultimate strength. Fractions of this level would then be selected for fatigue maximum stresses. The results of one tensile test are presented in figure 46, stress vs. strain for specimen 91G0111. An interesting feature is the existence of two proportional limits. The curve goes non-linear at approximately 60 MPa, indicating damage in the weaker 90^0 plies. The curve then regains linearity until 150 MPa where damage in the 0^0 plies causes a second non-linearity point. The curve continues in a non-linear fashion until failure at 223 MPa. A second tensile test yielded an ultimate stress of 217 MPa. The fracture surface is shown in figure 47. It appears that the 90^0 plies retard the longitudinal crack growth found in the unidirectional specimens. Fracture occurred across the hole suggesting transverse, through the thickness, cracking, leading to failure. It remained to be seen whether the fracture surface was due to a stress concentration or the fact that at the hole, it is the smallest cross-section, requiring less travel for crack propagation.

The first two fatigue tests, specimens 91G0103 and 91G0105 were tested in the region between the first proportional limit and the second. The purpose was to determine whether damage in just the 90^0 plies would be sufficient for fatigue failure.

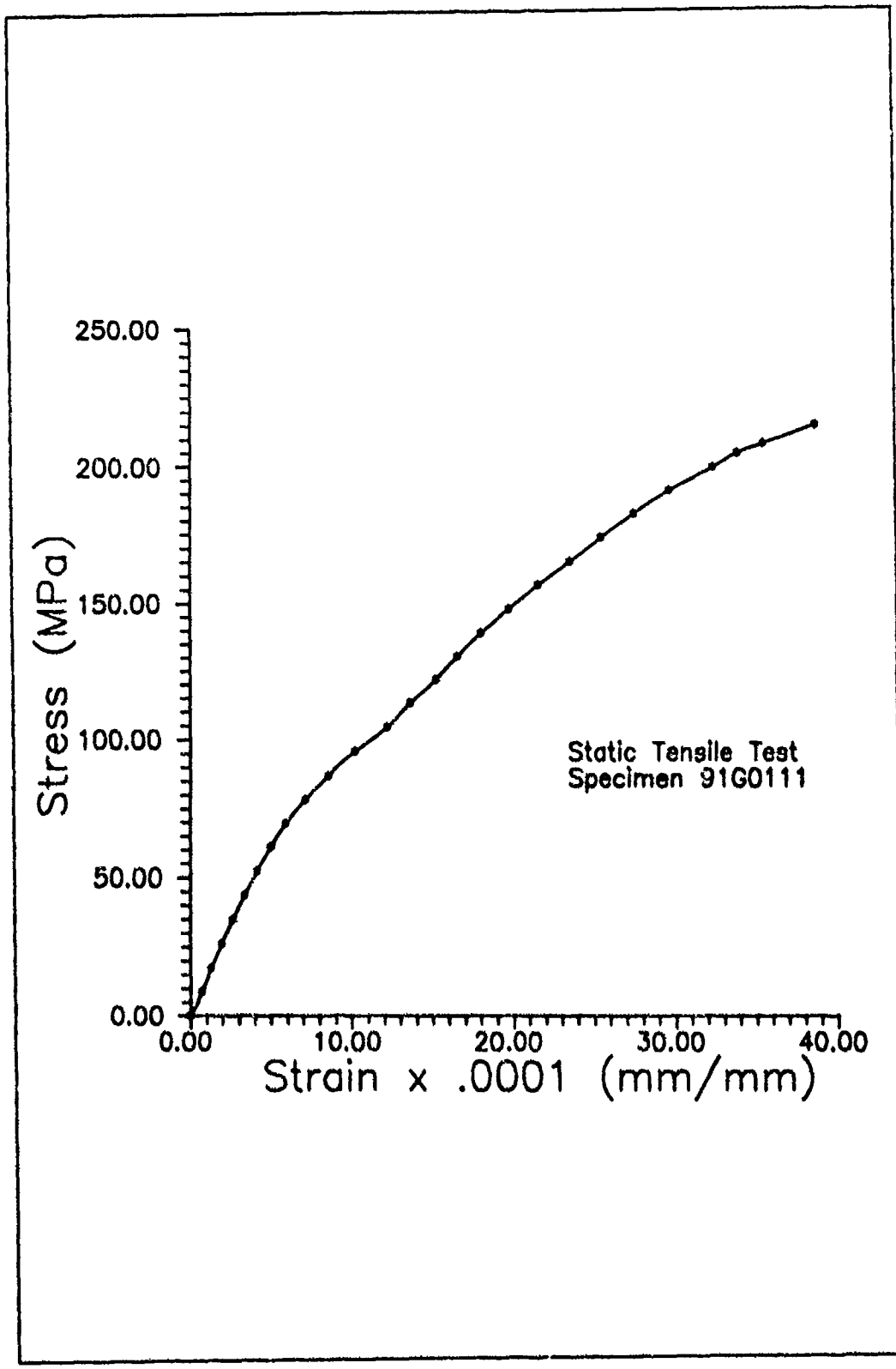

Figure 46 Stress Vs. Strain Specimen 91G0111

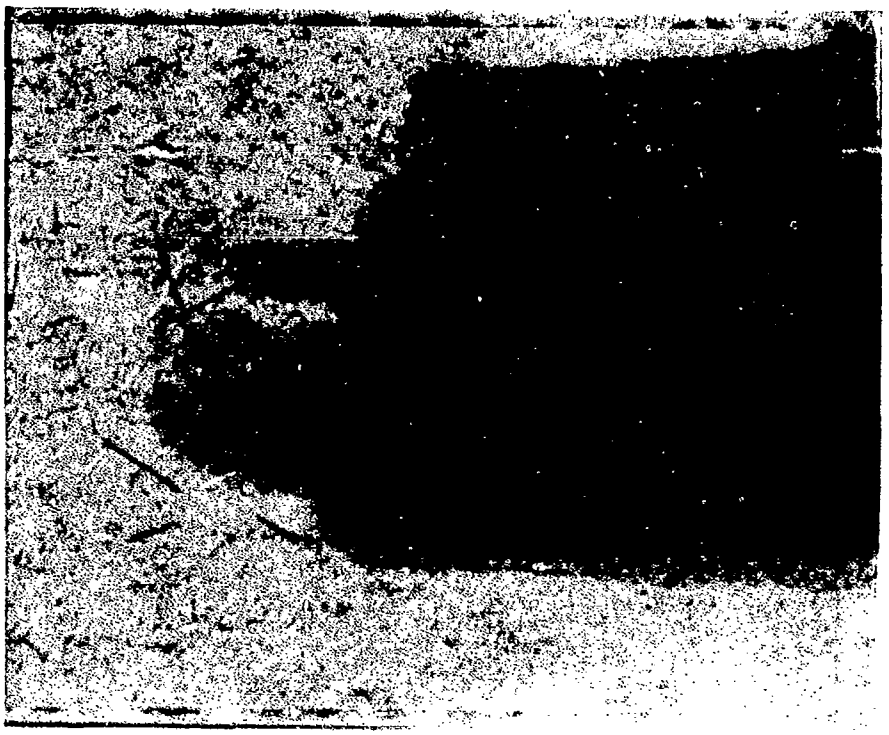

Figure 47 Final Fracture Specimen 91G0111

Specimen 91G0103 was tested at a maximum stress of 88 MPa. Problems with the extensometer prevented accurate measurement of residual strain accumulation, however, modulus degradation was recorded. The results are shown in figure 48, modulus reduction over test life. This curve indicates damage occurs early in the test with a thirty percent reduction in stiffness by 1000 cycles. After 1000 cycles, the modulus stabilizes until run-out at one million cycles. Edge replicas were taken on this specimen to try and account for the steep early decrease in modulus. All replicas were taken under load based on results obtained by Marshall and Evans [36]. They found that cracks would close up as load was decreased, leading one to believe an area was damage-free when in fact, substantial cracking had transpired. A micrograph of a replica from the test is presented in figure 49. A matrix crack that has propagated through the middle two 90^0 plies is shown in the figure. The test produced cracking such as this randomly on the edge in the gage section. These cracks only appeared in the transverse plies. Notice that the crack appears to be deflecting longitudinally as it approached the 0^0 layer, which is shown at the bottom of the figure. The 90^0 plies appear as the region with circles, which are the cross-sections of the fibers running transverse to the loading direction. This damage corresponds with the sudden decrease in modulus shown in figure 48

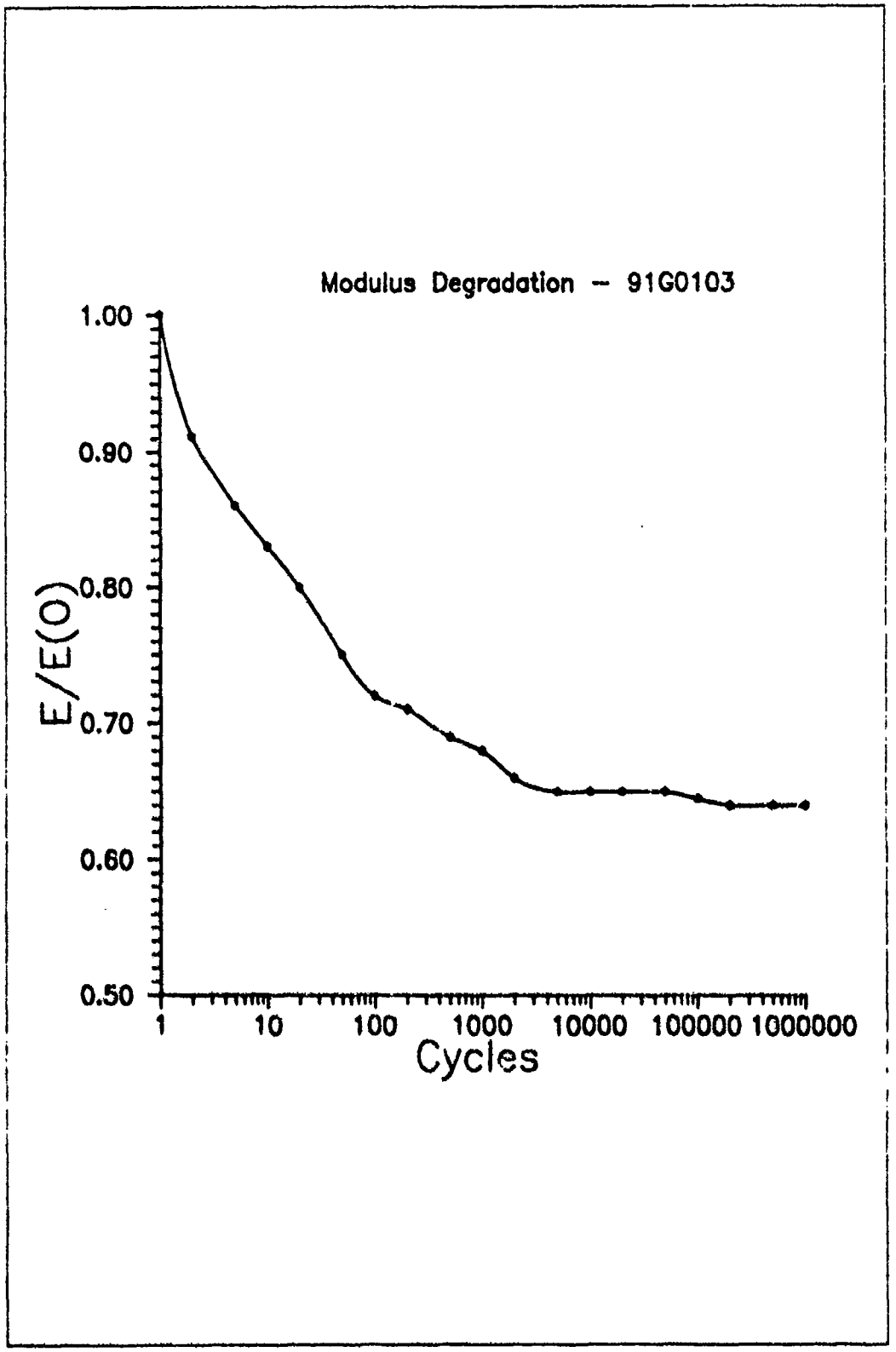

Figure 48 Modulus Reduction 88 MPa Test

Figure 49 Crack in Transverse Plies, 88 MPa Test
200X Magnification, Cycle 1026

because cracks appeared immediately, extending to their final lengths by the time the modulus began stabilizing. It should be noted that cracks did not extend into the 0^0 plies , therefore they can be assumed to be damage-free. This is to be expected since the test was performed below the second proportional limit from the static tensile tests. The second proportional limit being indicative of damage in the 0^0 laminae.

The second test was performed, using specimen 91G0105, at 120 MPa maximum stress. This stress was also in the stress region between the two proportional limits. However, 120 MPa was close to the second limit and it was possible the specimen would fail. The results of this test are shown in figures 50 and 51. Figure 50 depicts stress-strain behavior over test life, figure 51 is modulus degradation.

The stress-strain curves show the non-linearity point of cycle one closely corresponds to the static tensile test specimens' first proportional limit. Subsequent tests show the matrix microcracking closure stress level seen in the unidirectional specimens. That stress level is constant regardless of cycle at approximately 40 MPa. Above 40 MPa, the cracks in the 90^0 plies are opened, allowing extension of the material and yielding a large change in slope or stiffness. Permanent damage that is not recovered by load elimination can be seen by the residual strain accumulation.

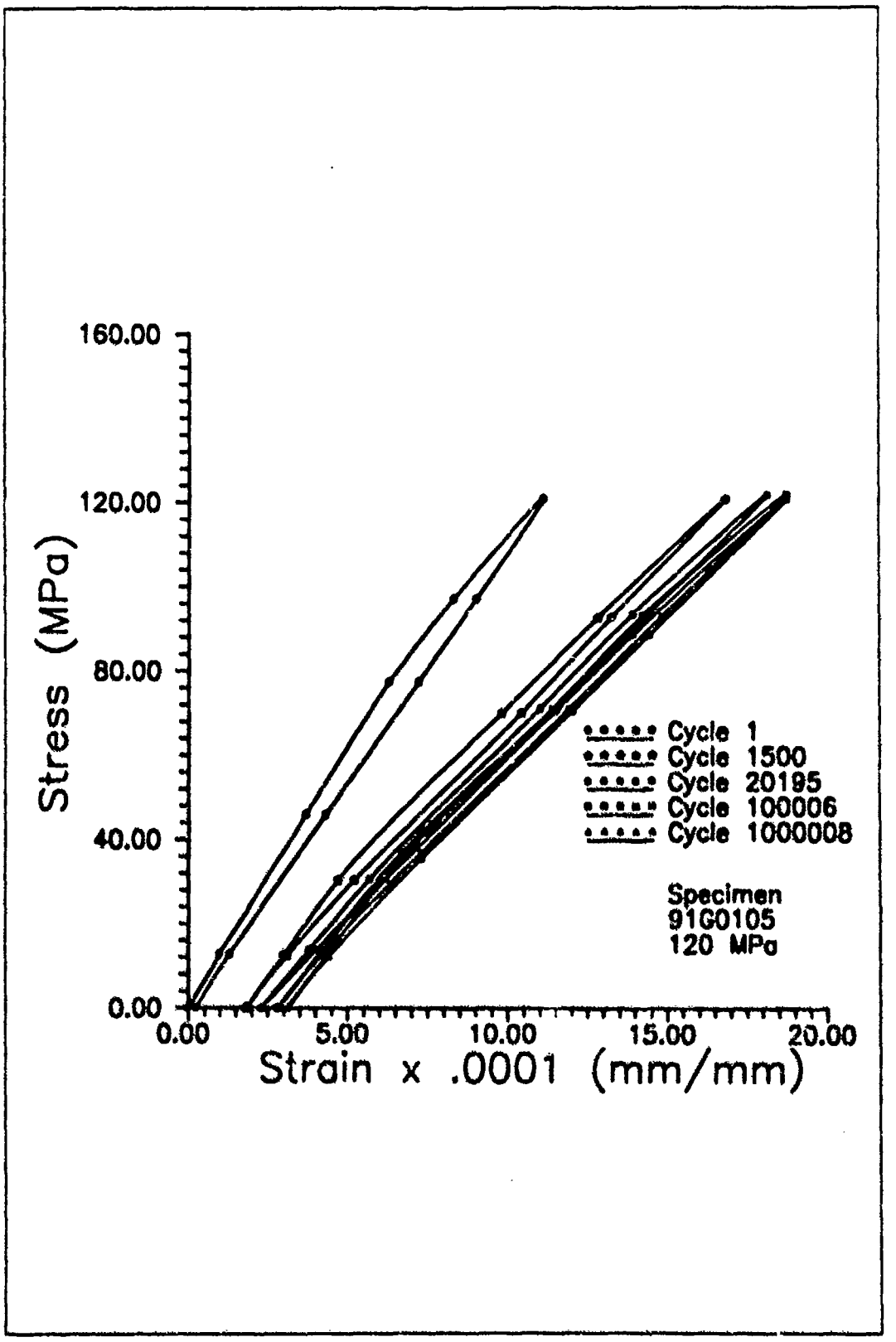

Figure 50 Stress Vs. Strain 120 MPa Test

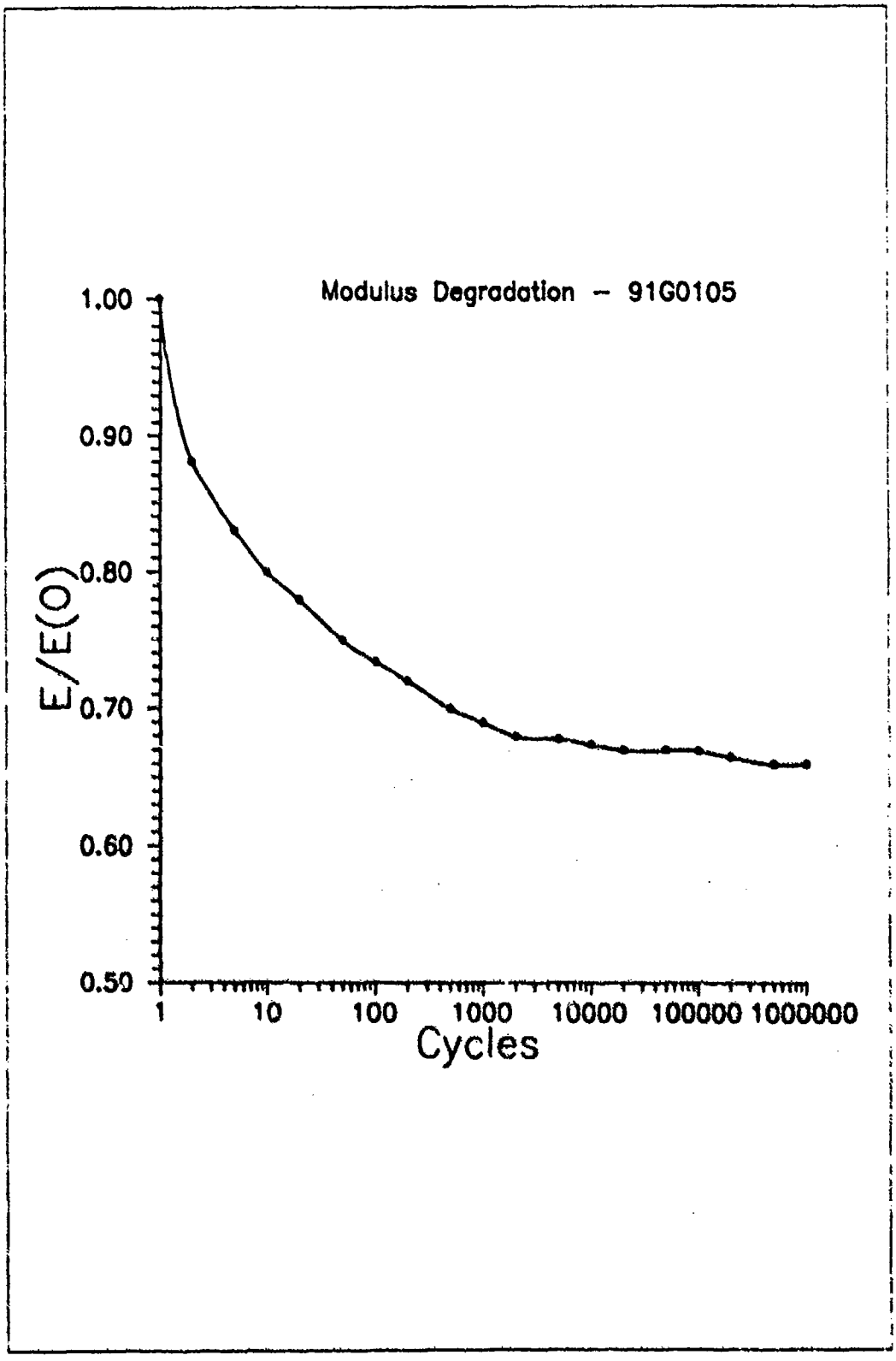

Figure 51 Modulus Reduction 120 MPa Test

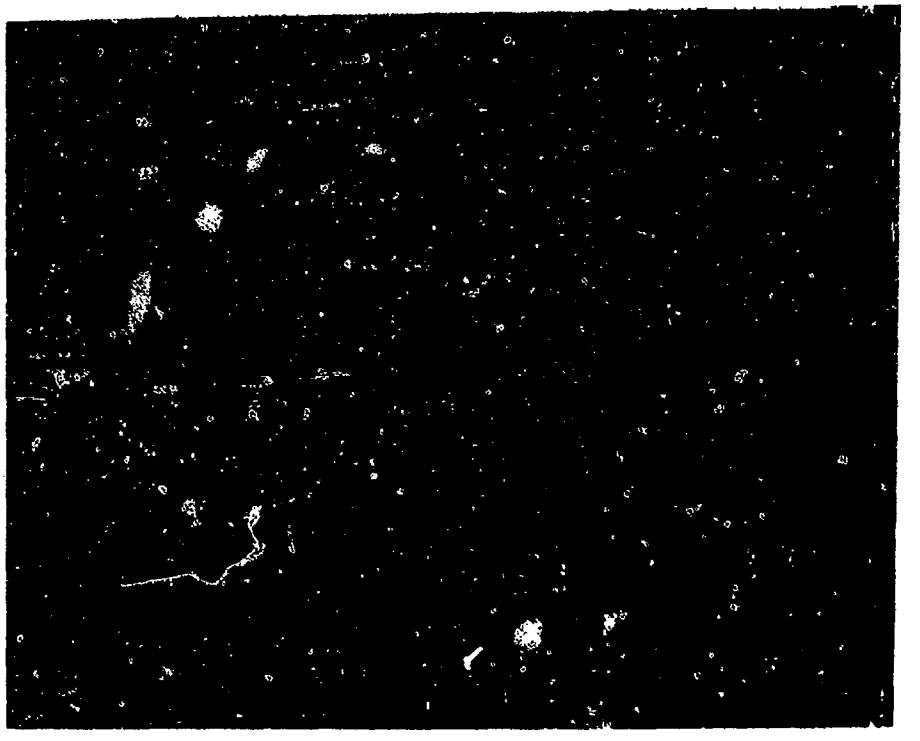

Figure 52 Cracks in Transverse Plies, 120 MPa Test
200X Magnification, Cycle 2145

Figure 51 shows the modulus degradation incurred by the specimen over the test life. As with the 88 MPa test, damage occurs swiftly in the 90^0 plies, stabilizing by one thousand cycles. This stabilizaation is shown further by examining stress-strain curves in figure 50. From cycle 1500 on, the slopes of the curves are nearly identical indicating little additional damage. An example of the damage in the specimen is shown in figure 52, which is a micrograph of an edge replica of the specimen. Damage was typical of this photograph. Transverse cracking spanned the 90^0 plies with deflections at the $0^0/90^0$ interface. Longitudinal cracks can be seen in the 90^0 layers near the ply interface running parallel with the 0^0 laminae. Several cracks such as in figure 52 appeared in the gage length. However, the cracks were random in appearance and not evenly spaced, suggesting the specimen was not in a highly stressed state. This test also ran-out to one million cycles.

The maximum stress level was increased significantly for the third fatigue test. Specimen 91G0107 was tested with maximum stress of 180 MPa. This level is slightly higher than the second proportional limit determined earlier. Unidirectional specimens had run-out when tested at levels just over the proportional limit, but, it was unclear how a bidirectional laminate would react. The results of this test are shown in figures 53, 54 and 55.

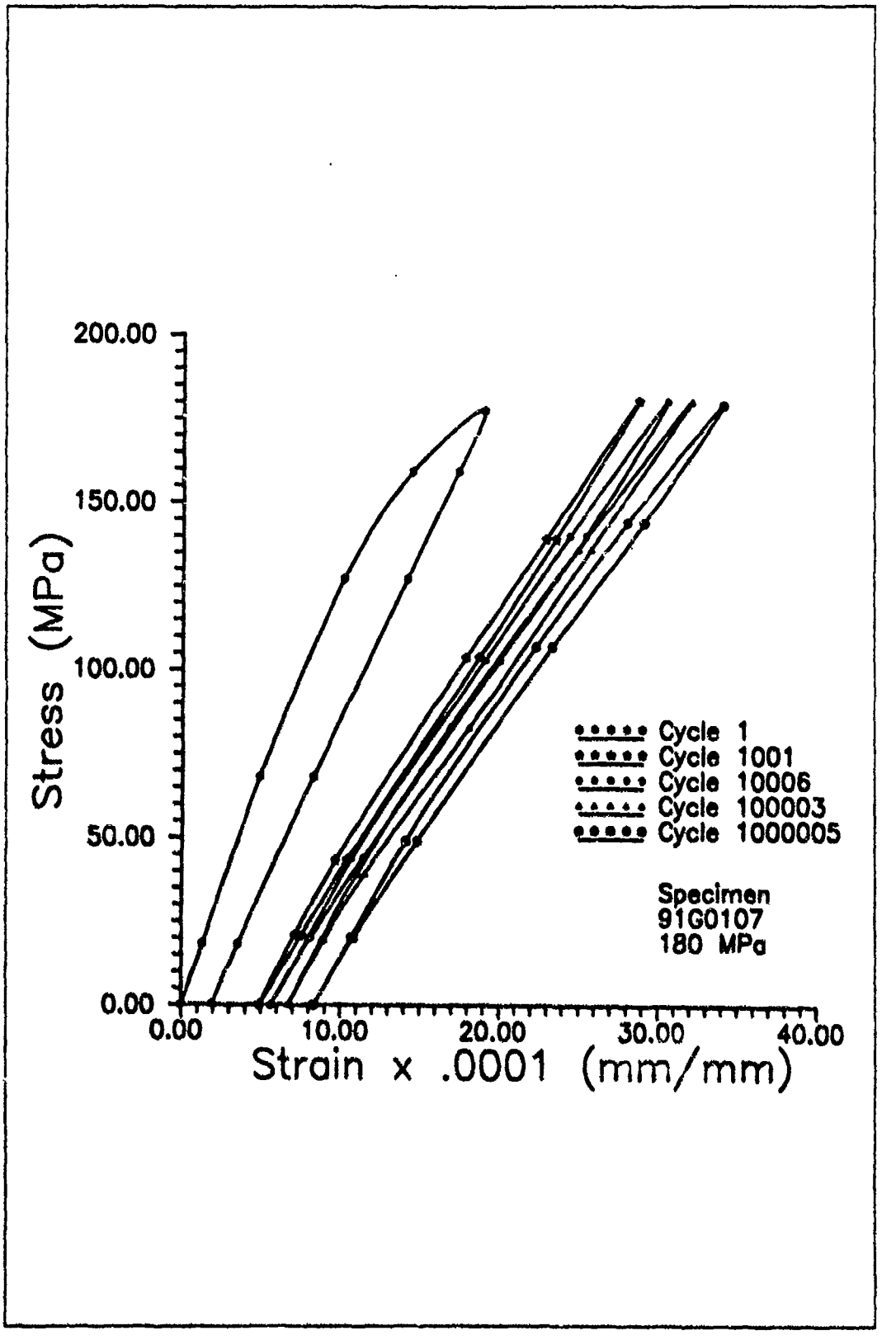

Figure 53 Stress Vs. Strain 180 MPa Test

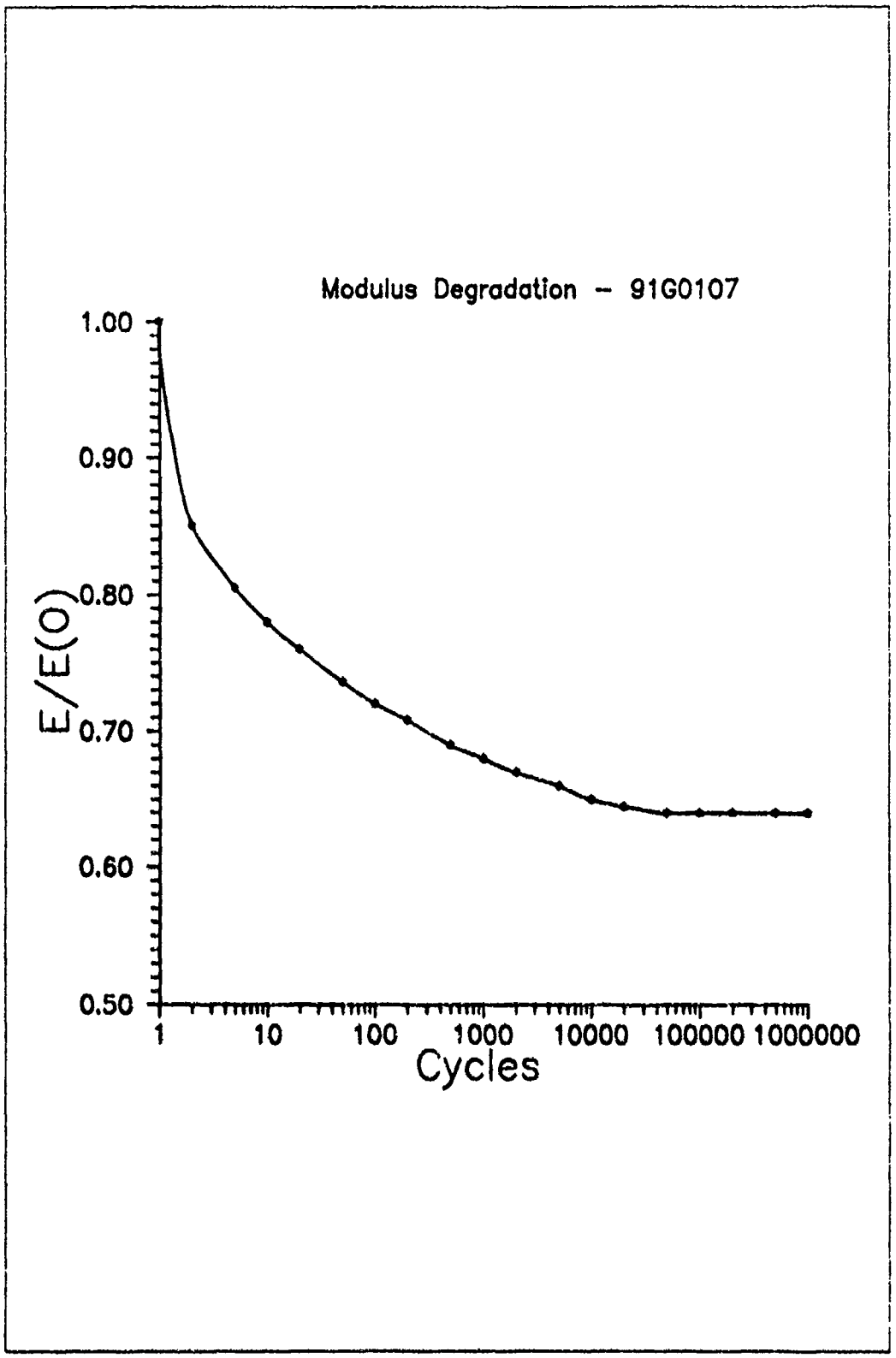

Figure 54 Modulus Reduction 180 MPa Test

Figure 55 Cracks in Transverse Plies, 180 MPa Test
200X Magnification, Cycle 101,000

Figure 53 shows the effects of the higher stress level on the laminate. The first cycle clearly depicts a much larger non-linear region than previous tests, suggesting higher levels of cracking than before. In addition, there is residual strain accumulation on the first cycle that was not present after the first cycle on the 120 MPa test. Total residual strain is almost double that of the 120 MPa test. The matrix microcrack closing stress seems to remain constant for it appears in figure 53 as 40 MPa, identical to the previous test. The slope of the stress-strain curves decrease greatly between cycle one and 1000, both above and below 40 MPa. After cycle 1000, the curves are nearly identical suggesting maximum damage has occurred early and has been retarded. This is supported by the results of figure 54, which show the modulus degradation. Extensive decreases in stiffness are shown, especially in the first ten cycles for this specimen. The stabilization of the modulus after 4000 cycles suggests no further damage is occurring.

Specimen 91G0107 did survive one million cycles of testing. Replicas taken showed transverse ply matrix cracking was the dominant damage mode, but, as yet, interface delamination did not occurr, nor fiber breakage in the 0° laminae. Figure 55 shows the transverse cracking through the 90° plies and some crack coupling between a transverse crack and longitudinal matrix crack.

Testing thus far had been at a maximum stress of 80 percent of ultimate without a failure. The author decided to increase stress substantially, obtain a failure point and then decrease stress levels gradually on other tests to fill in the bidirectional S-N curve.

Test four, specimen 91G0109, was executed at a maximum stress of 209 MPa. This level represented .94 of ultimate strength. The results of this test are given in figures 56 through 63.

The stress-strain curves of figure 56 show the effects of the high stress. Cycle one permanent strain accumulation is almost equal to the total residual strain of the 120 MPa test. This large residual strain component increased even more through 1042 cycles. Once again, the crack closure stress appears as 40 MPa. The decrease in slopes is substantiated by figure 57, which shows the modulus degradation. The stiffness is reduced early, typical of all bidirectional tests but instead of stabilizing, it continues to decrease until failure. Failure occurred at 87587 cycles.

Extensive replicas were taken on this test in the hopes of capturing all damage modes. Early in the test, a replica was taken in the center of the gage length. The micrograph of the replica is shown in figure 58. In this photo, regularly spaced transverse cracks appeared with a crack density that had not been encountered in previous tests.

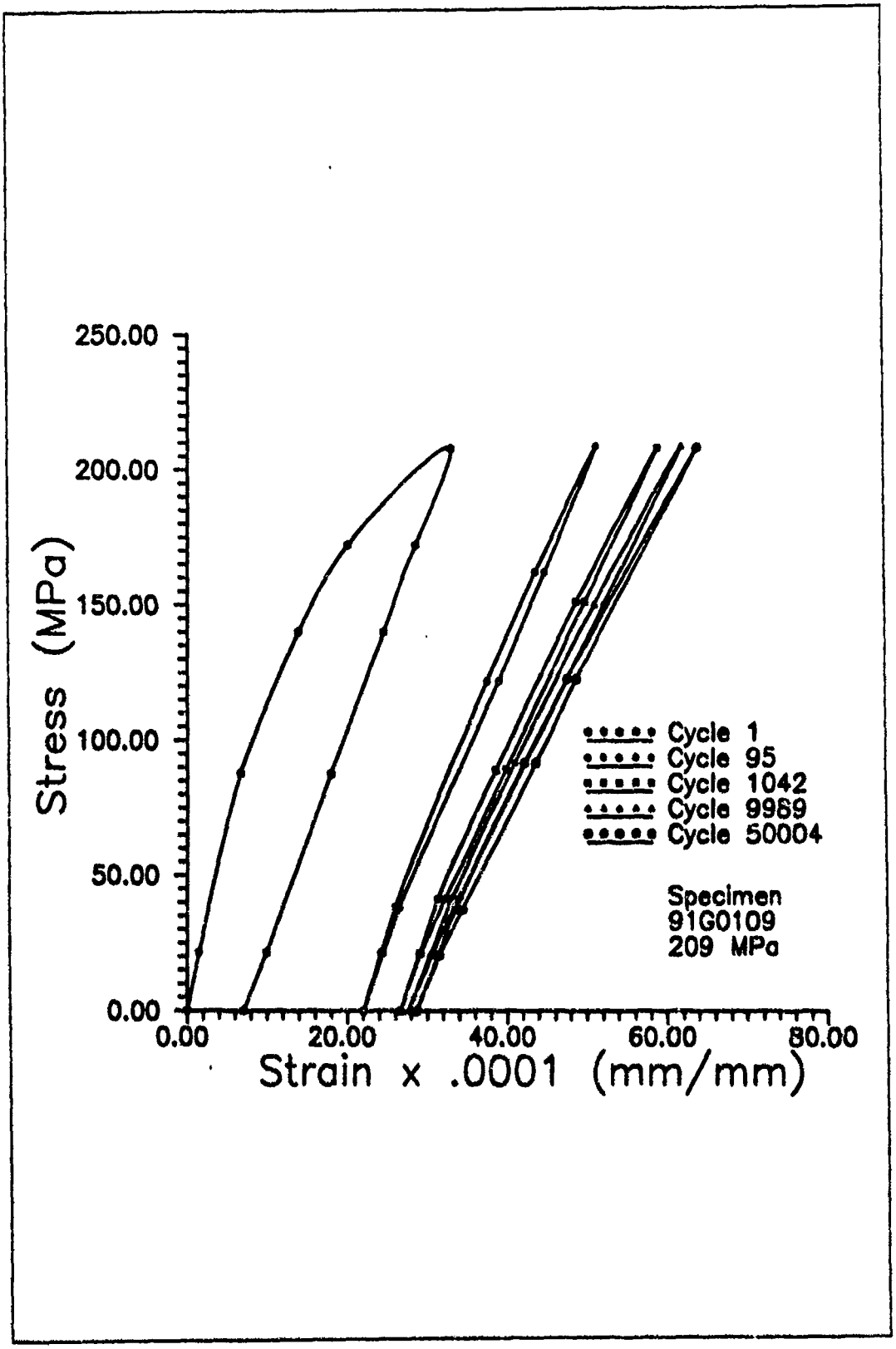

Figure 56 Stress Vs. Strain 209 MPa Test

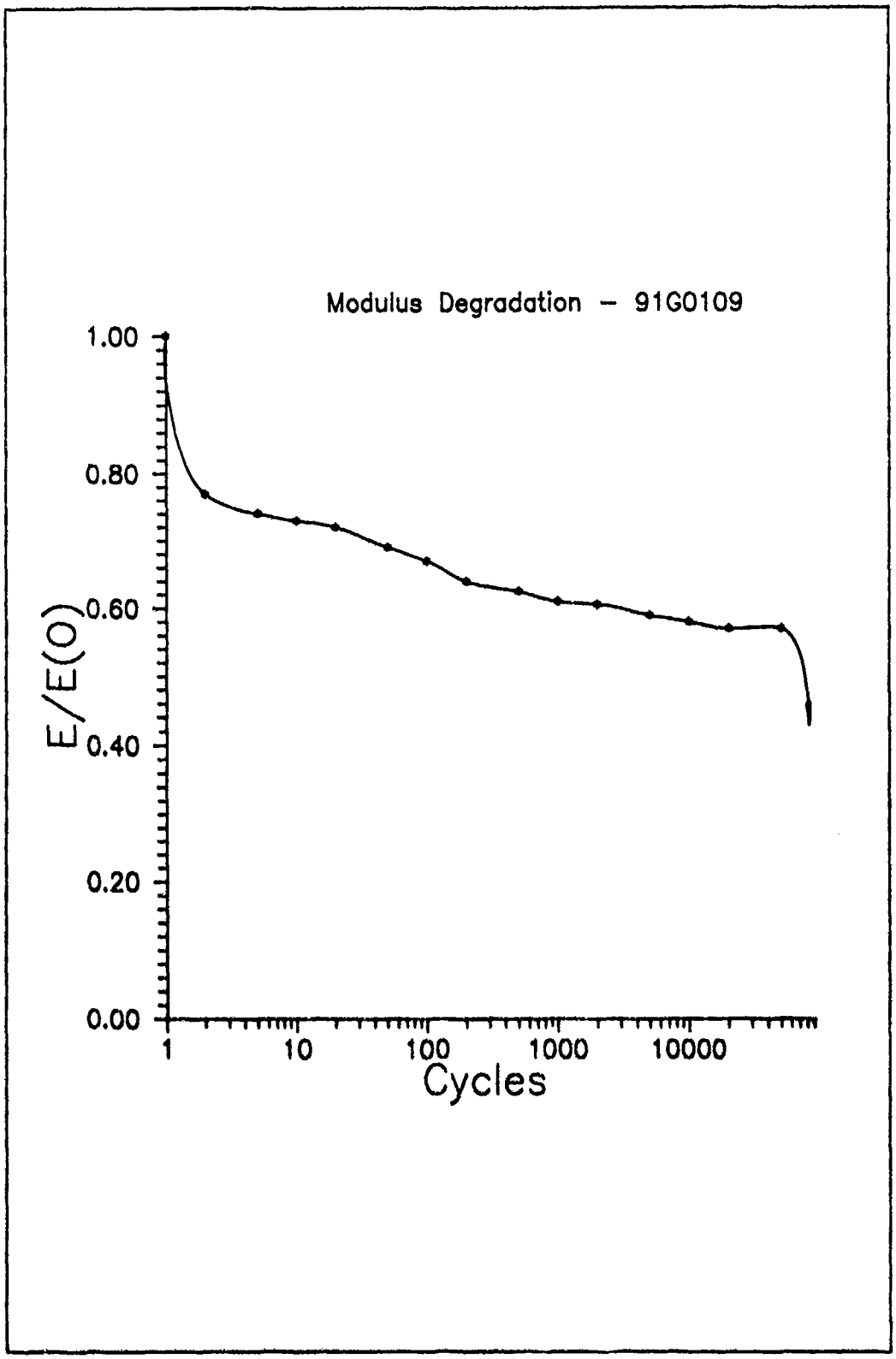

Figure 57 Modulus Reduction 209 MPa Test

Figure 58 Regularly Spaced Transverse Ply Cracks
209 MPa Test, 200X Mag., Cycle 94

Figure 59 Transverse Ply Cracks Away From Hole
209 MPa Test, 100X Mag., At Failure

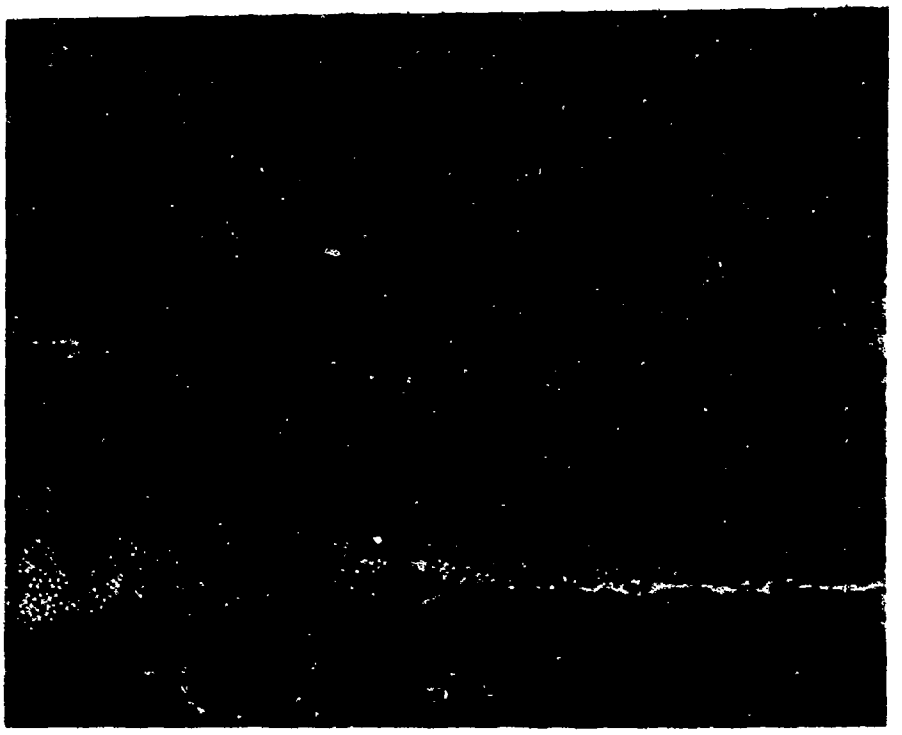

Figure 60 Transverse Ply Crack Far From Hole
209 MPa Test, 200X Mag., At Failure

Replicas taken a few millimeters from the center of the specimen, where figure 58 was obtained, show the same crack pattern but notice the decrease in crack density, see figures 59 and 60. Obviously, the area around the hole would be the critical damage zone.

The cracks near the hole were monitored closely for progression. The crack density did not increase as testing continued. They did propagate longitudinally near the ply interfaces, combining with other cracks. Eventually, the transverse cracks extended through the width causing fracture in the 90° plies. The coupling of the longitudinal cracks allowed for delamination followed by fiber fracture in the 0° laminae. These modes are all shown in the edge replica photographs of the fracture surface, figure 61. It is clearly shown how transverse matrix cracking has caused the 90° plies to fracture in a plane normal to the load direction. In addition, these plies delaminated from the 0° plies as evidenced by the intact 0° plies with the absence of transverse plies. The fracture of the 0° fibers occurred to the right of where this photo was taken.

A macroscopic view of the fracture surface is shown in figures 62 and 63. Figure 62 depicts the fracture across the width of the specimen. The final fracture is across the hole. This correlates with the high crack density that was shown in figure 58. A side view of the same fracture is given in figure 63. Delaminations can be clearly seen here.

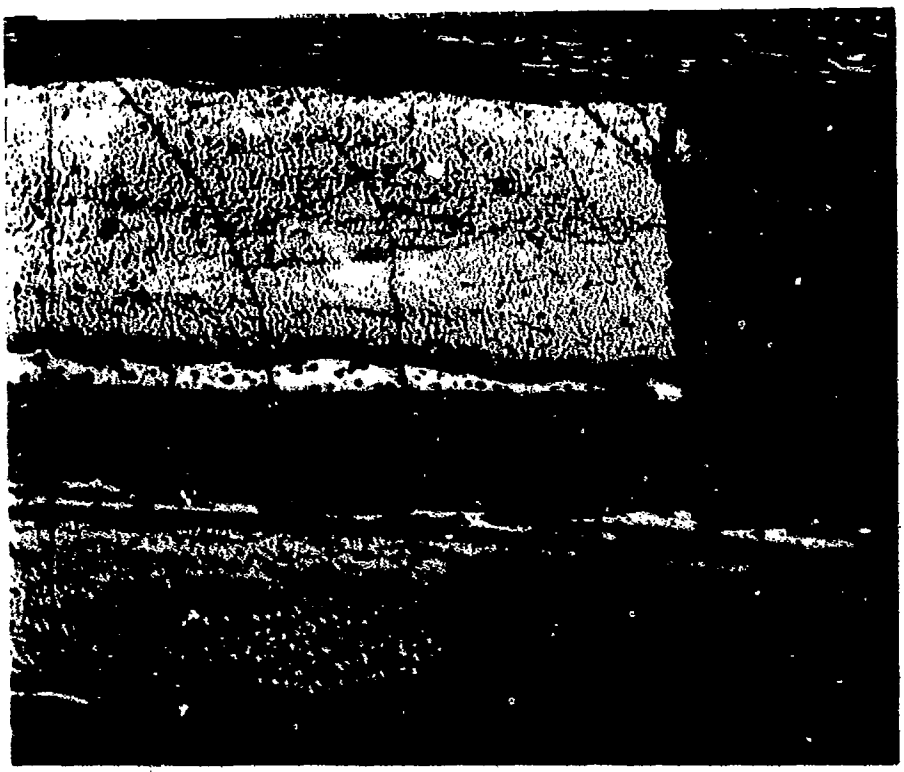

Figure 61 Fracture Surface, Side View
209 MPa Test, 50X Magnification

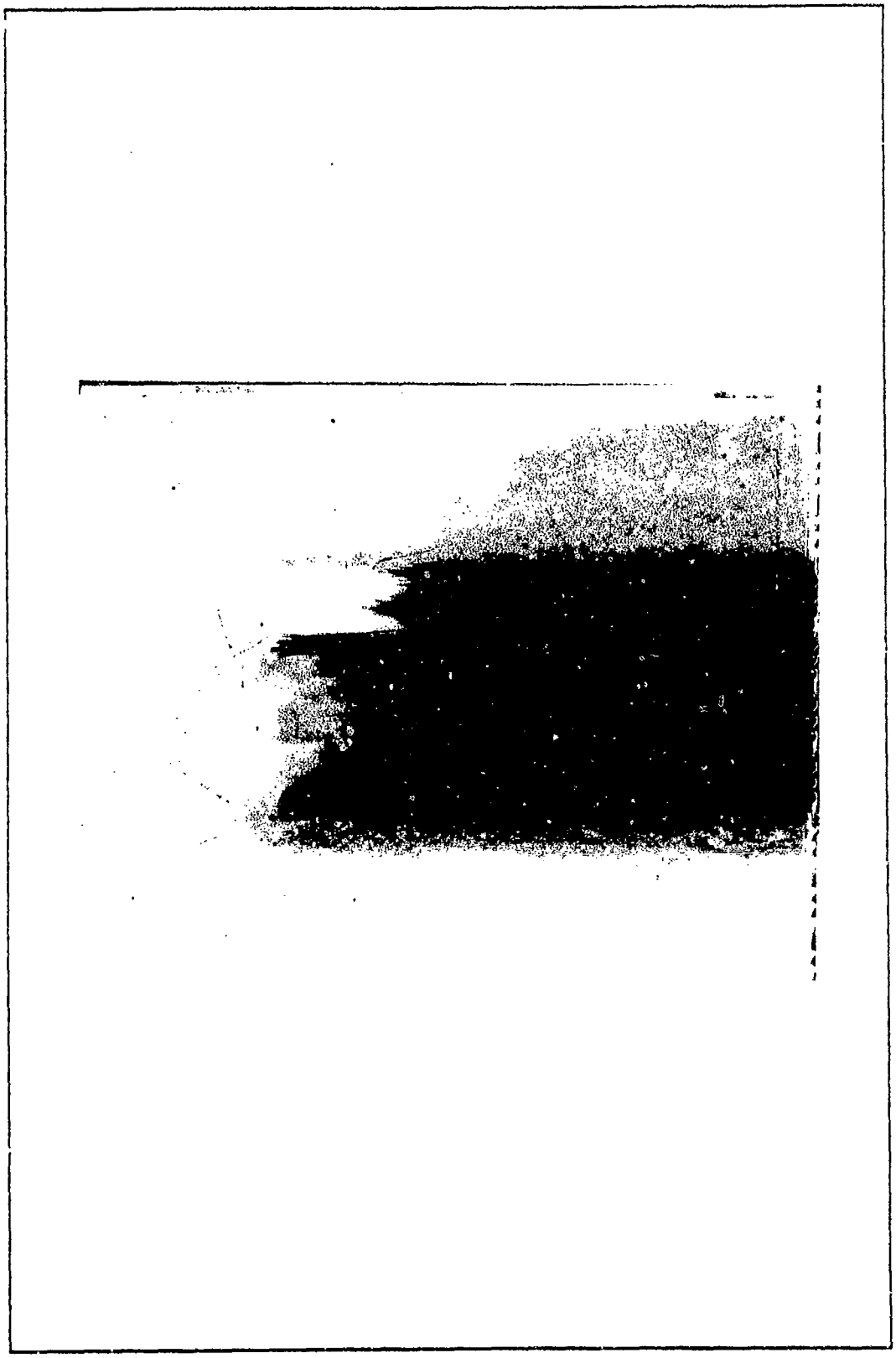

Figure 62 Fracture Surface, Across Width
209 MPa Test, 6.3X Magnification

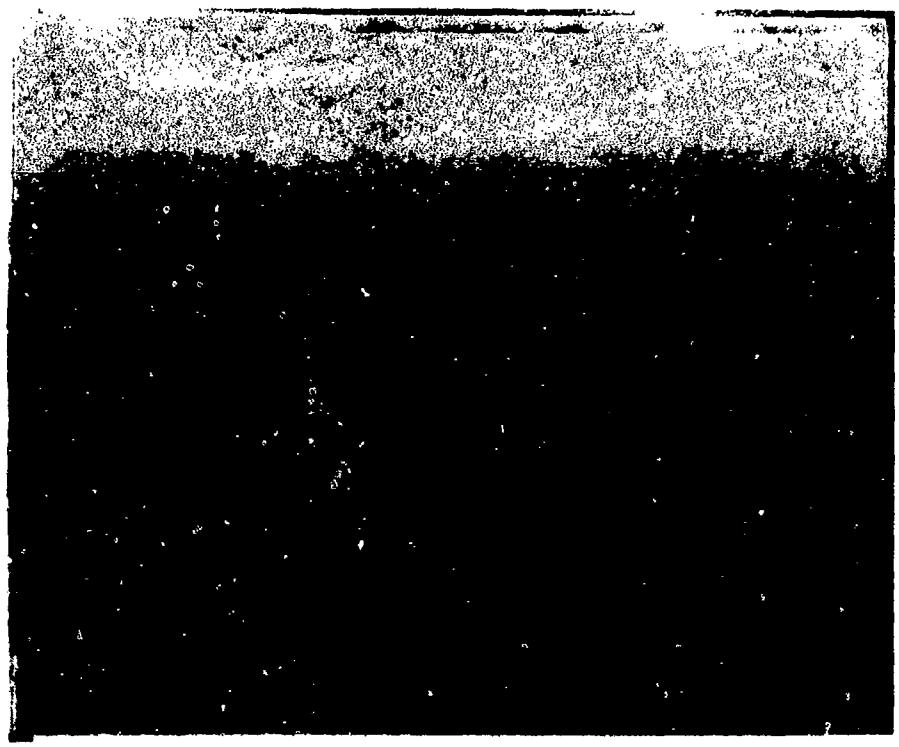

Figure 63 Fracture Surface, Side View
209 MPa Test, 6.3X Magnification

Test five was designed to approach run-out yet still have a reasonable chance at failure. Specimen 91G0110 was tested at 192 MPa maximum stress. This represented a value of .86 ultimate stress. The results of the test are given in figures 64 and 65.

The stress-strain results of figure 64 show trends that are almost identical to the 209 MPa test. This test also showed large amounts of residual strain early in the test. Final strain appeared to be larger than that in the 209 MPa test. However, data collection did not occur between 50000 and 87587 cycles in the 209 MPa test due to the logarithmic nature of the collection. Therefore, the actual final residual strain in the 209 MPa test was not computed.

The 192 MPa test shows steady decrease in stiffness throughout the test. The matrix crack closure level is again in the 40 MPa range. The steady degradation of stiffness is confirmed in figure 65. There is a sharp decrease in the first few cycles due to the establishment of transverse matrix cracks in the 90^0 plies. The steady decrease thereafter can be attributed to crack propagation and coupling at the ply boundaries leading to delamination. This specimen failed at 357881 cycles.

Since specimen 91G0110 had yielded a failure at .86 ultimate at such a large number of cycles and run-out had been achieved at 80 percent of ultimate, the final test would be run between the two failure points already obtained.

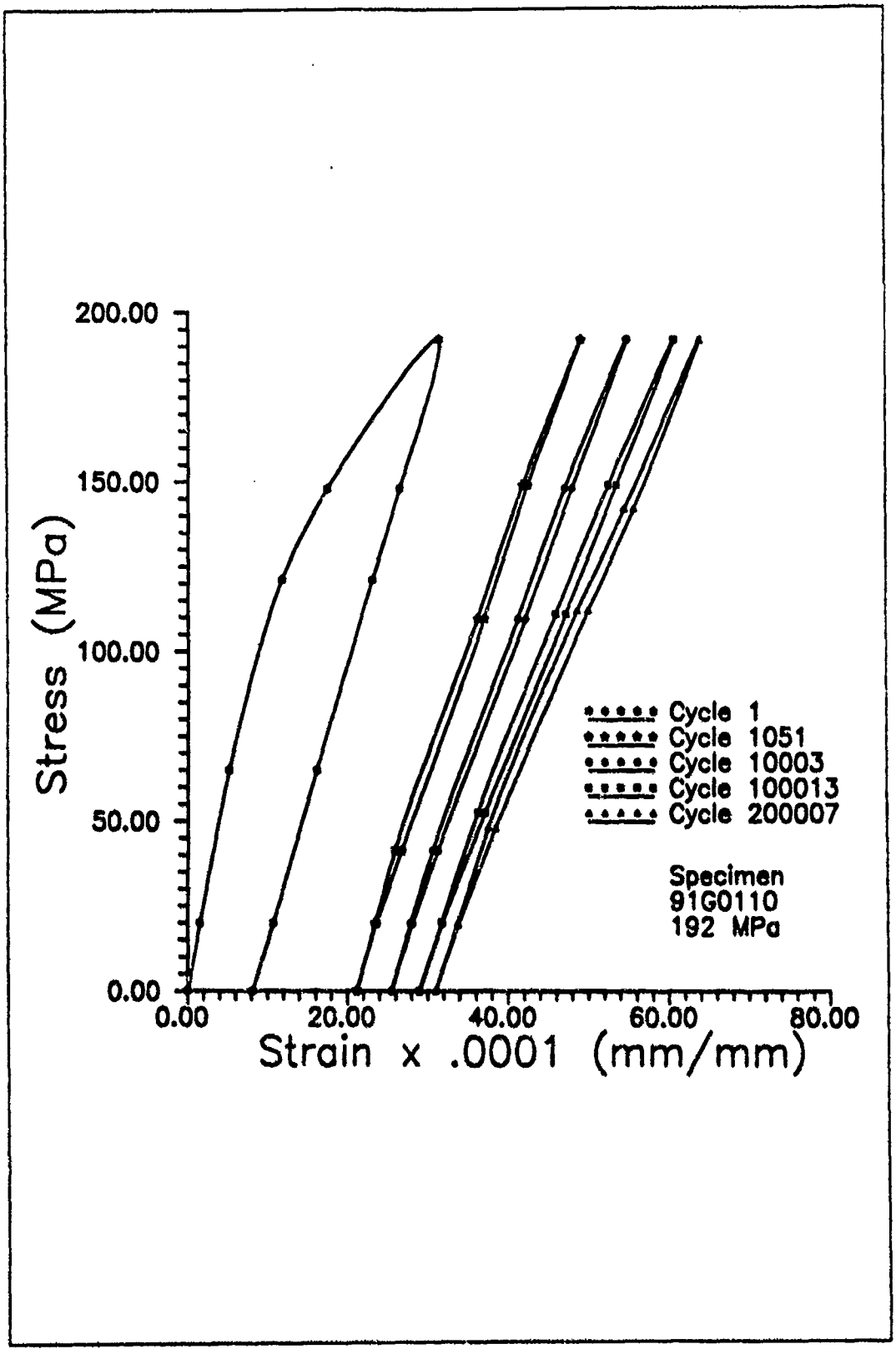

Figure 64 Stress Vs. Strain 192 MPa Test

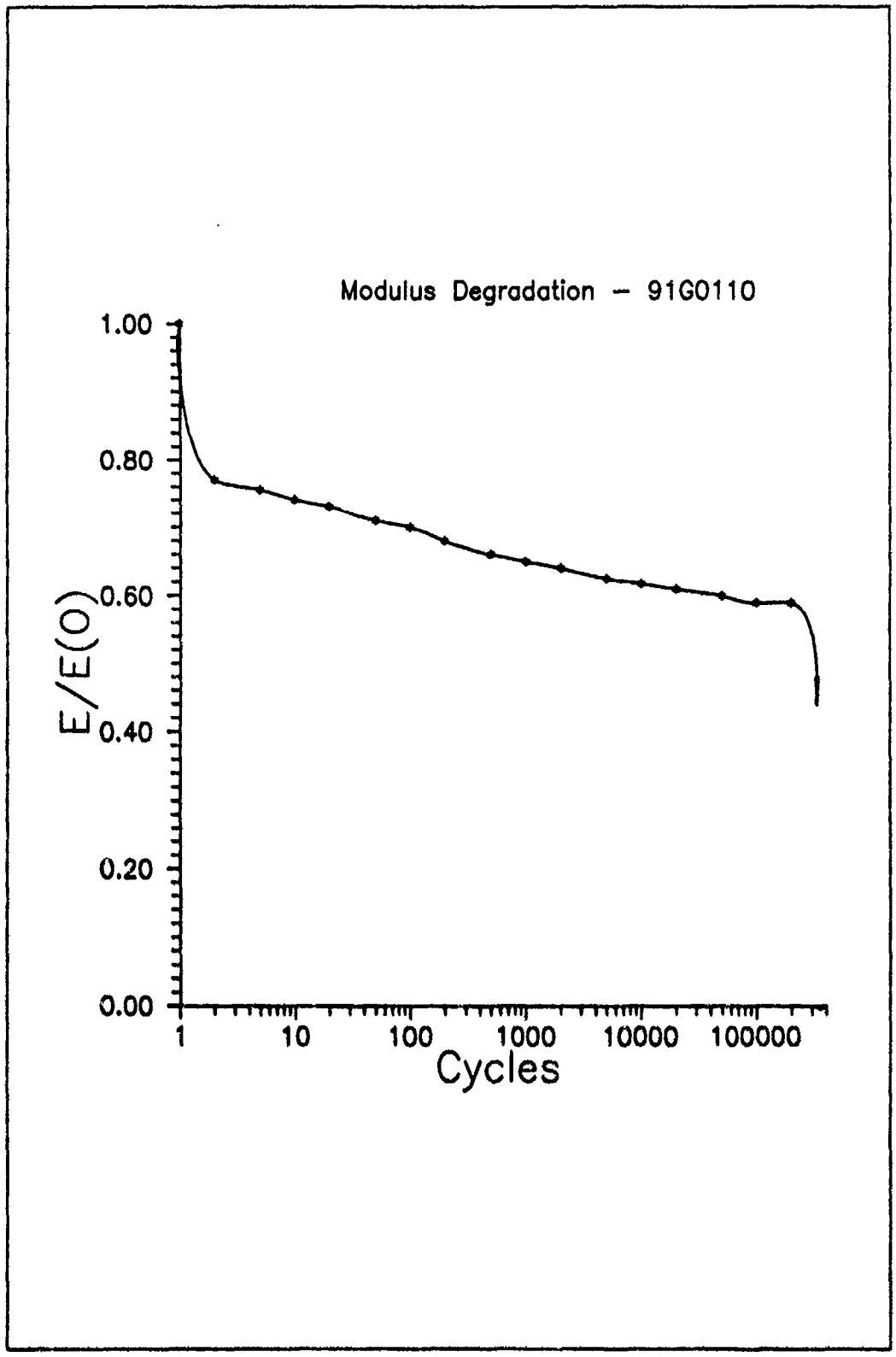

Figure 65 Modulus Reduction 192 MPa Test

The six percent difference between failure and run-out provided an endurance limit with a sufficiently small zone that further tests in this region were deemed unnecessary.

The final fatigue test, specimen 91G0108 was tested at 203 MPa maximum stress. This was equivalent to .91 ultimate stress. The stress-strain curves, modulus reduction and fracture surface are shown in figures 66, 67 and 68.

Residual strain, modulus decrease and crack closing stresses were consistent with previous tests where the specimen failed. Modulus reduction is significant in the first few cycles followed by steady decline until failure. This specimen failed after 52318 cycles.

Even though this specimen did not last as long as the 209 MPa test, it is within the scatter band normally seen in composite fatigue testing. Therefore, the test was considered a valid data point. The final S-N curve is presented in figure 69. The dashed horizontal line depicts the endurance limit for the bidirectional laminate.

Two static tensile tests were performed on unnotched $[(0/90)_2]_s$ SiC/1723 to determine if their failure strengths were vastly different from unnotched specimens as in the unidirectional case. The two specimens had failure stresses of 226 MPa and 254 MPa. These were very close to the 217 MPa and 223 MPa values obtained from notched tensile tests. It can be concluded that the notch does not have a significant effect on a bidirectional laminate.

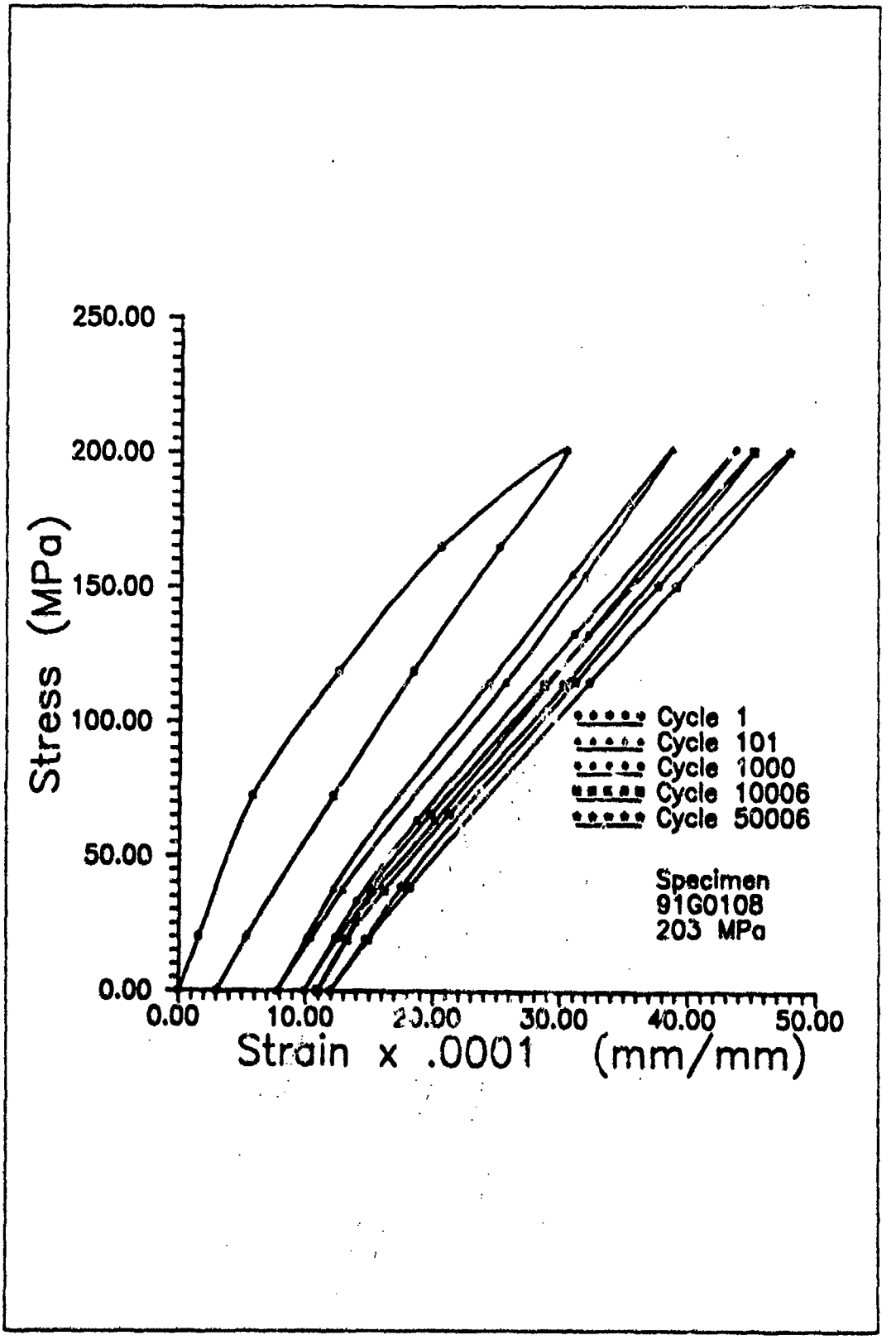

Figure 66 Stress Vs. Strain 203 MPa Test

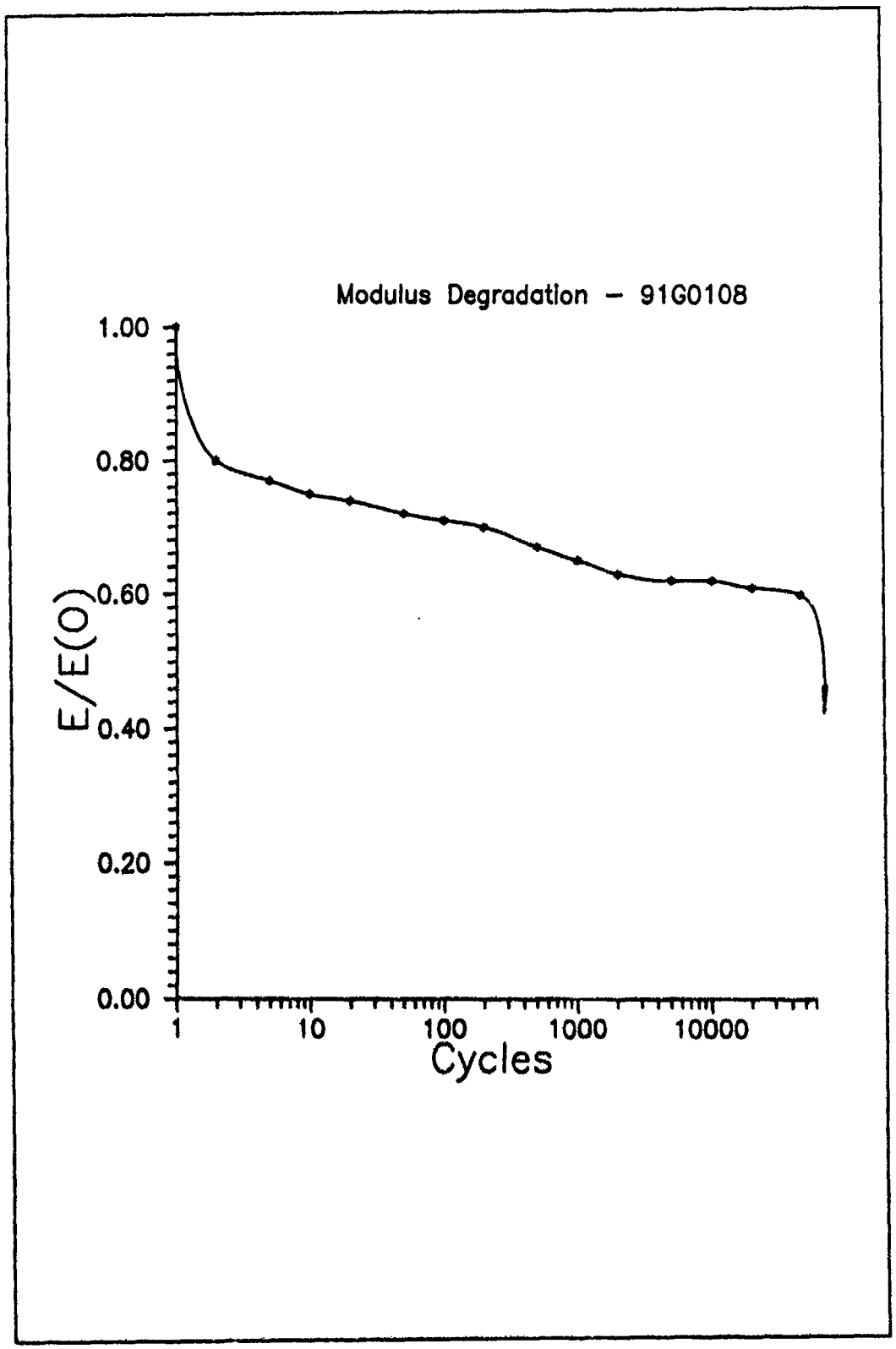

Figure 67 Modulus Reduction 203 MPa Test

Figure 68 Final Fracture, Specimen 91G0108

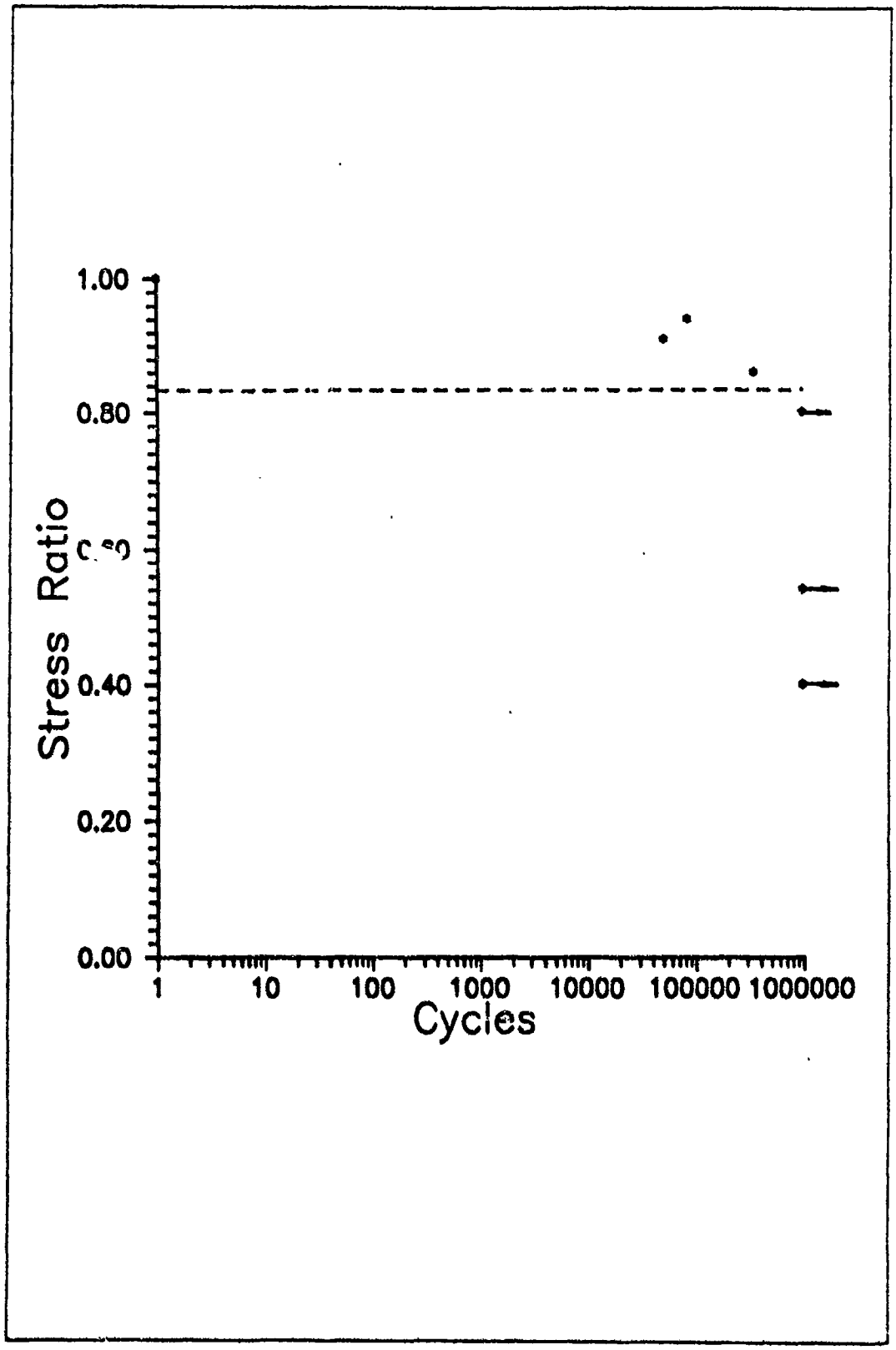

Figure 69 S-N Curve $[(0/90)_1]_s$ Laminates

Notch insensitivity can be explained by some of the replicas that were made. As has been shown, cracking did not extend from the 90^0 plies into the 0^0 plies. The 0^0 plies served as a retarder to damage that occurred in the transverse plies. Surface longitudinal cracks in the 0^0 plies were not evident in these tests as they had been in the unidirectional tests. However, it can be argued that cracking in the 0^0 plies, which had to occur even though it was not recorded, was also retarded when coming into contact with the transverse plies. Longitudinal ply damage can be assumed because testing was performed above the second proportional limit, indicative of 0^0 lamina damage.

A clear endurance limit region had been established for $[(0/90)_2]_s$ SiC/1723. This endurance limit falls within eight percent of the endurance limit calculated by Zawada and Butkus [44] for unnotched SiC/1723, further supporting the claim for notch insensitivity. The dependence on stress level for fatigue life is not as clearly defined as the unidirectional case. This is shown in the difference between the S-N curves.

2. Analytical Comparisons Classical laminated plate theory has been used previously to characterize fatigue behavior of a quasi-isotropic laminate [24]. Tracy found that by applying total ply discount methods to his data, the methods clearly showed where fatigue failure or run-out would occur.

This method was modified and adopted for the bidirectional tests in this thesis. Previous work had been done on unnotched specimens so there were no complications in determining the modulus due to the presence of the hole. However, with notched specimens, the stress and strain field near the hole can be quite complex. This would make modulus calculations near the hole very difficult. This difficulty was avoided by using a clip-on extensometer to measure displacements. The extensometer had a gage length of 25.4 mm and the specimen holes had diameters of only 1.7 mm. Therefore, the points on the specimen where the extensometer was attached were sufficiently far away from the hole to yield a constant far field stress field. This, in effect, eliminated the hole from entering into the measurement of the modulus, allowing discount methods to be applied.

Established values for E_1, E_2, ν_{12}, ν_{21} and G_{12} were obtained for SiC/1723 from Bachmann [43]. These values are given on the next page.

$$E_1 = 139.97 \text{ GPa}$$

$$E_2 = 87.98 \text{ GPa}$$

$$\nu_{12} = .18$$

$$\nu_{21} = .113$$

$$G_{12} = 43.99 \text{ MPa}$$

These values were inserted into equations 42, 43 and 44.

$$Q_{11} = \frac{E_1}{1 - (\nu_{12})(\nu_{21})} \tag{42}$$

$$Q_{12} = \frac{\nu_{12} E_2}{1 - (\nu_{12})(\nu_{21})} \tag{43}$$

$$Q_{22} = \frac{E_2}{1 - (\nu_{12})(\nu_{21})} \tag{44}$$

As discussed earlier in Chapter II, the stiffnesses for each lamina were transformed to the laminate coordinate system. The $[\overline{Q_{ij}}]$ matrix for each lamina is given below.

$$[\bar{Q}]_0 = \begin{vmatrix} 142.9 & 16.17 & 0 \\ 16.17 & 89.80 & 0 \\ 0 & 0 & .44 \end{vmatrix} \text{ GPa} \tag{45}$$

$$[\bar{Q}]_{90} = \begin{vmatrix} 89.8 & 16.17 & 0 \\ 16.17 & 142.88 & 0 \\ 0 & 0 & .44 \end{vmatrix} GPa \qquad (46)$$

The extensional stiffnesses, $[A_{ij}]$, were then calculated. Tracy considered A_{11} to be equivalent to the longitudinal stiffness that was measured by the extensometer. However, the derivation in Chapter II clearly indicates that A_{11} and A_{12} are also needed to determine E_x. The extensional stiffnesses were then substituted into equation (35) to yield a modulus value of 115.7 GPa. This value was somewhat lower, eleven percent, then the average exporimentally determined value.

Total ply failure was assumed in the transverse plies, thus, $[\overline{Q_{ij}}]$ values were set to zero for those laminae. The extensional stiffnesses were then recomputed leading to a longitudinal modulus of 70.99 GPa. This represented .61 of the original modulus value. This value is shown as the dashed horizontal line in figure 70, which depicts the modulus degradation for all bidirectional tests. The line marks the point between fatigue failure and run-out. Assuming total ply failure in the 90^0 plies is consistent with the damage modes that were observed. Transverse cracking extended in the 90^0 plies leading to fracture and delamination with the 0^0 lamina. The 0^0 laminae were then bearing the entire load leading to fiber fracture and

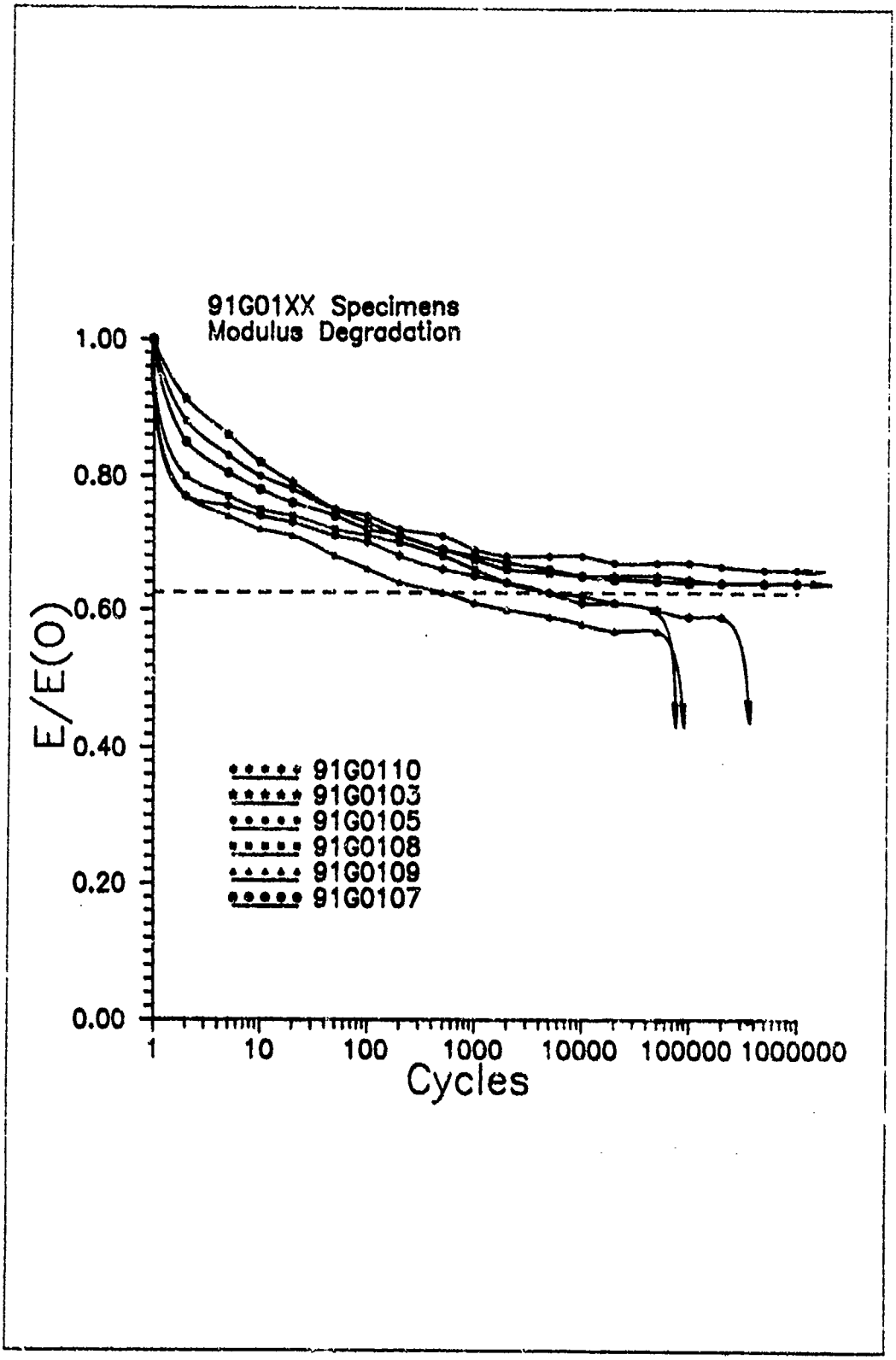

Figure 70 Modulus Degradation $[(0/90)_7]_s$ Specimens

pull-out shortly therafter.

Hence, applying elements of classical laminated plate theory along with total ply discount methods, the fatigue behavior of bidirectional SiC/1723 can be characterized and predicted with excellent accuracy.

V. CONCLUSIONS AND RECOMMENDATIONS

A. Conclusions

Tension-tension fatigue testing was performed on unidirectional, $[0]_8$, and bidirectional, $[(0/90)_2]_s$, notched laminates of SiC/1723. The specimens had a centrally located hole drilled in them to evaluate the effect of a stress concentration on fatigue life. The D/W ratio for all tests was .26 $\pm$ .02.

Static tensile tests on notched $[0]_8$ specimens showed a large drop in ultimate strength of the composite. Average notched strength of the specimens was 320 MPa. Unnotched strengths ranged from 550 MPa to 680 MPa. Large longitudinal matrix cracks extending in the loading direction led to final fracture. These cracks emanated near the points on the hole considered to be the theoretical maximum stress concentration points in the literature.

Fatigue testing showed the same damage modes as the static tests. With increased cycling, longitudinal matrix cracking extended from the holes. These cracks existed throughout the thickness, coalesced and grew lengthwise in the specimen. Fiber breakage and pullout occurred in these crack zones leading to specimen failure.

Specimen lifetime was determined to be a function of applied stress as shown in the S-N curve. A clear endurance limit window was also established as being between .77 and .82 of ultimate strength. Below .77 of ultimate strength,

the specimen survived one million cycles of fatigue testing. Above .82 of ultimate, the specimen failed before 54000 cycles.

Several existing fatigue models that had been used with metal matrix composites and graphite/epoxy were applied to this composite to see if they could predict or characterize the fatigue life or behavior. The Whitney-Nuismer Model, previously used with SiC/Al, predicted an endurance limit window of .65 to .80 ultimate stress. This window was close to the experimentally evaluated endurance limit. The window was somewhat larger due to the wide range in unnotched specimen strengths. The other two models, Fatigue Modulus Concept and Elastic Modulus Degradation Model, predicted the fatigue life of the composite poorly.

Testing continued with the bidirectional laminates. Static tensile tests of notched specimens provided ultimate stresses of 217 MPa and 223 MPa. Unnotched tests yielded ultimate stresses of 226 MPa and 254 MPa. The proximity of unnotched to notched values indicated the effect of the hole, in terms of a stress concentration were negligible. The notched specimens fractured across the widths, at the hole, which accounted for the smallest cross-sectional area.

Fatigue testing showed the following damage modes. Early in cycling, matrix cracking would develop in the transverse plies. These cracks would then extend across the plies until they were either stopped at the $0^0/90^0$ interface

or deflected longitudinally. The deflected cracks would combine with other cracks providing a large damage zone on the ply interfaces. Failure would occur when the transverse ply cracks would extend through the width causing 90^0 ply failure. This was followed by delamination caused by the deflected cracks and finally fiber breakage and pullout in the 0^0 fibers.

As with the unidirectional specimens, fatigue life proved to be a function of applied stress. An endurance limit range of .81 to .86 of ultimate strength was obtained experimentally. Below .81 of ultimate, specimens would run-out one million cycles. Above .86 of ultimate strength, failure would occur.

Total ply discount methods utilizing elements of classical laminated plate theory were used to predict fatigue life of the $[(0/90)_1]_s$ specimens. The stiffness ratio of the specimen with transverse plies discounted over the original stiffness was calculated to be .61. Experimental results indicated the limit between run-out and failure occurred when the modulus ratio was between .60 and .64.

Hence, as the stress is increased to yield 90^0 ply failure, the specimen will fail. Total ply discount corroborates the damage observations seen during testing. All specimens showed transverse ply matrix cracking. Specimens which did not fail over one million cycles, did not experience failure in those plies. Failure occurred when the

90^0 layers failed, followed by delamination and fiber breakage in the 0^0 laminae.

B. Recommendations

There are many areas that warrant further study with SiC/1723; three of which will be mentioned here. They include high temperature testing, D/W ratio variations and flexural testing.

A promising future for ceramic matrix composites is their application in turbojet or ramjet engines. In these engines, CMCs like SiC/1723 would experience severe thermomechanical fatigue. Therefore, fatigue testing should continue with high temperature environment included. Testing could proceed with a constant elevated temperature and mechanical fatigue or cycling of both temperature and load.

Second, the unidirectional specimens were notch sensitive. However, only one D/W ratio was used in this thesis. Therefore, various hole sizes should be used to determine SiC/1723 dependence on notch geometry. This is not recommended for the bidirectional laminates since they appeared notch insensitive.

Lastly, flexural fatigue testing should be examined since realistic application of the composite would include bending as well as pure tensile loading. A three or four point bend fixture could be constructed and modified for use on one of the tensile test machines.

Bibliography

1. Van Vlack, L.H. Elements of Materials Science and Engineering. Reading Massachusetts: Addison-Wesley Publishing Co., 1980, page 256.

2. Ibid. page 312.

3. Chawla, K.K. Composite Materials Science and Engineering. New York: Springer-Verlag Inc., 1987, page 77.

4. Mallick, P.K. Fiber-Reinforced Composites. New York: Marcel Dekker Inc., 1988, page 7.

5. Goetchius, G.M. "Fatigue of Composite Materials," Advanced Composites III: Expanding the Technology. Proceedings of the Third Conference on Advanced Composites. Detroit MI: American Society for Metals. page 289.

6. Jones, R.M. Mechanics of Composite Materials. New York: Hemisphere Publishishing Corp., 1975, page 288.

7. Goetchius, G.M. "Fatigue of Composite Materials," Advanced Composites III: Expanding the Technology. Proceedings of the Third Conference on Advanced Composites. Detroit MI: American Society for Metals. page 290.

8. Kulkarni, S.V. et al. "Fatigue of Notched Fiber Composite Laminates: Analytical and Experimental Evaluation," Composite Materials: Testing and Design, ASTM STP 617. American Society for Testing and Materials, Philadelphia, 1976, page 70.

9. Ibid. page 71.

10. Hahn, H.T. "Fatigue Behavior and Life Prediction of Composite Laminates," Composite Materials: Testing and Design, ASTM 674. American Society for Testing and Materials, Philadelphia, 1978, page 383.

11. Goetchius, G.M. "Fatigue of Composites Materials," Advanced Composites III: Expanding the Technology. Proceedings of the Third Conference on Advanced Composites. Detroit MI: American Society for Metals. page 292.

12. Hahn, H.T. "Fatigue Behavior and Life Prediction of Composite Laminates," Composite Materials: Testing and Design, ASTM 674. American Society for Testing and Materials, Philadelphia, 1978, page 410.

13. Ibid. pp. 411-412.

14. Wang, A.S.D. "Strength, Failure and Fatigue Analysis of Laminates," Engineered Materials Handbook, Vol. 1-Composites. American Society for Metals, Columbus, OH.,1987.

15. Jen, M.R. et al. "Fatigue Degradation in Centrally Notched Quasi-Isotropic Laminates," Journal of Composite Materials, Vol. 24, August 1990, pp. 823-837.

16. Hwang, W and K.S. Han. "Fatigue of Composites-Fatigue Modulus Concept and Life Prediction," Journal of Composite Materials, Vol. 20, March 1986, page 155.

17. Ibid. page 158.

18. Tsangarakis, N. et al. "Static and Fatigue Notch Strength Prediction in Alumina Fiber Reinforced Aluminum Plates with a Circular Hole," Journal of Composite Materials, Vol. 22, April 1988, pp. 386-393.

19. Tsangarakis, N. "The Notch-Fatigue Behavior of an Aluminum Composite Reinforced Unidirectionally with Silicon Carbide Fiber," Journal of Composite Materials, Vol. 21, November 1987, pp. 1008-1016.

20. Timoshenko, S.P. and J.N. Goodier. Theory of Elasticity Second Edition. New York: McGraw-Hill, 1951, page 78.

21. Tsangarakis, N. et al. "Static and Fatigue Notch Strength Prediction in Alumina Fiber Reinforced Aluminum Plates with a Circular Hole," Journal of Composite Materials, Vol. 22, April 1988, pp.386-393.

22. Butkus, L. et al. "Fatigue Testing of Ceramic Matrix Composites at Room and Elevated Temperature," pending publication by American Society for Testing and Materials, 1990.

23. Jones, R.M. Mechanics of Composite Materials. New York: Hemisphere Publishing Co.,1975, pp. 46-51, 147-166.

24. Tracy, Capt. G.D. Failure Mechanisms in a Quasi-Isotropic Ceramic Composite Laminate Under Tensile Fatigue Loading. MS Thesis, AFIT/GAE/ENY/90D-30. School of Engineering, Air Force Institute of Technology (AU), Wright-Patterson AFB OH, December 1990.

25. Langley, N.R. et al. "Properties of Ceramic Fibers from Organosilicon Polymers," Fiber Reinforced Ceramic Composites, edited by K.S. Mazdiyasni. Park Ridge, NJ: Noyes Publications, 1990, page 64.

26. Yajima, S. et al. "Synthesis of a Polytitanocarbosilane and its Conversion into Inorganic Compounds," Journal of Materials Science, Vol. 16, 1981, pp. 1349-1355.

27. Klang, E.C. and M.W. Hyer. "Damage Initiation at Curved Free Edges: Application to Uniaxially Loaded Plates Containing Holes and Notches," Recent Advances in Composites in the United States and Japan , ASTM STP 864. American Society for Testing and Materials. Philadelphia, 1985, pp. 79-83.

28. Kress, G.R. and W.W. Stinchcomb. "Fatigue Behavior of Notched Graphite/Epoxy Laminates," Recent Advances in Composites in the United States and Japan, ASTM STP 864. American Society for Testing and Materials. Philadelphia, 1985, pp. 173-195.

29. Andrews, A. ABC's of Ultrasonics. New York: Bobbs-Merrill Co. 1961, page 80.

30. Frederick, J.R. Ultrasonic Engineering. New York: John Wiley and Sons Inc. 1965, pp.249-256.

31. Ibid.

32. Camponeschi, E.T. and W.W. Stinchcomb. "Stiffness Reduction as an Indicator of Damage in Graphite/Epoxy Laminates," Composite Materials: Testing and Design, ASTM STP 787. American Society for Testing and Materials. Philadelphia, 1982, pp. 225-246.

33. Prewo, K.M. "Fatigue and Stress Rupture of Silicon Carbide Fiber-Reinforced Glass-Ceramics," Journal of Materials Science. Vol. 22, 1987, pp. 2695-2701.

34. Kim R.Y. and N.J. Pagano. "Initiation of Damage in Unidirectional Brittle Matrix Composites," Proceedings of the Fourth Japan-US Conference on Composite Materials. pp. 799-812. Lancaster PA: Technomic Publishing Co., 1988.

35. Bullock, Capt. D.E. Failure Characterization of a Fiber Reinforced Ceramic Matrix Composite with Circular Holes. MS Thesis, AFIT/GAE/ENY/91D. School of Engineering, Air Force Institute of Technology (AU), Wright-Patterson AFB OH, December 1991.

36. Marshall, D.B. and A.G. Evans. "Failure Mechanisms in Ceramic-Fiber/Ceramic Matrix Composites," Journal of the American Ceramic Society. Vol 68, No. 5, 1985, pp.225-231.

37. Mallick, P.K. Fiber-Reinforced Composites. New York: Marcel Dekker Inc., 1988, page 238.

38. Tsangarakis, N. "The Notch-Fatigue Behavior of an Aluminum Composite Reinforced Unidirectionally with Silicon Carbide Fiber," Journal of Composite Materials. Vol. 21, November 1987, pp. 1008-1016.

39. Caslini, M. et al. "Study of Matrix Cracking and Delamination in Glass/Epoxy Laminates," Journal of Composites Technology and Research. Vol. 9, No. 4, 1987, pp. 121-130.

40. Sbaizero O. and A.G. Evans. "Ceramic Matrix Composites," Journal of the American Ceramic Society. Vol. 69, No. 6, pp. 481-486.

41. Mallick, P.K. Fiber-Reinforced Composites. New York: Marcel Dekker Inc., 1988, pp. 240-241.

42. Chawla, K.K. Composite Materials Science and Engineering. New York: Springer-Verlag Inc., 1987, page 250.

43. Bachmann Capt. S.E. Transverse Cracking in a Fiber Reinforced Ceramic Matrix Composite. MS Thesis, AFIT/GAE/ENY/90D-2, School of Engineering, Air Force Institue of Technology (AU), Wright-Patterson AFB OH, December 1990.

44. Zawada L.P. and L.M. Butkus. "Room Temperature Tensile and Fatigue Properties of Silicon Carbide Fiber-Reinforced Aluminosilicate Glass," Proceedings, 14th Annual Conference on Composites and Advanced Ceramics. Cocoa Beach, FL. 1990.

Appendix I

Table 1 Unidirectional Fatigue Tests

Specimen	Width (mm)	Thickness (mm)	Initial Modulus (GPa)	Maximum Stress (MPa)	Number of Cycles to Failure
90G0304	5.690	2.667	125.0	130	Runout
90G0305	5.920	2.540	128.2	140	Runout
90G0307	5.812	2.464	126.1	170	Runout
90G0308	6.083	2.426	120.0	250	53803
90G0409	6.070	2.362	139.8	270	Runout
90G0701	5.994	2.362	145.2	313	10
90G0703	6.070	2.375	151.0	299	17001
90G0704	5.994	2.362	148.0	310	1105

Table 2 Unidirectional Tensile Tests

Specimen	Width (mm)	Thickness (mm)	Proportional Limit (MPa)	Maximum Stress (MPa)
90G0303	6.350	2.622	169.5	321
90G0301	5.718	2.622	143.0	282
90G0306	5.599	2.516	144.0	297
90G0701	5.994	2.363	Unavailable	348

Note- All Specimens had 1.6 mm hole

- Stresses based on minimum cross-sectional area

Appendix II

Table 3 Bidirectional Fatigue Tests

Specimen	Width (mm)	Thickness (mm)	Initial Modulus (GPa)	Maximum Stress (MPa)	Number of Cycles to Failure
91G0105	6.350	2.845	138.0	120.0	Runout
91G0103	6.020	2.769	125.0	88.0	Runout
91G0107	5.870	2.896	134.8	180.0	Runout
91G0108	6.070	2.896	122.0	203.0	52318
91G0109	5.840	2.896	142.0	209.0	87587
91G0110	6.121	2.845	124.0	191.8	357881

Table 4 Bidirectional Tensile Tests

Specimen	Width (mm)	Thickness (mm)	Proportional Limit (MPa)	Maximum Stress (MPa)
91G0106	6.121	2.819	61.0	223
91G0111	5.969	2.921	61.0	217
91G0112	4.699	2.591	Unavailable	226
91G0102	4.242	2.819	Unavailable	254

Note- All specimens had 1.6 mm hole except 91G0112 and 91G0102, which were notch-free

- Stresses based on minimum cross-sectional area

Vita

Captain William R. Moschelle was born 25 April 1964 in Watertown, New York. He graduated from Thousand Islands High School, Clayton, New York in 1982. He entered Clarkson University, Potsdam, New York, on an ROTC scholarship later that year. Upon graduation in 1986 with a Bachelor of Science Degree in Mechanical Engineering, he was commissioned in the Air Force. He was then assigned to the Air-to-Surface Guided Weapons System Program Office, Eglin AFB, Florida, where he was an aircraft integracion engineer. He was later reassigned to the Air-to-Surface Ballistic Weapons Office, Eglin AFB, where he was lead engineer on the Bigeye chemical bomb and 30 mm Ammunition Processor. He entered the School of Engineering, Air Force Institute of Technology in May 1990.

REPORT DOCUMENTATION PAGE

Form Approved
OMB No 0704-0188

1. AGENCY USE ONLY (Leave blank)	2. REPORT DATE	3. REPORT TYPE AND DATES COVERED
	December 1991	Master's Thesis (Final)

4. TITLE AND SUBTITLE Fatigue Behavior and Failure Mechanisms of Centrally Notched $[0]_8$ and $[(0/90)_2]_S$ Silicon Carbide Reinforced Alumino-Silicate Glass, SiC/1723

5. FUNDING NUMBERS

6. AUTHOR(S)

William R. Moschelle, Captain, USAF

7. PERFORMING ORGANIZATION NAME(S) AND ADDRESS(ES)

Air Force Institute of Technology
WPAFB, OH 45433

8. PERFORMING ORGANIZATION REPORT NUMBER

AFIT/GAE/ENY/91D-19

9. SPONSORING/MONITORING AGENCY NAME(S) AND ADDRESS(ES)

WL/MLLN
WPAFB, OH 45433

10. SPONSORING/MONITORING AGENCY REPORT NUMBER

11. SUPPLEMENTARY NOTES

12a. DISTRIBUTION/AVAILABILITY STATEMENT

Approved for public release;distribution unlimited

12b. DISTRIBUTION CODE

silicon carbides

13. ABSTRACT *(Maximum 200 words)*

Unidirectional and bidirectional notched laminates of SiC/1723 were fatigue tested under tensile-tensile loading with a load ratio of 0.1. The notch, a hole, was determined to have a significant effect on $[0]_{(8)}$ specimens. Matrix cracking developed near the theoretical maximum stress concentration points on the hole propagating parallel to the fibers, in the load direction, followed by fiber breakage. $[(0/90)_{(2)}]_{(S)}$ specimens were found to be notch insensitive. Damage modes for this lay-up were transverse ply matrix cracking, delamination and fiber breakage in the longitudinal plies which led to specimen failure. Several existing analytical models were then applied to these laminates to predict fatigue life.

14. SUBJECT TERMS	15. NUMBER OF PAGES
Ceramic Matrix Composites, Fatigue, Notched Specimen	151
	16. PRICE CODE

17. SECURITY CLASSIFICATION OF REPORT	18. SECURITY CLASSIFICATION OF THIS PAGE	19. SECURITY CLASSIFICATION OF ABSTRACT	20. LIMITATION OF ABSTRACT
Unclassified	Unclassified	Unclassified	UL